NTNU – Trondheim
Norwegian University of
Science and Technology

Perforation of Welded Aluminium Structures

Steffen Mikael Walnum
Breivik
Espen Frøyen Thomsen

Civil and Environmental Engineering
Submission date: June 2014
Supervisor: Tore Børvik, KT

Norwegian University of Science and Technology
Department of Structural Engineering

Department of Structural Engineering
Faculty of Engineering Science and Technology
NTNU - Norwegian University of Science and Technology

ACCESSIBILITY
OPEN

MASTER´S THESIS 2014

SUBJECT AREA:	DATE:	NUMBER OF PAGES: 142
Computational Mechanics	10.06.2014	18 + 110 + 14

TITTEL:

Perforation of Welded Aluminium Structures

UTFØRT AV:

Steffen Mikael Walnum Breivik
Espen Frøyen Thomsen

SUMMARY:
The ballistic properties of three welded plates have been investigated, with special emphasis on the weld and heat affected zone (HAZ). The material is aluminium alloy EN AW-6082 T6 and the plates are 10, 20 and 30 mm thick. Physical experiments have been compared with numerical simulations. Material input for the numerical simulations have either been taken from direct calibration and inverse modelling of tensile tests, or from NaMo results provided by Dr. Ole Runar Myhr at Hydro Aluminium. NaMo, a software developed by Dr. Myhr, uses material composition and temperature history as input, and gives material parameters for any point in the material as output. The material models from tensile tests have also been combined with hardness measurements in order to estimate material parameters for selected points across the HAZ.

Preliminary hardness measurements were taken to determine the weakest point of the HAZ, and these results were used to determine target positions for ballistic testing. A limited amount of ballistic experiments with 7.62 mm APM2 projectiles were performed. The exit velocity of the projectiles was higher in the HAZ for all three plates. In addition, the experiments targeting the weld itself revealed that this was somewhat stronger than the HAZ. Too few tests were performed in order to make a substantiated conclusion, however, trends were observed.

The numerical ballistic simulations have been performed using the finite element code IMPETUS Afea Solver. Simulations overall gave non-conservative results, meaning that they overestimate the resistance of the plates. An initial model was calibrated with tensile tests from the base material of the 10 mm plate, and therefore these results are closest to the values given by ballistic experiments. The complete numerical model gave the best results for the HAZ. Tensile tests combined with hardness measurements overestimated the strength of the HAZ, i.e. the results were non-conservative.

The Cylindrical Cavity Expansion Theory has been applied. With material parameters and geometry as input, it calculates the energy needed for perforation. Different material models have been tested, and generally the results are also with CCET, non-conservative. Thicker plates make the method less conservative.

Relatively accurate results were obtained using the two pure numerical methods described.

RESPONSIBLE TEACHER:	Professor Tore Børvik
SUPERVISORS	Professor Tore Børvik, Professor Odd Sture Hopperstad and PhD Student Jens Kristian Holmen
CARRIED OUT AT:	SIMLab, The Departement of Structural Engineering, NTNU

Institutt for konstruksjonsteknikk
Fakultet for ingeniørvitenskap og teknologi
NTNU - Norges teknisk- naturvitenskapelige universitet

TILGJENGELIGHET
ÅPEN

MASTEROPPGAVE 2014

FAGOMRÅDE:	DATO:	ANTALL SIDER: 142
Beregningsmekanikk	10.06.2014	18 + 110 + 14

TITTEL:

Perforering av sveiste aluminiumkonstruksjoner

UTFØRT AV:

Steffen Mikael Walnum Breivik
Espen Frøyen Thomsen

SAMMENDRAG:
De ballistiske egenskapene til tre sveiste plater har blitt undersøkt med fokus på selve sveisen og den varmepåvirkede sonen. Materialet brukt er aluminium EN AW-6082 T6 i platetykkelsene 10, 20 og 30 mm. Fysiske eksperimenter har blitt sammenlignet med numeriske simuleringer. Materialmodeller for de numeriske simuleringene har enten blitt tatt fra direkte kalibrering og inversmodellering av strekktester, eller fra NaMo-resultatene gitt av Dr. Ole Runar Myhr ved Hydro Aluminium. NaMo, en programvare utviklet av Dr. Myhr, bruker materialsammensetning og temperaturhistorie som inndata, og gir materialparametere som utdata. Materialmodeller fra strekktester har også blitt kombinert med hardhetsmålinger for å anslå materialparametre for utvalgte punkter på tvers av HAZ.

Foreløpige hardhetsmålinger ble foretatt for å bestemme det svakeste punktet i HAZ, og disse resultatene ble brukt for å bestemme treffpunkter for ballistisk testing. En begrenset mengde ballistiske eksperimenter med 7,62 mm APM2-prosjektiler ble utført. Utgangshastigheten for prosjektilene var høyere i HAZ for alle de tre platene. Videre eksperimenter rettet mot selve sveisen viste at denne ga større motstand enn HAZ. For få tester ble utført for å lage en underbygget konklusjon. Tendenser ble imidlertid observert.

De numeriske ballistiske simuleringene har blitt utført ved hjelp av elementmetodekoden IMPETUS Afea Solver. Simuleringene ga stort sett ikke-konservative resultater, noe som betyr at de overvurderer motstanden av platene. En initialmodell ble kalibrert med strekkprøver fra basematerialet av 10 mm-platen, og derfor er disse resultatene nærmest de verdiene som ble målt i de ballistiske eksperimentene. Den komplette numerisk modellen ga de beste resultatene for HAZ. Strekktester kombinert med hardhetsmålinger overestimerte styrken av HAZ, dvs. resultatene var ikke-konservative.

Cylindrical Cavity Expansion Theory (CCET) har også blitt anvendt. Med materialparametre og geometri som inndata, beregner den energien som trengs for perforasjon. Ulike materialmodeller har blitt implementert, og generelt er resultatene også med CCET, ikke-konservative. Økende platetykkelser gjør metoden mindre konservativ.

Relativt nøyaktige resultater ble oppnådd med rene numeriske metoder.

FAGLÆRER:	Professor Tore Børvik
VEILEDERE:	Professor Tore Børvik, Professor Odd Sture Hopperstad og stipendiat Jens Kristian Holmen
UTFØRT VED:	SIMLab, Institutt for konstruksjonsteknikk, NTNU

Department of Structural Engineering
FACULTY OF ENGINEERING SCIENCE AND TECHNOLOGY
NTNU – Norwegian University of Science and Technology

MASTER'S THESIS 2014

for

Steffen M.W. Breivik and Espen Frøyen Thomsen

Perforation of welded aluminium structures

1. INTRODUCTION

Research of protective structures most often deals with normal impact on flat, flawless surfaces where the effects of edges and connections are disregarded. However, in the making of live protective structures the presence of e.g. welds, nuts or bolts is inevitable; making knowledge about connections an essential part of any design process. In the design of protective structures against small-arms bullets, steel is still the dominating material. The main reasons for this are that steels have high absolute strength and hardness combined with high ductility, low price compared to most other armour materials and excellent load carrying capability and formability. Thin plates of ultra-high-strength steels are therefore frequently being used both in civil and military ballistic armours, where the choice of alloy is a function of application, ballistic performance, weight and price. However, recent studies have indicated that high-strength aluminium can give equally good or even better ballistic properties than high-strength steel when area-weight is considered. In this study, the basic idea is to investigate the presence of a weld on the ballistic properties of an aluminium alloy through experimental tests, numerical simulations and analytical calculations.

2. OBJECTIVES

The research project has three main objectives: (1) investigate experimentally the effects of welding on the ballistic properties in aluminium structures, (2) predict the behaviour from the experiments numerically by using NaMo, Weldsim and nonlinear finite element methods, (3) employ the analytical approach in the cavity expansion theory to analyse the perforation process.

3. A SHORT DESCRIPTION OF THE RESEARCH PROJECT

The main topics in the research project will be as follows;

1. Extruded plates with different thicknesses (10, 20 and 30 mm) made of aluminium alloy EN AW-6082 T6, are produced by Hydro Aluminium Profiles (HAP) at Raufoss.
2. Such plates are welded together using MIG-welding by Marine Aluminium to make test specimens (approx. 100x400 mm^2).
3. Series of ballistic tests are performed on the plates to determine the effect of the weld as a function of distance from the weld.
4. Various material tests are carried out, and the data is used to identify material properties in a constitutive relation and fracture criterion.
5. A literature survey is done to understand the mechanisms in the heat treatment of aluminium alloys.
6. Numerical simulations of the impact tests using IMPETUS Afea Solver are carried out. NaMo can be used to obtain material parameters without doing any experiments, while Weldsim may be applied to determine the HAZ. Numerical results are compared with experimental findings.
7. Utilisation of the closed form solutions available through the Cylindrical Cavity Expansion Theory (CCET) is encouraged.

Supervisors: Professor Tore Børvik, Professor Odd Sture Hopperstad and Jens Kristian Holmen

The thesis must be written according to current requirements and submitted to Department of Structural Engineering, NTNU, no later than June 10th, 2014.

NTNU, January 14th, 2014

Tore Børvik
Main supervisor/Professor

Preface

This thesis was written in the spring of 2014 and submitted in partial requirement for the degree of Master of Science in Civil and Environmental engineering, with Specialisation in Computational Mechanics. The experimental work was funded and the problem statement was formulated by the Structural Impact Laboratory (SIMLab) at the Department of Structural Engineering at the Norwegian University of Science and Technology (NTNU).

Trondheim, June 10 2014

Steffen M. W. Breivik

Espen Frøyen Thomsen

Acknowledgments

During the work of this thesis Professor Tore Børvik and PhD Student Jens Kristian Holmen have been of tremendous help. Weekly meetings, answering questions at any time and giving valuable input on any topic, have made this period more constructive and efficient for the authors.

Professor Odd Sture Hopperstad helped with a solution for estimating material models in the HAZ. His broad understanding of the field of material mechanics is much appreciated.

Fellow master's student Kjetil Steen Rostad provided us with necessary hardness measurements before ballistic testing. Dr. Ida Westerman followed up with complete hardness measurements and crystal clear macro photos of the weld and HAZ.

Ballistic testing was performed during one day, and this would not have been possible without the help of Trond Auestad. Ballistic test results, still frames and video footage from a high speed camera were provided by Mr. Auestad after testing.

Tensile tests were performed by Tore André Kristensen at SINTEF Materials and Chemistry. In addition he gave a thorough introduction into how the tensile tests were performed and the equipment being used.

Numerical material models have been made by Dr. Ole Runar Myhr at Hydro Aluminium in cooperation with IFE, Institute of Energy Technology, using the softwares NaMo and Weldsim. Dr. Ole Runar Myhr has answered many questions regarding NaMo and the aluminium plates investigated.

Thanks to Professor Tore Børvik, Jens Kristian Holmen, Ingunn Frøyen, Asbjørn Breivik and Siri Olimb Myhre for proofreading, both technical and grammatical, before delivery and printing of this thesis.

Lastly, Dr. Lars Olovsson deserves recognition for the excellent finite element software IMPETUS Afea Solver. After trying similar softwares during the time at NTNU, IMPETUS Afea Solver has proven easy to work with in comparison. Its powerful 64 node cubic hexahedron element is truly excellent at displaying large plastic deformations, which is highly relevant for this thesis.

Abstract

The ballistic properties of three welded plates have been investigated, with special emphasis on the weld and heat affected zone (HAZ). The material is aluminium alloy EN AW-6082 T6 and the plates are 10, 20 and 30 mm thick. Physical experiments have been compared with numerical simulations. Material input for the numerical simulations have either been taken from direct calibration and inverse modelling of tensile tests, or from NaMo results provided by Dr. Ole Runar Myhr at Hydro Aluminium. NaMo, a software developed by Dr. Myhr, uses material composition and temperature history as input, and gives material parameters for any point in the material as output. The material models from tensile tests have also been combined with hardness measurements in order to estimate material parameters for selected points across the HAZ.

Preliminary hardness measurements were taken to determine the weakest point of the HAZ, and these results were used to determine target positions for ballistic testing. A limited amount of ballistic experiments with 7.62 mm APM2 projectiles were performed. The exit velocity of the projectiles was higher in the HAZ for all three plates. In addition, the experiments targeting the weld itself revealed that this was somewhat stronger than the HAZ. Too few tests were performed in order to make a substantiated conclusion, however, trends were observed.

The numerical ballistic simulations have been performed using the finite element code IMPETUS Afea Solver. Simulations overall gave non-conservative results, meaning that they overestimate the resistance of the plates. An initial model was calibrated with tensile tests from the base material of the 10 mm plate, and therefore these results are closest to the values given by ballistic experiments. The complete numerical model gave the best results for the HAZ. Tensile tests combined with hardness measurements overestimated the strength of the HAZ, i.e. the results were non-conservative.

The Cylindrical Cavity Expansion Theory, CCET, has been applied. With material parameters and geometry as input, it calculates the energy needed for perforation. Different material models have been tested, and generally the results are also with CCET, non-conservative. Thicker plates make the method less conservative.

Relatively accurate results were obtained using the two pure numerical methods described.

Contents

Nomenclature

α	Aluminium alloy phase
α_T	Heat expansion coefficient
β	Aluminium alloy phase
χ	Taylor-Quinney coefficient
ε_A	Almanasi strain
ε_e	Engineering strain
ε_G	Green strain
ε_l	True strain
ε_{lu}^p	True plastic strain at necking
ε_l^p	True plastic strain
ε^p	Equivalent plastic strain
ε_f^p	Equivalent plastic strain at fracture
$\dot{\varepsilon}^p$	Plastic strain rate
ε_v	Volumetric strain
γ	Cavity surface
λ	Heat conductivity
λ_g	Geometric slip distance
μ	Friction
ν	Poisson's ratio
ψ	Caliber radius head
ρ	Density
ρ_g	Geometrically necessary dislocations
ρ_p	Density of projectile
ρ_s	Statistically stored dislocations
ρ_t	Density of target
ρ_t	Total dislocation density
σ_0	Yield strength
σ_1	Maximum principal stress
$\Delta\sigma_d$	Contribution from dislocation hardening
σ_e	Engineering stress
σ_{eq}	Equivalent stress
σ_f	Flow stress
σ_i	Yield strength pure aluminium
σ_p	Precipitation hardening of alloy
σ_s	Quasi-static stress required to open a cavity
σ_{sat}	Saturation stress
σ_{ss}	Solid solution hardening potential
σ_t	True stress
σ_u	True tensile strength
a_B	Specimen radius at neck
A_0	Reference area
A	Area
B_0	CCET parameter
b	Burgers vector
b_{haz}	Width of HAZ
C_0	Reference concentration
C	CCET parameter

C	Strain rate parameter
C_i	Voce hardening parameters
$\overline{C_i}$	Mean concentration of element i
C_p	Heat capacity
d_0	Reference diameter
D	Damage parameter
d	Diameter
E	Young's modulus
EOS	Equation of state
$\overline{F}$	Mean interaction force
f_0	Volume fraction of Orowan particles
F	Force
fcc	Face-centered cubic
G	Shear modulus
h	Target plate thickness
HAZ	Heat affected zone
HV	Vickers hardness
k_1	Function of ogive shaped nose
K	Bulk modulus
l	Friedel length
L	Current length
ΔL	Incremental length
M	Taylor factor
m_p	Mass of projectile
m_{pl}	Mass of plug
MSE	Mean square error
p	Pressure
Q_i	Voce hardening parameters
R	Work hardening variable
R_B	Neck radius
s^{-1}	Strain rate unit
s	Second
T	Temperature
T_0	Reference temperature
T_{cr}	Recrystallisation temperature
T_m	Melting temperature
T_r	Room temperature
T^*	Homologous temperature
v_{bl}	Ballistic limit velocity
v_i	Initial velocity
v_r	Residual velocity
W_c	Plastic work per unit volume at fracture

CHAPTER 1

Introduction

The science of impact by high speed free-flying projectiles is known as ballistics. It is of great interest for both military and civil protective purposes. Because of its high strength, ductility, hardness, good formability and low cost, high strength steels have generally been preferred in the design of protective structures against small-arms bullets. Recent studies, however, suggest high-strength aluminium alloys may give equally good or even better ballistic properties, when areal weight is taken into consideration [1]. There has, however, been little research into the ballistic properties of welded connection.

The literature [2], describes the process of age hardening aluminium alloys. By natural and artificial ageing of certain alloy types, the strength can be increased. There is, however, an ideal length of time before the material starts to lose its strength, i.e. the material is over aged. At which point the ageing process should be stopped. When already age hardened alloys are subjected to welding, the temperature in the area close to the weld will get affected, and a heat affected zone (HAZ) is created.

The aluminium alloy used in this thesis is EN-AW 6082 T6. The 6XXX series is generally weldable, but the T6 temper suffer from severe HAZ softening because of the reversion of the hardening precipitates [3]. This thesis will therefore study the ballistic properties of the weld and the HAZ compared to the base material.

Figure 1.1 describes, by the means of a flow chart, the process of which the work will be carried out. A theoretical study will constitute a basis for the work. Ballistic experiments will be performed, where APM2 bullets will be fired at three different welded plates. These plates will be of 10 mm, 20 mm and 30 mm thicknesses. Material testing will be performed to investigate the material properties and to find the parameters of the material model. This material model will be used as input for numerical simulations in order to recreate the experiments using the finite element code IMPETUS Afea Solver. In addition, a numerical material model will be attempted, using NaMo, Nano Structure Model, and WELDSIM. The Cylindrical Cavity Expansion Theory, a closed form analytical expression, will also be used in order to find ballistic limit velocities.

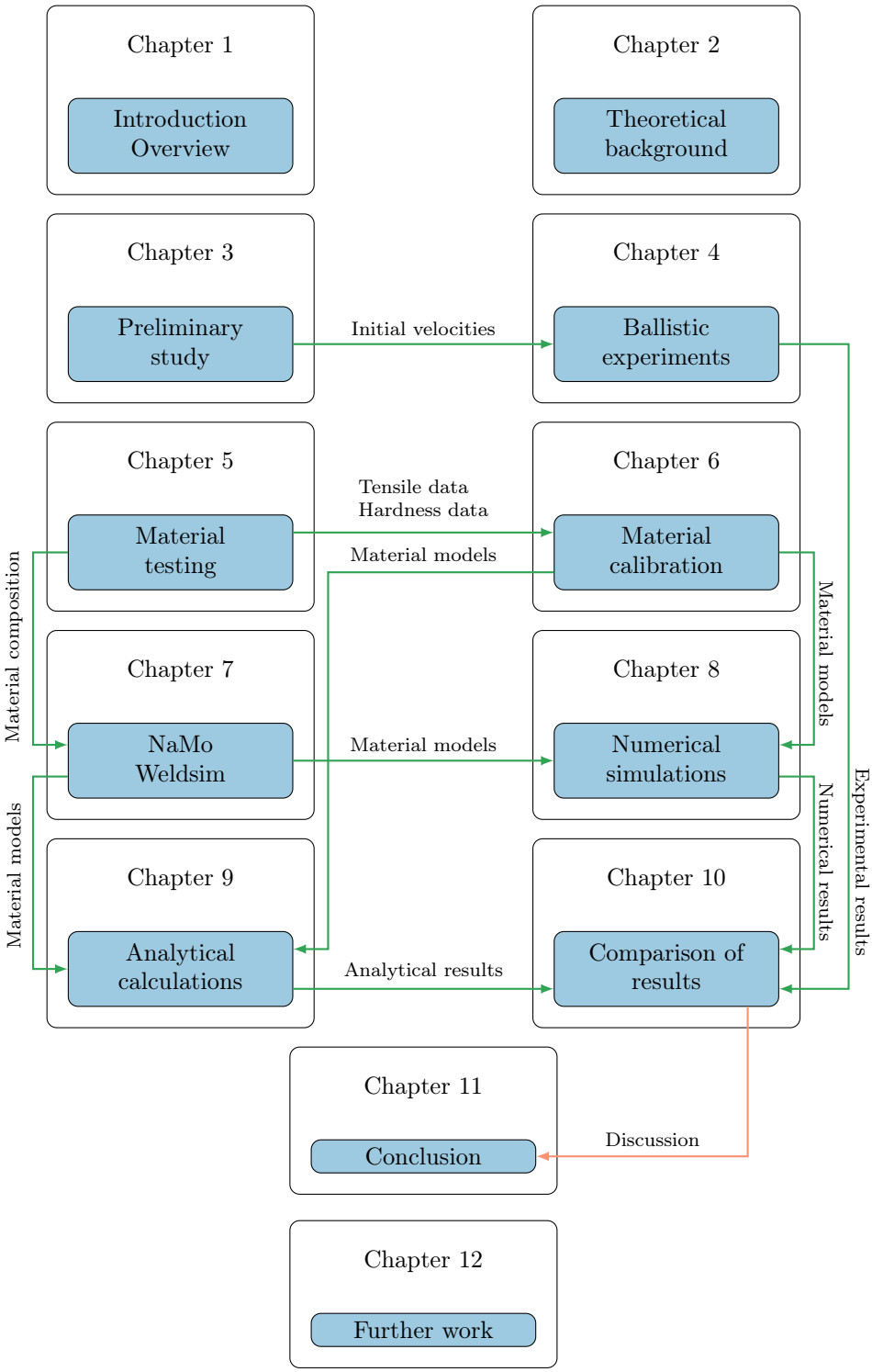

Figure 1.1: Thesis overview

CHAPTER 2

Theoretical Background

2.1 Ballistic Terminology

This chapter introduces some of the most important words and concepts used in this thesis.

Børvik [4] defines impact as the collision between two or more solids, where the interaction may be elastic, plastic, fluid or any combinations of these. The science of free-flying projectiles launched by an engine, typically firearms, their trajectory and impact, is called ballistics. Most relevant for this thesis is the subsection called terminal ballistics, which deals with impact between a projectile and a target.

Because the projectile velocity is of great importance in ballistics, different velocity regimes have been classified based on the target response. These regimes range from the low velocity regime, which deals with impacts below 50 m/s to the hyper velocity regime, which deals with impacts above 3000 m/s. This thesis, however, will only be involved in the sub-ordnance and ordnance regimes, ranging from 50-500 m/s and 500-1300 m/s respectively. In these regimes, the impact is characterised by highly localised plastic deformation. The activated zone of the target will generally be no more than two or three projectile diameters wide, giving hardly any global deformation. The generated heat has little or no time to dissipate, making the process adiabatic [4].

Depending on the material properties, velocity, shape of the projectile and relative dimensions of projectile and target plate, several modes of failure have been defined [5]. These failure modes are illustrated in Figure 2.1. As the projectile used in this thesis has an ogival shaped nose, and aluminium is a ductile material, the predominant failure mode is ductile hole growth. This assumption will be used in both analytical calculations and numerical simulations in subsequent chapters.

The tip of the ogival shaped nose makes a tiny hole in the target, and as Figure 2.1 illustrates, the projectile pushes the material laterally aside in localized plastic deformation. This continues until the hole is the same size as the projectile. Because the failure mode is quite predictable, with little or no unforeseeable fragmentation or fracture, material models can be used combined with the known size of the hole and an assumed rigid projectile, to analytically predict the energy needed for perforation. The numerical simulations are more likely to show this behaviour when a pinhole is introduced. A pinhole is simply a

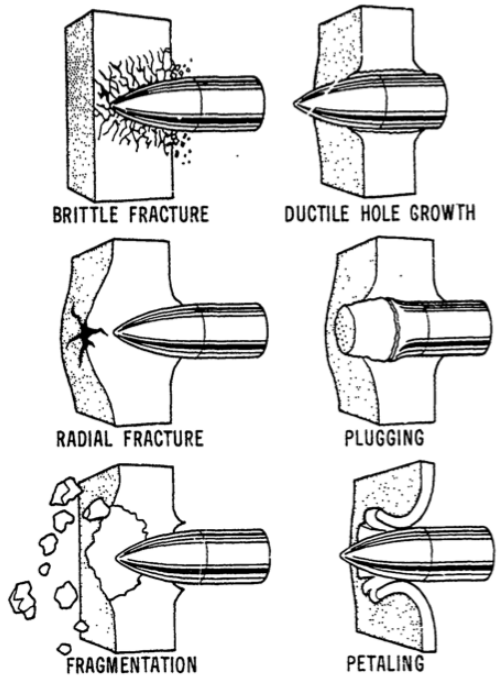

Figure 2.1: Different failure modes in impact dynamics [5]

thin hole through the target along the projectile impact axis. Studies show that a pin hole have little or no effect on the numerical results [6, 7]. A pin hole also eliminates the need for a fracture criterion. This is discussed further in Section 8.2.5.

2.1.1 Ballistic Limit Velocity

Figure 2.2 shows three different definitions of perforation. Backman and Goldsmith [8] define *perforation* as a projectile passing through a target having a residual velocity, v_r greater than zero. *Penetration* is defined as an impact where the target is penetrated, but v_r is zero.

The residual velocity is an important parameter in ballistics. It is the velocity at which, the projectile leaves the target after perforation. It depends on initial velocity, v_i and the ballistic limit velocity, v_{bl}.

The ballistic limit velocity is defined as the average v_i of two projectiles, where one only just perforates the target, and the other barely does not [4]. However in this thesis the ballistic limit velocity will be found from curve fitting using Recht-Ipson (see Section 2.5). Figure 2.3 illustrates the ballistic limit velocity, the ballistic limit curve and the ballistic limit line. The ballistic limit curve predicts the residual velocity as a function of the initial velocity. The ballistic limit line is defined as the residual velocity of a projectile passing through a target of zero thickness.

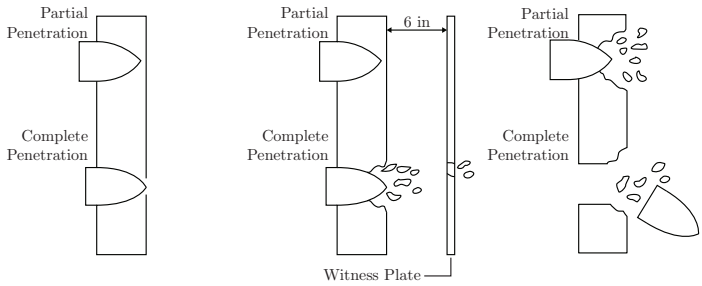

Figure 2.2: Definitions of perforation and partial penetration [8]

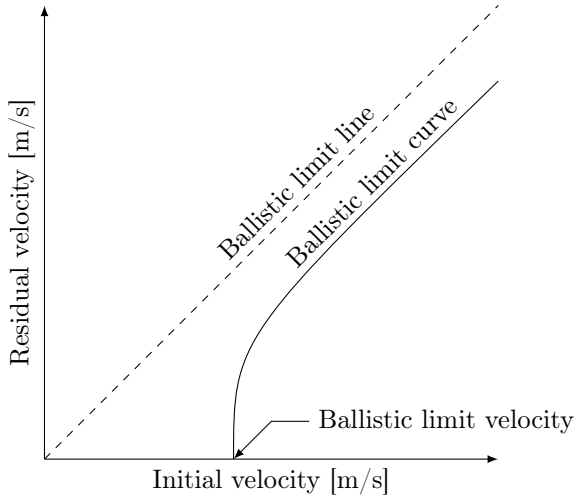

.

Figure 2.3: Illustration of the ballistic limit velocity and residual velocity as a function of the initial velocity [4]

2.2 Nonlinear Behaviour of Metals

When metals are subjected to extreme loads and strain rates, the material may exhibit nonlinear response. Since the projectiles in this thesis are in the sub-ordnance and ordnance regimes, this is highly relevant. Even though this subject is quite extensive, some of the most important concepts will be introduced in the following sections.

Cook et al. [2] mention three types of nonlinear behaviour important in structural engineering.

- *Material nonlinearity* occurs when the material is subjected to stresses and strains that surpass the yield limit. The material then experiences nonlinear hardening.
- *Contact nonlinearity* occurs when gaps between parts open or close, when the contact area and contact force change, or when there is sliding contact with frictional forces.

- *Geometric nonlinearity* occurs when deformation is sufficiently large, such that equilibrium equations must be written with respect to the deformed structural geometry.

2.2.1 Stress and Strain

Constitutive equations (Section 2.7), are dependent on good stress and strain measures. In traditional linear mechanics with small deformations, it is usually sufficient with engineering stress, σ_e, and engineering strain, ε_e. These are defined in Equations 2.1 and 2.2 respectively [9].

$$\sigma_e = \frac{F}{A_0} \tag{2.1}$$

$$\varepsilon_e = \frac{\Delta L}{L_0} \tag{2.2}$$

where F is the axial force, A_0 is the reference area, ΔL is the incremental length and L_0 is reference length. However, when dealing with large strains, the deformed geometry has to be taken into account. Thus other strain measures are needed. A finite strain measure is used to represent local deformations in a large deformation nonlinear analysis. Some finite strain measures are Green strain, ε_G, Almansi strain, ε_A, and logarithmic strain (true strain), ε_l, defined in Equations 2.3, 2.4 and 2.5 respectively [10]:

$$\varepsilon_G = \frac{L^2 - L_0^2}{2L_0^2} \tag{2.3}$$

$$\varepsilon_A = \frac{L^2 - L_0^2}{2L^2} \tag{2.4}$$

$$\varepsilon_l = \ln\left(\frac{L}{L_0}\right) \tag{2.5}$$

where L is the current length.

Important features of finite strain measures, are that they can predict zero strain for arbitrary rigid body translations and rotations, and reduce to infinitesimal strains if the nonlinear strain terms are neglected. They should also approach $-\infty$ for full compression and ∞ for infinite stretching. Figure 2.4 shows that only the logarithmic strain is suitable in the entire range [10].

Logarithmic strain will be used to calculate strain in upcoming tensile tests. Since the elastic strains in metals are small, and the plastic deformation does not alter the volume [9], the following equations can be used:

$$A_0 L_0 = AL \tag{2.6}$$

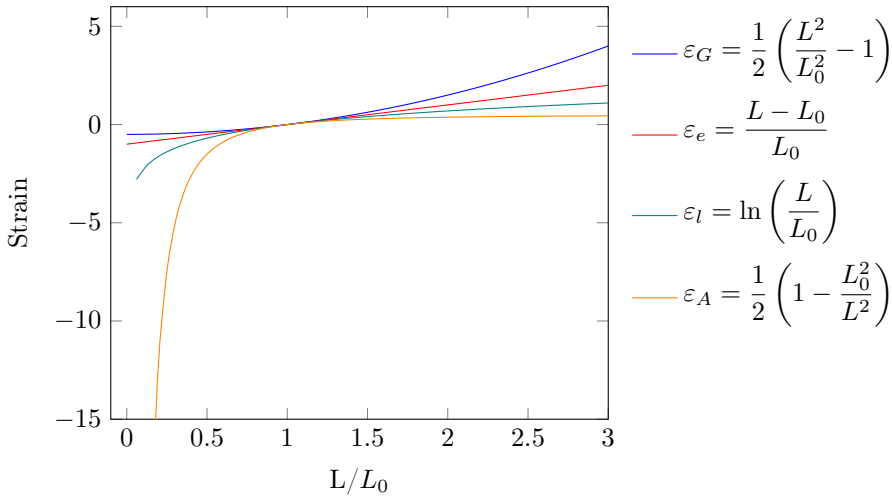

Figure 2.4: Four different strain measures

$$A_0 = \frac{\pi}{4} d_0^2 \tag{2.7}$$

$$A = \frac{\pi}{4} d^2 \tag{2.8}$$

where A_0 and d_0 are the undeformed cross sectional area and diameter of the specimen, while A and d are the dimensions after deformation. Inserting Equation 2.6, 2.7 and 2.8 into the expression for logarithmic strain, gives:

$$\varepsilon_l = 2 \ln\left(\frac{d_0}{d}\right) \tag{2.9}$$

With force and diameter, the true stress,σ_t, can be calculated:

$$\sigma_t = \frac{F}{A} = \frac{4F}{\pi d^2} \tag{2.10}$$

2.3 Aluminium

2.3.1 Background

Aluminium

Chemical symbol:	Al
Atomic number:	13
Atomic weight:	26.982
Density:	2700 kg/m^3
Electron order:	2 - 8 - 3

(a) Aluminium facts

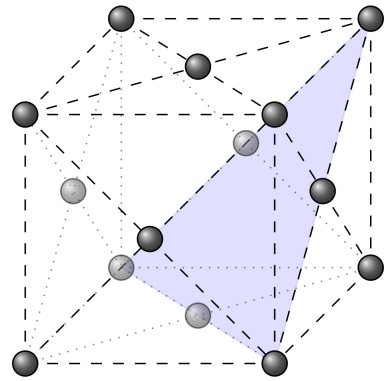

(b) Face-centered cubic lattice structure

Figure 2.5: Aluminium facts and crystalline structure

Aluminium is the third most abundant element in the earth's crust, and is usually extracted from the bauxite ore. Aluminium has many useful properties including good formability, high strength to weight ratio, excellent conductivity (both heat and electrical), easily recyclable, good corrosive resistance and good reflective capabilities. In addition, the density, ρ, of aluminium is about one third the density of steel. Many of these properties can be enhanced or reduced by adding other elements, making an aluminium alloy. Of all the aluminium produced, about 75% is still in use today [11], and only 5% of the energy used to make «new» aluminium is needed to recycle aluminium [11].

2.3.2 Microstructure

The microstructure of metals is described by the size, shape and distribution of their grains. A grain is a part of the metal where the atoms are organized in a crystalline way. Aluminium has a face-centered cubic, fcc, crystalline structure. Figure 2.5b shows the lattice.

As melted aluminium solidifies, small crystals or nuclei form at random positions. These continue to grow into larger grains, each with their own crystalline direction. Grain boundaries evolve when grains grow towards each other and the different crystalline directions meet. The strength of a material is highly dependent on how dislocations move inside the grains and across grain boundaries. With a finer grain structure, dislocations will have a harder time propagating since there are more grain boundaries to cross. In aluminium the preferred dislocation directions lie along {111} planes, one of which can be seen in Figure 2.5b as a shaded triangle. Figure 2.6 show how the grain size alters the mechanical properties in most metals.

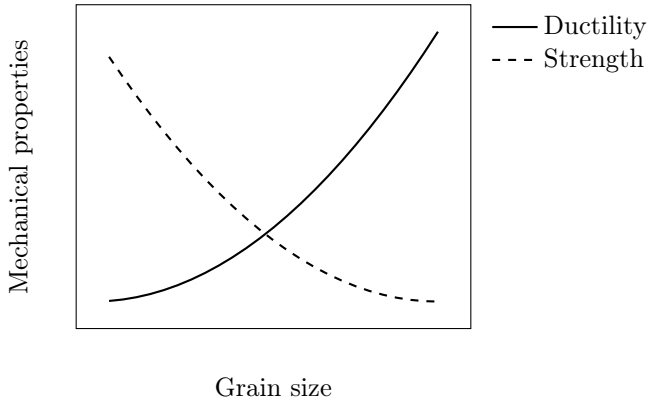

Figure 2.6: Grain size effects

2.3.3 Strengthening Mechanisms

Pure aluminium has low mechanical strength. To strengthen the material dislocation movement needs to be restricted [12]. The most common methods for achieving this are investigated in the following sections.

Strengthening by Grain Size Reduction

When melted aluminium cools, crystallisation starts at random places in the melt forming grains, as explained above. However, each grain and its inherent crystalline structure is randomly orientated. Now the structure and its slip planes change direction at the grain boundaries. This is illustrated in Figure 2.7. As we see from the figure, the dislocation has to change direction to continue into the next grain, requiring additional energy [12].

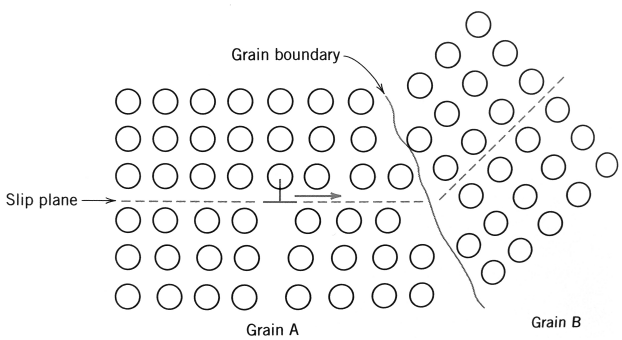

Figure 2.7: Grain orientation, grain boundary and slip plane [12]

With grain boundaries being an effective obstacle against dislocation motion, it is beneficial to have smaller and more numerous grains. This will give a greater total area of grain boundary, and with that, greater yield strength. The Hall-Petch equation suggests a closed form expression for the yield strength based on the average grain size [12]:

$$\sigma_y = \sigma_0 + \frac{k_y}{\sqrt{d}} \tag{2.11}$$

where d is the average grain size, σ_0 is a material constant for the starting stress of dislocation movement and k_y is a strengthening coefficient unique to each material.

Solid solution strengthening

Alloy elements are either substitutional or interstitial [12], which means that the introduced element either takes an aluminium atom's place in the lattice, or it fits in between the aluminium atoms. Usually this will skew the aluminium crystal. The alloying makes it more difficult for dislocations to move, and the material strengthens.

There are mainly two different alloy categories; wrought aluminium alloys and cast aluminium alloys. Most aluminium alloys starts out as cast ingots. Cast ingots are easily transformed into other products. The wrought aluminium alloys have been worked mechanically while the cast alloys have settled in a mould. The different wrought aluminium alloy series are based on one or more main alloying elements (see Section 2.3.4).

Heat treatment

Some of the alloy series are post production heat treatable. This can change the size, distribution and shape of the grains after alloy production. Table 2.1 and Table 2.2 show different heat treatments, often denoted «tempers».

Table 2.1: How different heat treatments are categorized [13]

Temper	Method	Description
F	As fabricated	No other heat treatment than the heat during production
O	Annealed	Heated a great deal to produce lower strength. Stable alloy.
H	Strain hardened	The H is usually followed by two digits. The first indicates additional temper methods used and the second the degree of strain hardening.
W	Solution heat-treated	Unstable temper seldom used
T	Thermally treated	Different heat treatments after fabrication to make stable tempers. Classified by digits 1-10.

Table 2.2: Different T-tempers [13]

Temper	Treatment sequence
T1	Cooled from hot working, naturally aged (at room temperature)
T2	Cooled from hot working, cold worked, naturally aged
T3	Solution heat-treated, cold worked, naturally aged
T4	Solution heat-treated, naturally aged
T5	Cooled from hot working, artificially aged (at elevated temperature)
T6	Solution heat-treated, artificially aged
T7	Solution heat-treated, stabilized
T8	Solution heat-treated, cold worked, artificially aged
T9	Solution heat-treated, artificially aged, cold worked
T10	Cooled from hot working, artificially aged, cold worked

Precipitation hardening

By heat-treating certain alloys in a specific sequence, it is possible to give the material added strength. This is often called age hardening, because of the time dependence. Figure 2.8 shows a hypothetical phase diagram. A phase diagram is a representation of different phases present in an alloy at a given temperature and a given amount of alloying element. This will be used to illustrate the manner in which precipitation hardening is carried out.

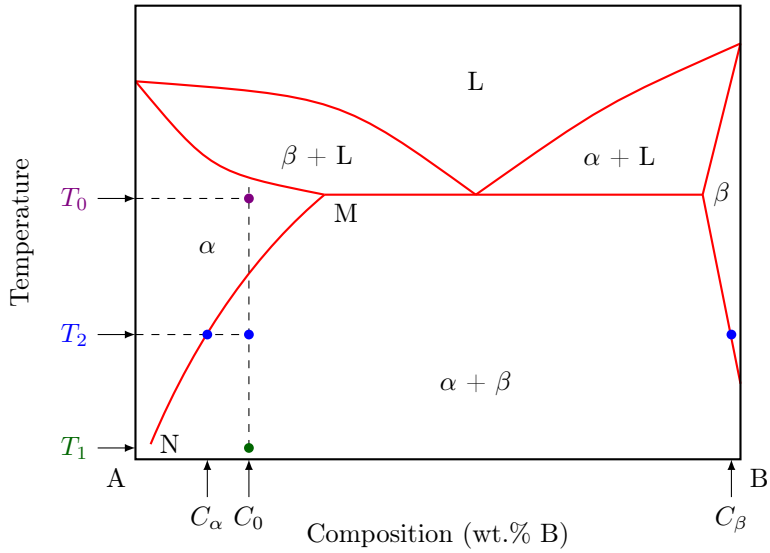

Figure 2.8: Hypothetical phase diagram [12]

For precipitation to occur, one needs a supersaturated alloy. To accomplish this, a material with an alloy concentration of C_0, is heated to a temperature T_0. After some time a solid state solution called the α-phase is formed. In this phase the alloy atoms substitute the aluminium atoms in the lattice, and equilibrium is created. Stage two consists of quenching the material, which means that the material is rapidly cooled to T_1, usually room temperature. By doing this instantaneously, the alloy atoms have no time to diffuse, resulting in a supersaturated solution.

The material is still relatively soft. For the material to gain strength, the alloying atoms have to diffuse together forming precipitates. This is done by heating the material to an intermediate temperature T_2. At this temperature, the alloying atoms are allowed to diffuse within the material, and with time, form β precipitates. These precipitates cause strains in the atomic structure, that inhibit dislocation motion and strengthens the material.

There is however, an optimal time in which age hardening occur, before the strength starts to diminish. At this point, the material should be cooled and the ageing process stopped. Ageing after this point, will cause the atomic structure to reach equilibrium, and the strains imposed on the lattice will diminish. There is also an optimal average size of the precipitates. If they are too large to be sheared, the dislocations have to bend around. However, they should not be so big that the average distance between them

gets to large. This leaves the material vulnerable to applied heat in the future from e.g. welding, where a heat affected zone, HAZ, will be created in the vicinity of the weld [12].

Work hardening

When metals are plastically deformed, dislocations move through the structure and pile up. In addition, new dislocations arise causing an increased dislocation density, i.e. the average distance between dislocations gets smaller. Dislocation-dislocation interactions are on average repulsive. So when dislocations move closer together, it gets harder to deform the material.

Hot working

Hot working is defined as work being done to the metal at temperatures above the recrystallisation temperature, T_{cr}. T_{cr} is the temperature where the grains start to grow and reshape into a stress free state (usually above 150 °C for aluminium [13]).

2.3.4 Classification of Aluminium Alloys

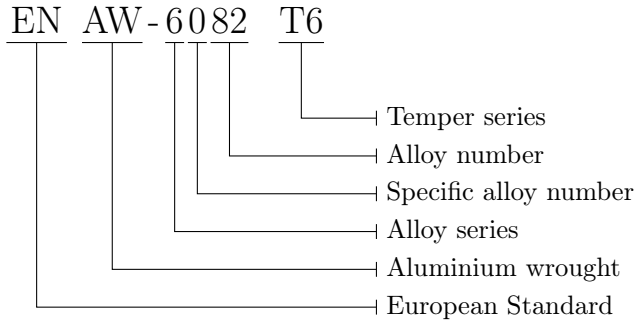

Figure 2.9: Classification of alloy EN AW-6082 T6

The aluminium alloy used in this thesis is denoted EN AW-6082 T6. It is normally used for rolled products, extruded and forged shapes and automotive applications [14]. As the Tables 2.1, 2.2, and 2.3 indicate, this is a high strength alloy with good formability that has been solution heat treated and artificially aged. Its main alloying elements are magnesium and silicon. However it also contains small amounts of manganese, iron, titanium, zinc, copper and chrome [15]. A more detailed description of the chemical composition of the individual plates can be found in Table 5.1. Figure 2.10 shows which elements different aluminium alloy series contain, and Table 2.3 sums up their physical properties.

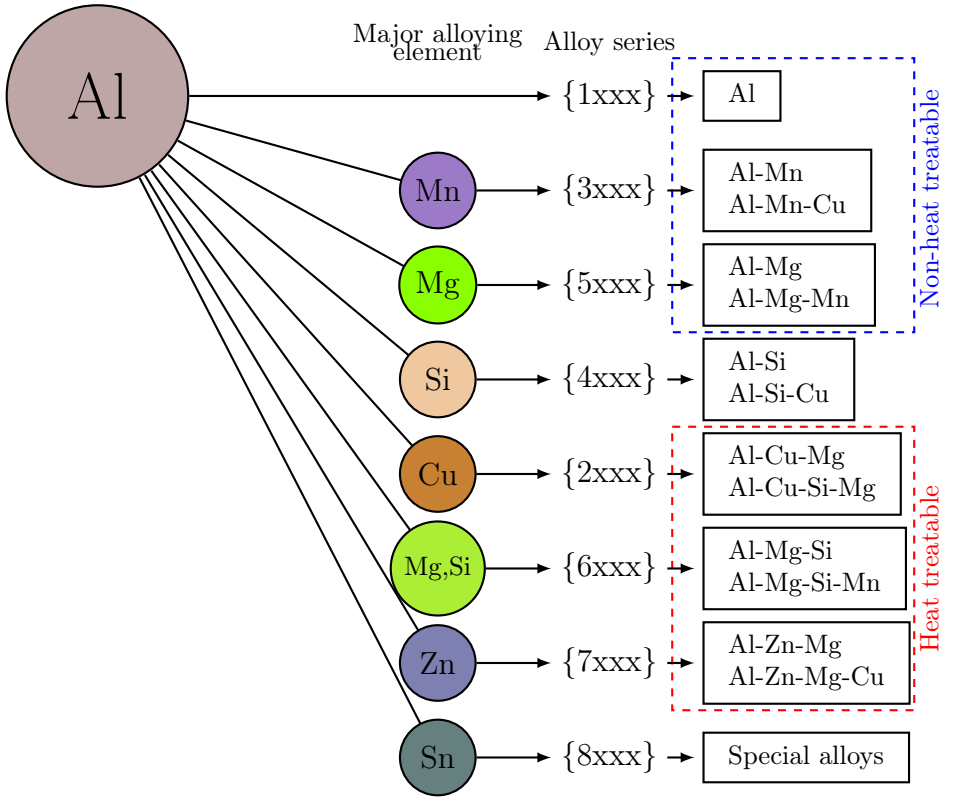

Figure 2.10: Aluminium wrought alloy designation system [13]

Table 2.3: Categorisation of different aluminium alloys [13]

Series	Properties
1xxx	Minimum 99% aluminium. Gives low strength, high formability, very good corrosive resistance, excellent electrical and thermal conductance and high reflectiveness
2xxx	High strength, good fatigue resistance and lowered corrosive resistance.
3xxx	Ductile alloys. Gives good formability, medium strength and good thermal conductivity.
4xxx	Low ductility alloys. Brittle behaviour and low formability. Mostly used in casting.
5xxx	Combination of medium strength and good formability.
6xxx	High strength alloys. Good formability.
7xxx	Very high strength alloys. Reduces the corrosion resistance.
8xxx	Stiff alloys. Good fatigue resistance. Lightweight.

2.4 Welding Theory

2.4.1 Background

Welding is a common material joining process, often used in fabrication of metal structures. The most common welding technologies include:

- Shielded metal arc welding (SMAW)
- Gas metal arc welding (GMAW)
- Tungsten inert gas welding (TIG)
- Laser welding
- Friction stir welding (FSW)

Usually there is some kind of filler material that combined with high temperatures melt the work pieces together. SMAW, also known as rod welding, is the most common method because of its easy use, low equipment cost and manoeuvrability in the field. Whereas with SMAW everything is built into the welding rod, GMAW has a more complicated process. Figure 2.11 illustrates the process of SMAW and GMAW welding.

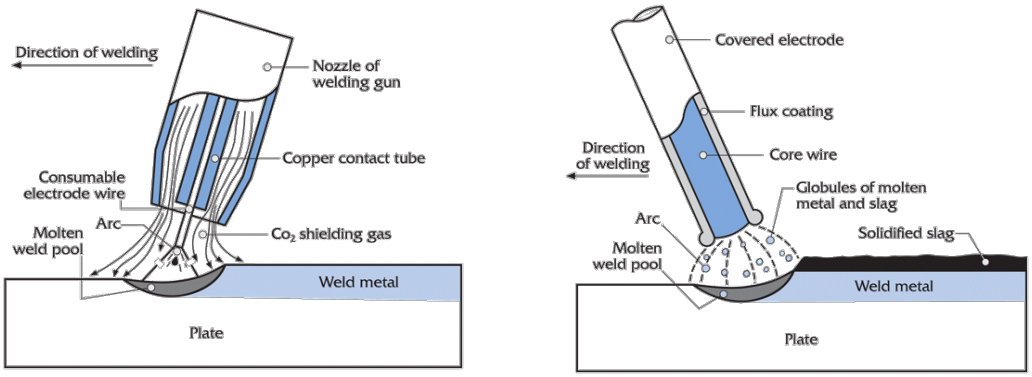

(a) Gas metal arc welding

(b) Shielded metal arc welding

Figure 2.11: Most common welding technologies [16]

2.4.2 Gas Metal Arc Welding

The welding method used for the plates in this thesis is gas metal arc welding (GMAW). GMAW uses a consumable electrode, which generates an electric arc between the electrode and the work piece. This heats the work pieces above melting temperature and causes them to fuse together [13].

An important advantage of GMAW is that, as Figure 2.11 illustrates, as opposed to SMAW, GMAW does not produce slag. When the electrode, the arc, or the welding metal comes in contact with atmospheric gases such as nitrogen or oxygen, it can cause fusion defects, porosity and weld metal embrittlement [17]. To avoid this, GMAW uses active or inert shielding gases that shield the process from these contaminants. In the

figure, CO_2 is used. This is an active gas, and is mostly used for welding steel. In non-ferrous metals such as aluminium, inert gases are more commonly used [13].

2.4.3 Heat Affected Zone

As explained in Section 2.3.3, age hardened aluminium alloys are vulnerable to over ageing. If the aluminium alloy has previously been age hardened at elevated temperatures, and then cooled at maximum hardening, the added ageing caused by the heat from the welding process, will cause the metal in the vicinity of the weld to lose much of its strength [12, 18].

2.5 Recht-Ipson Model

The Recht-Ipson model was originally developed for blunt nosed projectiles creating a plug when perforating a thin plate. By assuming that the plug leaves the plate with the same velocity as the residual velocity of the projectile and that the energy needed to perforate the plate is constant and independent of the initial and residual velocity, utilizing conservation of momentum and energy, Recht and Ipson [19] found the following expression for the residual velocity:

$$v_r = \left[\frac{m_p}{m_p + m_{pl}}\right] \left(v_i^2 - v_{bl}^2\right)^{1/2} \tag{2.12}$$

where m_p, is the mass of the projectile and m_{pl} is the mass of the plug. This expression considers both the energy lost to deformation and heat, and the energy lost due to the peripheral shear zone. The expression relies on knowing the ballistic limit velocity. However, if we know the residual velocity, solving for ballistic limit velocity yields:

$$v_{bl} = \left(v_i^2 - \left[\frac{m_p + m_{pl}}{m_p}\right] v_r^2\right)^{1/2} \tag{2.13}$$

When a projectile does not produce a plug at perforation, Equation 2.12 reduces to Equation 2.14. As explained in Section 2.1, this is normally the case when using conical or ogival projectiles. In this case the ballistic limit energy is lost due to plastic deformation, where the material is pushed laterally aside. This is also known as ductile hole growth, and the energy needed can be calculated analytically using the Cylindrical Cavity Expansion Theory [4]. This is covered in Section 2.8.

$$v_r = \left(v_i^2 - v_{bl}^2\right)^{1/2} \tag{2.14}$$

In 1978, Lambert and Jonas [5], developed a generalized expression based on the Recht-Ipson Model:

$$v_r = a\left(v_i^p - v_{bl}^p\right)^{1/p} \tag{2.15}$$

By inserting variables a and p into the expression, curve fitting tools can be used to create a best fit to more accurately describe experimental results. However, according to Ben-Dor et al. [20], the results cannot be said to be more accurate using this generalised expression.

2.6 Vickers Hardness

Hardness is a measure of resistance against localised plastic deformation in a material. Earlier, hardness was just a qualitative measurement of which minerals could scratch each other, arranging them on a scale from one to ten, in which one being talc and ten being diamond. Later, several quantitative methods of measuring hardness have been developed. It is important to know that there is no standardised measure of hardness, and one should be careful comparing hardness values from different hardness tests [12].

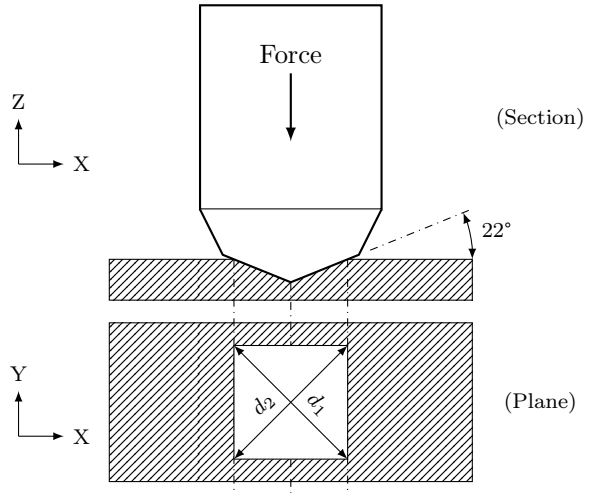

Figure 2.12: Vickers hardness testing

In this thesis, the Vickers hardness method (HV) has been used. This method uses a small diamond pyramid indenter, which is pushed with a predefined force into the test specimen for a predefined length of time (see Figure 2.12). Afterwards, the area of the indentation is measured and used to calculate the Vickers hardness by using Equation 2.16.

$$HV = 1.854 \frac{F}{\left(\frac{d_1 + d_2}{2}\right)^2} \tag{2.16}$$

where d_1 and d_2 is defined in Figure 2.12. Applied loads have two ranges. The micro range from 1-1000 grams and the macro range from 1-100 kg [21]. For Vickers hardness tests the results are generally the same, as long as the applied load is larger than 200 grams [21]. The resulting indentation is observed and measured under a microscope.

2.7 Constitutive Equations

A constitutive equation describes the relationship between stresses and strains in a material. An important constitutive relationship in structural engineering is Hooke's law:

$$\sigma = E\varepsilon \tag{2.17}$$

wehre E is the Young's modulus, σ is the stress and ε is the strain. This relationship, however, is only valid when the applied stresses are less than the yield stress, σ_0, of the given material. When the applied stresses exceed the yield strength, plastic deformation occurs and the material usually work-hardens. This response is often nonlinear and more complex models are needed.

2.7.1 Voce Law

To describe the material response after yielding, two frequently used work hardening relationships are the Power Law:

$$R(\varepsilon^p) = K(\varepsilon^p)^n \tag{2.18}$$

and the Voce Law:

$$R(\varepsilon^p) = \sum_{i=1}^{j} Q_i(1 - \exp(-C_i\varepsilon^p)) \tag{2.19}$$

where K, Q_i and C_i are constants and ε^p the equivalent plastic strain.

While the Power Law may be better suited for steels, the Voce law has been used in this thesis, because it more accurately describes the tendency for aluminium to saturate (i.e. the hardening rate tends to zero). Equation 2.19 gives the work-hardening variable, R, as a function of the equivalent plastic strain, ε^p. Q_i and C_i are material constants determined by curve fitting tensile test results, while j is usually 1, 2 or 3. The added values of Q_i, represent the saturated value of R, σ_{sat} [9].

2.7.2 Johnson-Cook Strength Model

Strain is not the only parameter that affects the material response. Voce law gives a good description of the work hardening in an aluminium tensile test, but it does not account for different material responses at elevated strain rates and temperatures.

$$\sigma_{eq} = [A + B(\varepsilon^p)^n][1 + C\ln\dot{\varepsilon}^{p*}][1 - T^{*m}] \tag{2.20}$$

Equation 2.20 shows a three term material model developed in 1983 by Johnson and Cook [22]. Here A, B, n, C and m are material constants, σ_{eq} is the equivalent stress, ε^p is the equivalent plastic strain, $\dot{\varepsilon}^{p*} = \dot{\varepsilon}^p/\dot{\varepsilon}^p_0$ is the dimensionless plastic strain rate given by the plastic strain rate, $\dot{\varepsilon}^p$, and a reference plastic strain rate $\dot{\varepsilon}^p_0$. $T^* = (T - T_r)/(T_m - T_r)$ is the homologous temperature given by the material temperature, T, room temperature,

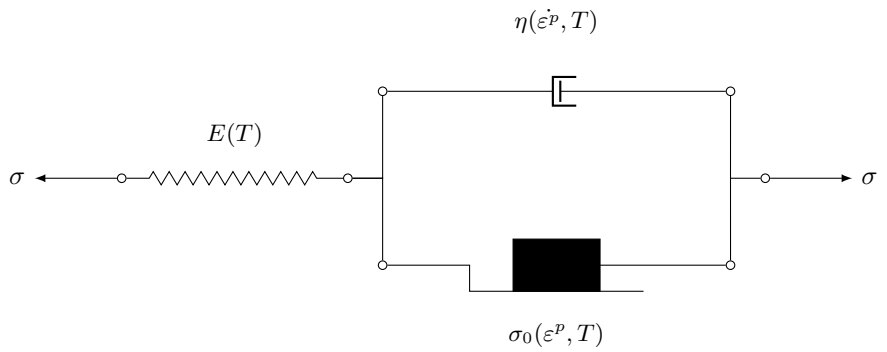

Figure 2.13: Rheological model of a thermoelastic-thermoviscoplastic material

T_r, and melting temperature, T_m. The change in temperature resulting from adiabatic heating due to the high strain rate is given as:

$$\Delta T = \int_0^{\varepsilon^p} \chi \frac{\sigma_{eq} d\varepsilon^p}{\rho C_p} \tag{2.21}$$

where χ is the Taylor-Quinney coefficient that represents the fraction of plastic work that is converted into heat, ρ is the material density and C_p is the heat capacity of the material.

The first term in Equation 2.20, is as described in the previous section, a power law work hardening model. The second term takes into account the strain rate to make the material response rate sensitive, while the third term implements temperature as a variable. Together, these three terms describes a thermoelastic-thermoviscoplastic material, as illustrated by the rheological model in Figure 2.13, where the spring illustrates the elastic area of the material, while the dashpot illustrates the rate dependency of the plastic area. The friction block represents the yield limit. All parts are dependent on the temperature.

At plastic strain rates, $\dot{\varepsilon}^{p*}$, smaller than 1, the logarithmic term may cause trouble. To handle this, the second term has been modified to get the Modified Johnson-Cook model:

$$\sigma_{eq} = [A + B\epsilon_p^n][1 + \dot{\varepsilon}^{p*}]^C[1 - T^{*m}] \tag{2.22}$$

As mentioned in the previous section, the power law is not ideal for describing work hardening in aluminum. Therefore, by substituting the power law term with the Voce work hardening term described in the previous section, we get a Johnson-Cook type material model better suited to describe the response of aluminium:

$$\sigma_{eq} = [A + \sum_{i=1}^{j} Q_i(1 - exp(-C_i\varepsilon^p))][1 + \dot{\varepsilon}^{p*}]^C[1 - T^{*m}] \tag{2.23}$$

2.7.3 Fracture Criterion

In literature there are many available fracture criteria. One that is easy to implement numerically, is the Cockcroft-Latham criterion. The IMPETUS Afea Solver manual [23] gives the following expression:

$$D = \frac{1}{W_c} \int_0^{\varepsilon^p} max(0, \sigma_1) d\varepsilon^p \tag{2.24}$$

where W_c is given as:

$$W_c = \int_0^{\varepsilon_f^p} \sigma_t d\varepsilon^p \tag{2.25}$$

Here σ_1 is the maximum principal stress, ε_f^p is the equivalent plastic strain at fracture and W_c is the plastic work per unit volume at fracture. The material will lose its shear strength once the damage parameter, D, has evolved from 0 to 1. As opposed to some other fracture criterea (e.g. the Johnson-Cook fracture criterion), the Cockcroft-Latham criterion does not directly account for neither strain rate nor temperature, however it is still applicable. Increased strain rate leads to higher stress and lower plastic strain, while higher temperature leads to lower stress and higher plastic strain. This means that W_c remains approximately constant. With only equivalent plastic strain and maximum principal stress as input variables, the Cockcroft-Latham fracture criterion can be implemented with ease [24].

2.8 Cylindrical Cavity Expansion Theory

Experience shows that perforation of plates by conical- and ogival-nose shaped bullets are dominated by ductile hole growth [4]. This means that no plug is produced, but rather the material is pushed laterally aside in highly localized plastic deformation. In the Recht-Ipson model, only the kinetic energy before and after impact is considered, and that the energy needed for perforation is a material constant. A theory called Cylindrical Cavity Expansion Theory, CCET, evaluates the perforation process, and analytically calculates the energy needed for perforation, with only geometry and material parameters as input [25].

The model was originally developed by Hill [26], however in this thesis a new adaption by Johnsen [27], which includes a Voce work hardening law, will be used. To model ductile hole growth, the target is idealised as thin independent layers that are compressed laterally, thus making the problem one-dimensional. The cavity is expanded from an initial diameter of zero to the diameter of the projectile.

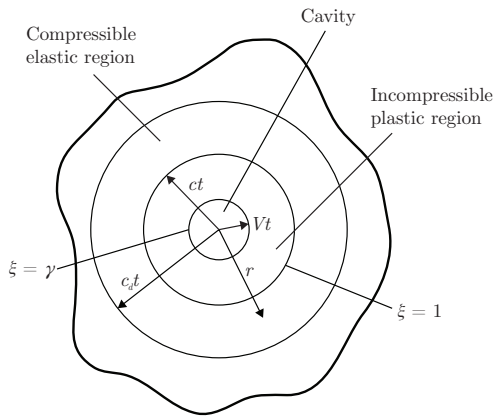

Figure 2.14: Response regions in the Cylindrical Cavity Expansion Theory [28]

Figure 2.14 shows the different response regions associated with CCET. The compressible elastic region has a Young's modulus, E , and Poisson's ratio, ν, while the incompressible plastic region is evaluated using Voce work hardening law. Thus, we get the material response in Equation 2.26. Where σ and ε are true stress and logarithmic strain respectively. Q_i and C_i are Voce law constants.

$$\sigma = \begin{cases} E\varepsilon, & \sigma \leq \sigma_0. \\ \sigma_0 + \sum_{i=1}^{2} Q_i(1 - \exp(-C_i\varepsilon)), & \sigma > \sigma_0. \end{cases} \tag{2.26}$$

With these assumptions, Johnsen found the ballistic limit to be:

$$V_{bl} = \left(\frac{2\sigma_s}{\rho_p}\frac{h}{(L + k_1 l)}\right)^{1/2}\left(1 + C + \frac{2}{3}C^2\right)^{1/2} \tag{2.27}$$

and the residual velocity:

$$v_r = \left(v_i^2 - v_{bl}^2\right)^{1/2} \left(1 - C + \frac{1}{2}C^2\right) \tag{2.28}$$

C accounts for the radial target inertia:

$$C = \frac{h}{(L + k_1 l)} \frac{\rho_t}{\rho_p} B_0 N(\psi) \tag{2.29}$$

k_1 and $N(\psi)$ are functions of the ogive shaped nose:

$$k_1 = \left(4\psi^2 - \frac{4\psi}{3} + \frac{1}{3}\right) - \frac{4\psi^2(2\psi - 1)}{\sqrt{4\psi - 1}} \arcsin\left[\frac{\sqrt{4\psi - 1}}{2\psi}\right] \tag{2.30}$$

$$N(\psi) = 8\psi^2 \ln\left(\frac{2\psi}{2\psi - 1}\right) - (4\psi + 1) \tag{2.31}$$

σ_s is the quasi-static stress required to open the cavity:

$$\sigma_s = \frac{1}{\sqrt{3}} \left[\sigma_0(1 - 2ln\gamma) - 2\sum_{i=1}^{2} Q_i \left(\ln\gamma + \frac{1}{2}\int_0^{1-\gamma^2} \frac{x^{C_i/\sqrt{3}}}{1 - x} dx\right)\right] \tag{2.32}$$

and γ is the cavity surface:

$$\gamma = \sqrt{\frac{2(1 + \nu)\sigma_0}{\sqrt{3}E}} \tag{2.33}$$

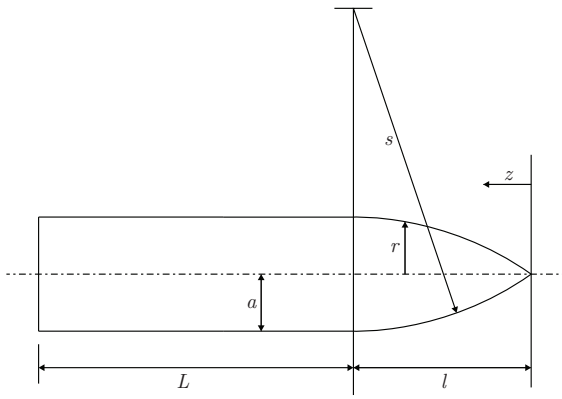

Figure 2.15: Ogival projectile with geometrical entities defined [27]

Figure 2.15 shows the geometry of an ogival projectile. Some of the entities are defined in the given equations. The rest can be found in the original adaption by Johnsen [27].

2.9 Software

2.9.1 Impetus

IMPETUS Afea Solver®, hereafter denoted IMPETUS Afea, is an explicit finite element software. IMPETUS Afea utilizes the GPU, graphical processing unit, instead of the CPU, central processing unit, to optimise parallelisation [23]. IMPETUS Afea has a very robust and accurate code with few input parameters. For instance there is only one contact algorithm (penalty), no elements with zero energy modes and only Lagrangian based description of motion [23]. This makes IMPETUS Afea computationally more expensive, but it also makes it nice and efficient to work with.

In this thesis two different volume elements in IMPETUS Afea have been used; a linear 8-node hexahedron element and a cubic 64-node hexahedron. The cubic 64-node hexahedron element can be seen in Figure 2.16. This higher order element is very good at describing large plastic deformations. The linear 8-node hexahedron is stiffer [23], but this element has only been used in a distance from the impact zone where deformations are almost non-existent.

A typical input file used in IMPETUS Afea is provided in Appendix D.

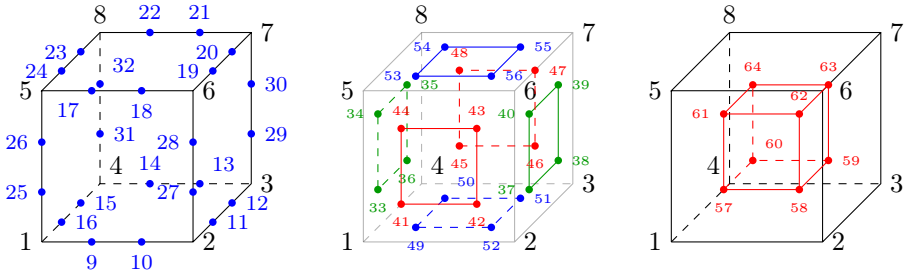

Figure 2.16: 64-node cubic hexahedron [23]

2.9.2 Other Software

MATLAB® is both a software and a programming language, which specialises in numerical computation. In this thesis it has been used for numerous tasks, and many scripts can be found in the Appendix.

Microsoft Excel® is a spreadsheet software. Mostly used for data viewing and some easier calculations. An-add in function to Excel, called Solver, has been utilised for curvefitting with least squares method.

Abaqus CAE® is another finite element software. It has a more developed graphical user interface than Impetus Afea. In this thesis it has been used for drawing element meshes for use in Impetus Afea.

LaTeX is an open source code used to typeset this document. Powerful sub-packages like TikZ [29] and PGFPlots [30] have been used making vector graphics and data plots.

CHAPTER 3

Preliminary Study

With few material samples available, it was important getting the ballistic experimental testing done right on the first try. Therefore, a preliminary study has been carried out, investigating the material properties of the base material and the HAZ. This study includes finding material data from the literature, using CCET to obtain ballistic limit velocities, setting up a Recht-Ipson curve and finding the Vickers hardness (HV) across the HAZ.

3.1 Material Data

Since material testing had not yet been done, material data had to be found from literature. After reviewing several papers on the EN AW-6082 T6 alloy, the material data from Wang et al. [18] were chosen. From this paper $Q_1, Q_2, C_1, C_2, E, \nu$ and σ_0 have been collected, and used as input for CCET. The parameters can be seen in Table 3.1.

Table 3.1: Material parameters from Wang et al. [18]

Parameter	Value
E	70 GPa
σ_0	240 MPa
ν	0.3
Q1	72 MPa
Q2	52 MPa
C1	3196
C2	29

3.2 Choosing Initial Velocity

The theory behind CCET is covered in Section 2.8. In this section, the CCET method will be used to analytically find the ballistic limit velocity (v_{bl}) and residual velocity (v_r) for each plate thickness. The analysis was performed using a Matlab script developed on the basis of the CCET adaption done by Johnsen [27]. The Matlab script can be

found in Appendix A. Results from the analyses are given in Table 3.2. The table also gives a chosen initial velocity for each plate thickness, to be used in subsequent ballistic experiments. The chosen initial velocities lay 50 m/s above the ballistic limit, to ensure full perforation. Firing the projectiles at velocities much higher than the ballistic limit is not going to yield good results. The Recht-Ipson curve is very steep just after v_{bl}, as can be seen in Figure 3.1. Obtaining results in this velocity range, makes it easier and more accurate curve fitting experimental data and finding v_{bl}.

Table 3.2: Ballistic limit velocities and subsequent chosen initial velocities for the ballistic experiments

Plate	v_{bl} given by CCET	Chosen v_i
10 mm	379 m/s	429 m/s
20 mm	553 m/s	603 m/s
30 mm	698 m/s	748 m/s

3.3 Recht-Ipson Model

For the theory behind the Recht-Ipson model, the reader is referred to Section 2.5. Using Equation 3.1 and ballistic limit velocities calculated in the previous section, the Recht-Ipson curves seen in Figure 3.1, have been plotted. These curves are used as a reference to evaluate the results while performing ballistic experiments.

$$v_r = (v_i^2 - v_{bl}^2)^{1/2} \tag{3.1}$$

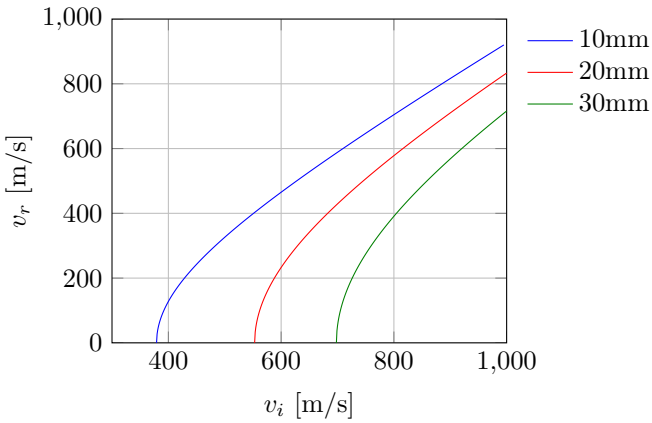

Figure 3.1: Recht-Ipson curves with v_{bl} from CCET

3.4 Hardness Measurements

To find the heat affected zone (HAZ), Vickers hardness tests have been performed for each plate thickness. These tests give the information needed for choosing the striking

positions. The hardness tests where performed by K. S. Rostad at NTNU Material Science and Engineering [31]. Figure 3.2 shows the results.

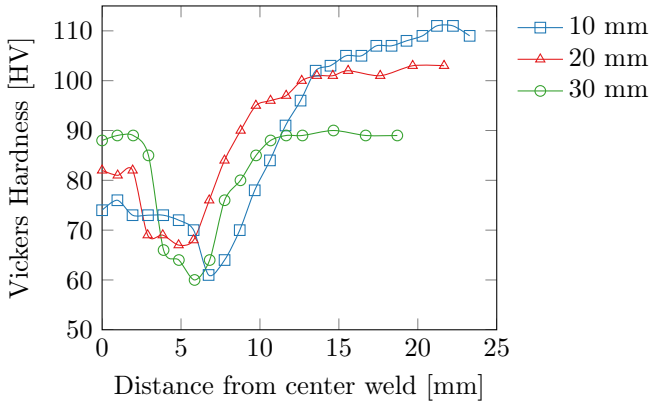

Figure 3.2: Hardness measurements from mid thickness of the three plates

On the basis of the hardness measurements, the distances from the weld centerline at which the projectiles should hit, were decided. Table 3.3 shows what distance each target zone corresponds to. Note that the hardness measurements have only been done in center thickness of each plate. The results are considered adequate as a preliminary measure. In ballistic experiments there are usually some deviations between wanted target position and the actual striking position.

Table 3.3: Target zone distances. All measurements from center weld.

Plate	Weld [mm]	HAZ [mm]	Base material [mm]
10 mm	0	7	20+
20 mm	0	5	15+
30 mm	0	6	15+

CHAPTER 4

Ballistic Experiments

4.1 Experimental Work

Ballistic experiments were conducted in a controlled environment in a laboratory at NTNU. A protective tank was used, in which the experimental rig was set up. A sketch of the rig setup can be seen in Figure 4.1. 7.62 mm APM2 hard steel core projectiles were fired from a smooth-bore Mauser rifle, triggered remotely from a safe distance outside the protective tank. The projectile geometry can be seen in Figure 4.2 and the trigger mechanism in Figure 4.3a. At the tip of the barrel a thin metal sheet connected to the high speed camera was placed. When broken, the high speed camera started recording. The velocity of the projectile was retrieved from high speed camera footage, taken by a Phantom V1610 at 70 000 frames/s. To achive the desired impact velocity, APM2 projectiles were loaded with a certain amount of gunpowder chosen from previous experience at SIMLab Ballistic Laboratory. Target plates were firmly clamped inside the experimental rig (Figure 4.3b).

The objective of the experiments was observing the difference in residual velocity, v_r, when projectiles perforated the base material, the heat affected zone (HAZ) and the weld. Three different plate thicknesses were used; 10 mm, 20 mm and 30 mm. The weld was milled flush with the plate in order to have equal thickness in all target zones. Up to 10 shots were fired in each plate at a predefined velocity and at predefined target locations, found in the preliminary study (see Chapter 3). Chosen striking positions were based on the hardness curves provided by K. Rostad [31]. For direct comparison, equal initial velocity in each test was desirable, however, it is difficult to get the exact same velocity using gunpowder. Results were curve fitted using Recht-Ipson and then ballistic limit curves from each plate and each target zone were compared.

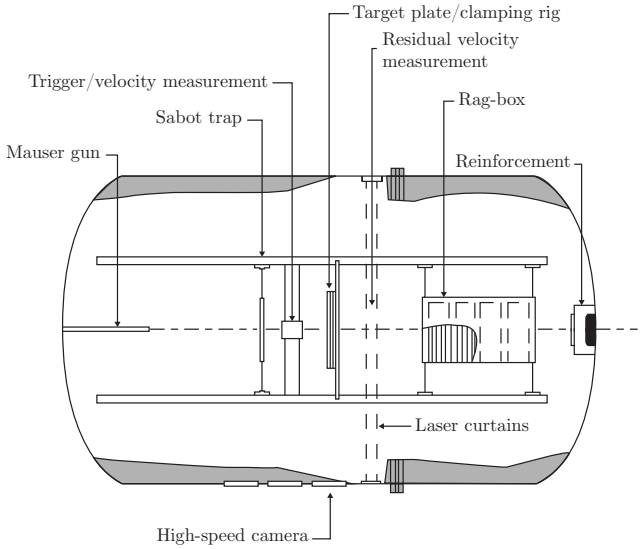

Figure 4.1: Experimental rig [28]

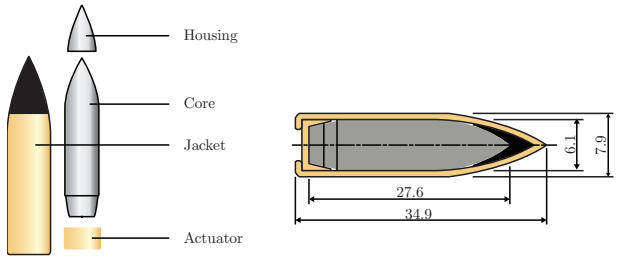

Figure 4.2: APM2 projectile geometry and composition [32]

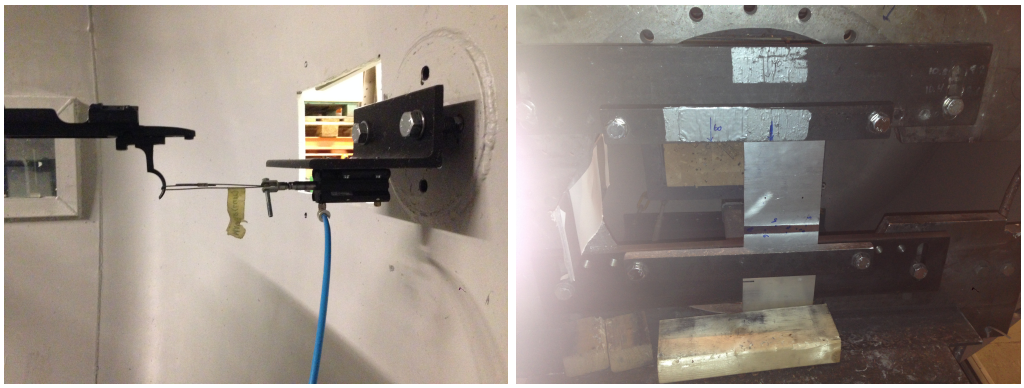

(a) Trigger mechanism **(b)** Target mount

Figure 4.3: Experimental setup

4.2 Results

In this section, results from the ballistic experiments are presented. Initially every ballistic experiment has been examined and either approved, adjusted or discarded. Only two results were discarded. Since limited material were available for testing, some of the results may not be satisfactory. This is discussed further in Section 4.3.

The residual velocity, v_r, from the tests were measured in the horizontal direction. Resulting in non-conservative results for projectiles with pitched exits. Because of this, v_r has been adjusted in a number of tests to account for the vertical velocity component, using standard trigonometry.

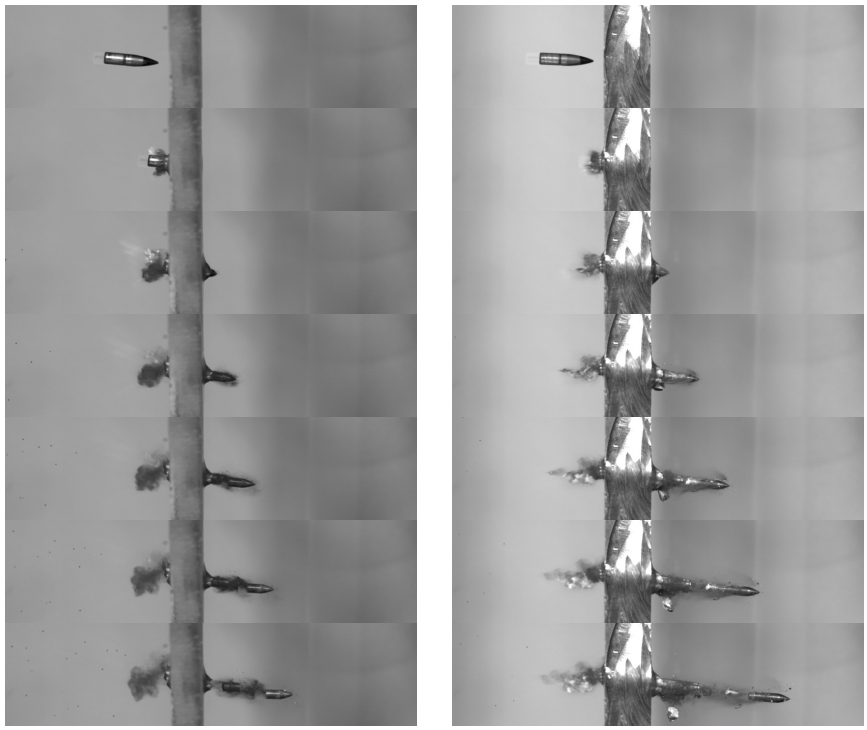

(a) Pitched entry and split projectile **(b)** Close to the edge of the plate

Figure 4.4: Discarded ballistic tests

Figure 4.4 shows the two tests that were discarded and therefore excluded from curve fitting with Recht-Ipson. Figure 4.4a shows projectile 20-3 entering the plate at a pitched angle. This is backed up by Figure 4.8b lower right perforation, also showing that this projectile must have been pitched at impact. The amount of energy needed for perforation is higher at this angle than for a horisontal flying projectile, and as Figure 4.6 shows, the residual velocity lies below the Recht-Ipson fitted curve. Figure 4.4b shows projectile 30-5 passing through the plate. It clearly shows the edge of the plate buckling outward as the projectile perforates the plate. This is why the result has been discarded.

Table 4.1 gives an overview of the results from the ballistic experiments. Figures 4.5, 4.6

and 4.7 give illustrations of the plates and positions of the individual impacts. They also give the hardness curves across the HAZ and the Recht-Ipson curves for the weld, HAZ and base material. These hardness curves are adopted from Chapter 5, and are not the same as hardness curves in Chapter 3. On page 36 and 37, pictures of the front and back of perforated plates are shown in Figure 4.8 and 4.9 respectivly. A perforation's position is the same in both the front picture and back picture of each plate. Table 4.2 gives the results from curve fitting the experimental results with Recht-Ipson.

Table 4.1: Results from ballistic experiments

Thickness [mm]	Test #	Target	Gunpowder [grains][a]	v_i [m/s]	v_r [m/s]	Comment
10	1	Base	27	502.1	377.3	Some fragmentation
	2	Base	27	468.8	317.7	OK
	3	Base	24	390.6	179.2	Some fragmentation
	4	Base	24	427.8	240.7	Some fragmentation
	5	HAZ	24	-	-	No results [b]
	6	HAZ	24	426.6	284.2[c]	Jacket intact
	7	HAZ	24	405.6	255.2	Jacket intact
	8	Weld	24	410.6	237.0[c]	Jacket intact
	9	HAZ	24	481.3	378.7[c]	Jacket intact
20	1	Base	33	627.4	398.2	OK
	2	Base	33	593.6	332.9	OK
	3	Base	31	551.1	229.9	Results omitted[d]
	4	Base	31	573.3	316.7	OK
	5	HAZ	31	547.4	319.8[c]	OK
	6	HAZ	31	564.1	318.9[c]	Only half the core exited
	7	Weld	31	556.7	321.3	OK
	8	HAZ	33	607.3	402.6[c]	OK
	9	HAZ	33	587.1	378.5	OK
30	1	Base	41	726.8	457.2	Close to edge
	2	Base	41	754.5	489.7	OK
	3	Base	36	628.0	214.5	OK
	4	Base	36	699.1	399.5	OK
	5	HAZ	36	651.0	364.9	Results omitted[e]
	6	HAZ	36	653.4	337.9[c]	OK
	7	Weld	36	670.7	331.7[c]	Close to projectile #6
	8	HAZ	36	695.4	431.7[c]	OK
	9	HAZ	36	670.7	341.5[c]	OK
	10	HAZ	36	648.5	325.5	OK

[a] 1 grain = 64.8 milligrams
[b] Camera malfunction
[c] Residual velocity adjusted because of pitched exit
[d] Results omitted because of pitched projectile entry and exit. In addition the projectile split in half
[e] Results omitted because projectile hit too close to the edge of the plate

4.2.1 10mm Plate

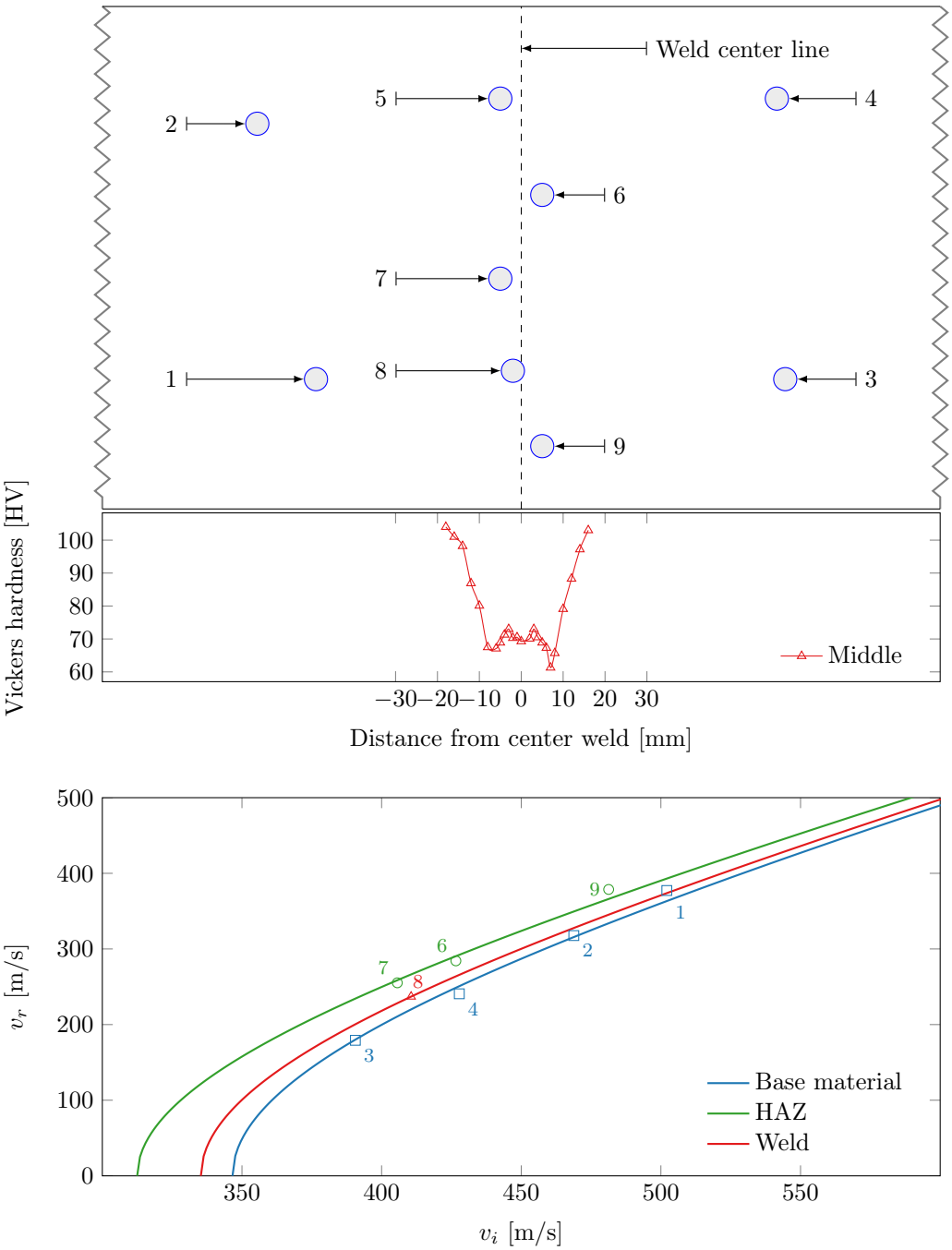

Figure 4.5: 10mm plate with numbered ballistic tests, a Vickers hardness profile and Recht-Ipson curves

4.2.2 20mm Plate

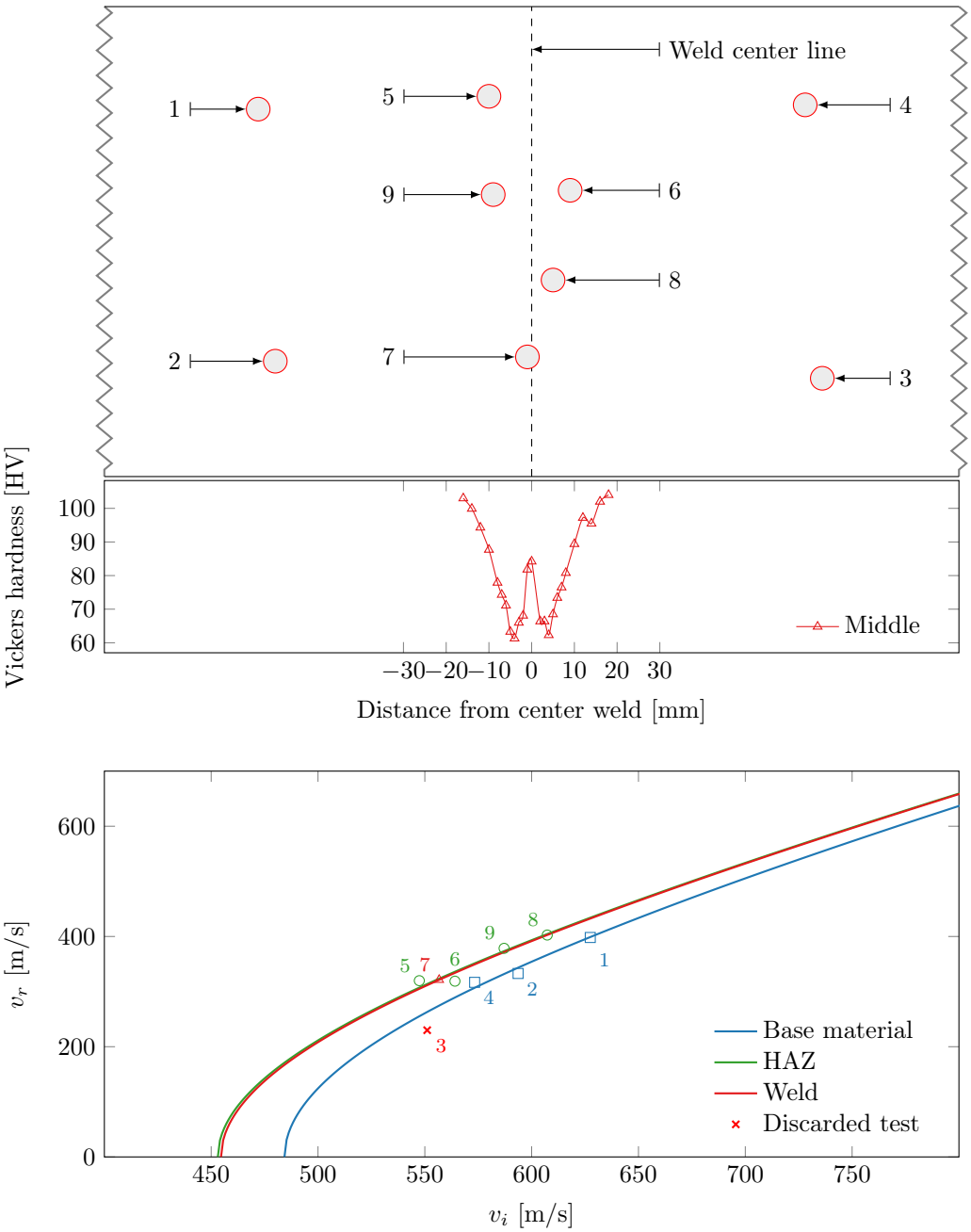

Figure 4.6: 20mm plate with numbered ballistic tests, a Vickers hardness profile and Recht-Ipson curves

4.2.3 30mm Plate

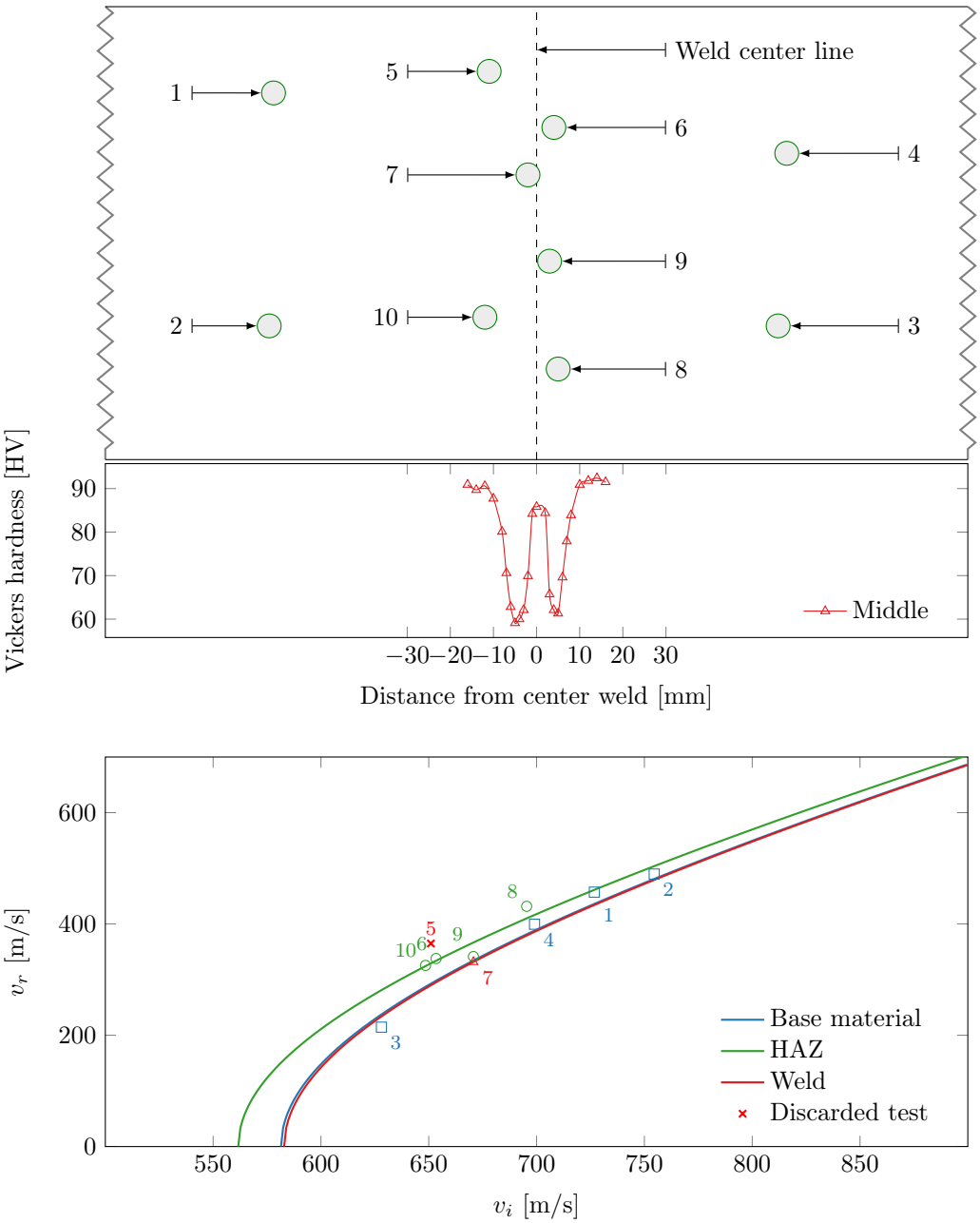

Figure 4.7: 30mm plate with numbered ballistic tests, a Vickers hardness profile and Recht-Ipson curves

(a) Front of 10mm plate

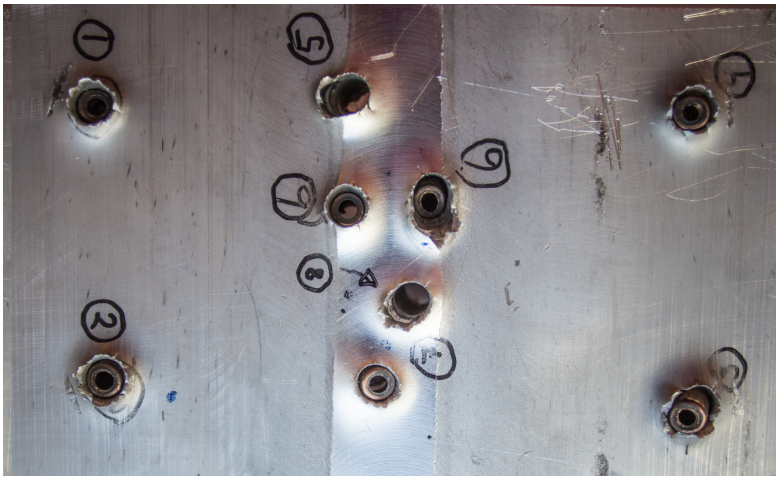

(b) Front of 20mm plate

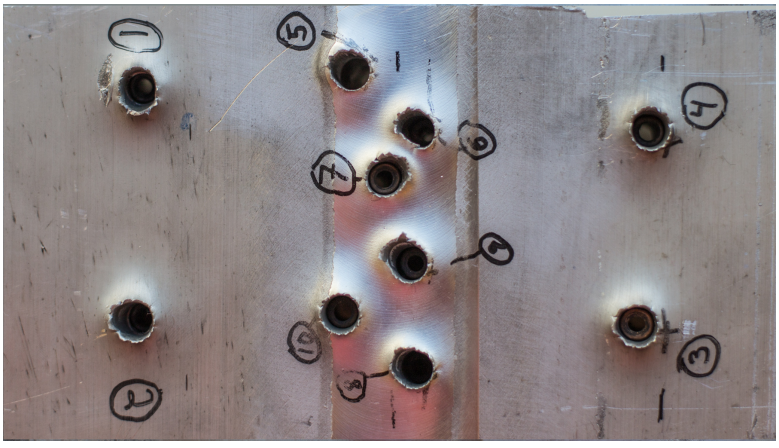

(c) Front of 30mm plate

Figure 4.8: Pictures of the perforated plates - Front

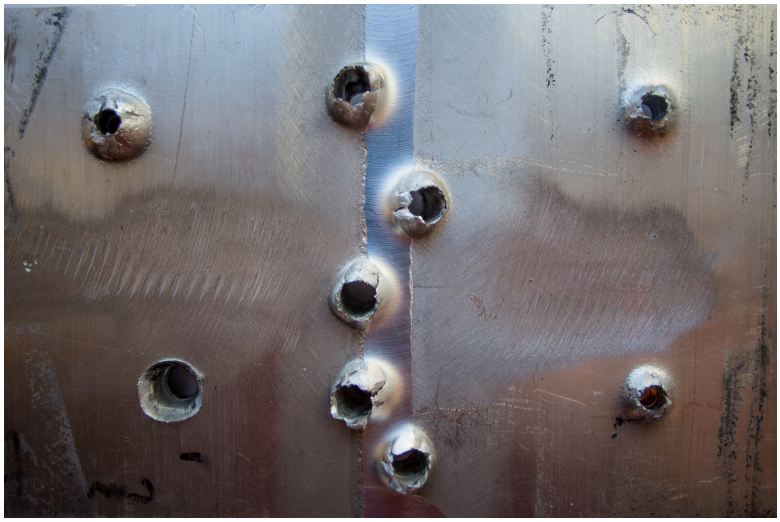

(a) Back of 10mm plate

(b) Back of 20mm plate

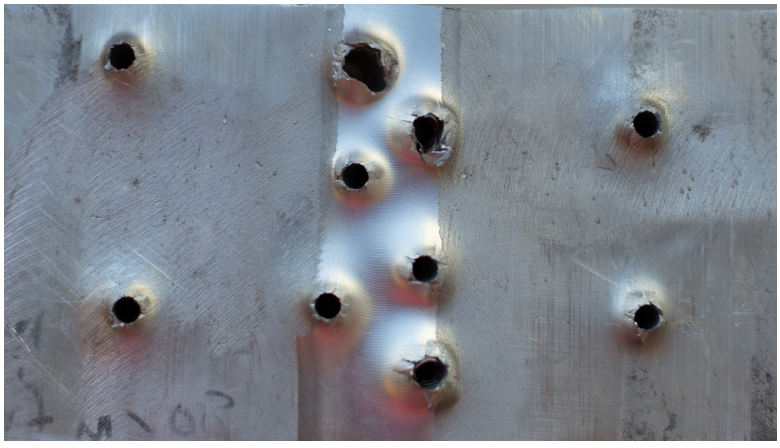

(c) Back of 30mm plate

Figure 4.9: Pictures of the perforated plates - Back

4.3 Discussion of Results

Different Recht-Ipson curves from each target zone for each plate thickness were expected. The results, however, were affected by a small margin for error in striking position, due to the short distances between base material, HAZ and weld. Pictures of the perforated plates can be seen in Figure 4.8 and 4.9, and it is seen that the perforations are quite close. Because of few samples available, the limit of how close striking positions could be, had to be lowered. This may have caused one test to influence the next, by e.g. work hardening in the vicinity of the impact zone.

Results from curve fitting are shown in Table 4.2.

Table 4.2: Results from curve fitting of experimental data

Plate	Zone	v_{bl}	Difference from base material
10 mm	Base material	347 m/s	-
	HAZ	312 m/s	-10%
	Weld	335 m/s	-3%
20 mm	Base material	484 m/s	-
	HAZ	453 m/s	-6%
	Weld	454 m/s	-6%
30 mm	Base material	581 m/s	-
	HAZ	562 m/s	-3%
	Weld	583 m/s	1%

4.3.1 10 mm Plate

As can be seen in Table 4.2 and Figure 4.5, a clearly softer response in the HAZ was observed. The weld however, gave a response closer to the base material. This was somewhat unexpected based on the initial hardness measurements, which showed a hardness closer to the HAZ. This could be due to normal scatter, as only one projectile was fired through the weld. However, every shot fired through the weld and the HAZ for the 10 mm plate, retained its jacket through the plate. One of these projectiles can be seen in Figure 4.10. As opposed to projectiles fired through the base material, where all lost their jacket at impact. According to ductile hole growth theory, when a projectile perforate a target with the jacket intact, it produces a larger hole. This will cause the plate to absorb more energy, giving lower residual velocities than expected.

4.3.2 20 mm Plate

In Figure 4.6, the distinction in the Recht-Ipson curves between the base material and the other zones is clearly seen. However, there is no distinct difference between the weld and HAZ curves, even though the hardness measurements in Figure 4.6 show a clear distinction in hardness. This could, again, be due to normal scatter, as only one test have perforated the weld. However as the projectile entered the target slightly skewed, it exited in the HAZ. This could have given less restistance.

Figure 4.10: Projectile that passed through HAZ with brass jacket intact compared to the steel core.

4.3.3 30 mm Plate

As the hardness profile in Figure 4.7 indicates, the hardness of the weld for the 30 mm plate is almost at base material values, while the hardness in the HAZ lies much lower. This coincides well with what we see in the Recht-Ipson curves in Figure 4.7.

CHAPTER 5

Material Testing

5.1 Material Composition

The chemical compositions of the three different plates of alloy EN AW-6082 T6 are given in Table 5.1. The compositions have been given by the plate manufacturer, Hydro Aluminium.

Table 5.1: Chemical composition of EN AW-6082 T6 in wt.%

	Si	Mg	Mn	Fe	Ti	Zn	Cu	Cr	Al
10 mm	0.93	0.60	0.55	0.18	0.011	0.002	0.008	0.011	Remainder
20 mm	0.99	0.63	0.56	0.17	0.018	0.006	0.025	0.011	Remainder
30 mm	0.97	0.63	0.54	0.16	0.013	0.004	0.004	0.013	Remainder
Eurocode[a]	0.7-1.3	0.6-1.2	0.4-1.0	0.50	0.10	0.20	0.10	0.25	Remainder

[a]Chemical composition of EN AW-6082 according to NS-EN 573-3 Table 6

As Table 5.1 shows, most of the compounds are within the limits of the standard. The major differences are copper, zinc and chromium with smaller amounts than the standard requires.

There are also relatively large internal differences between the plate thicknesses. It is hard to say how much these differences interfere with the overall results of this study, but since the amounts in question are relatively small, the effect has been regarded as minor. These deviations are a result of different cast ingots for each plate extrusion, and the fact that it is practically impossible to produce two cast ingots with indentical chemical compositions [33].

5.2 Hardness Measurement

To more accurately locate the HAZ in the material, Vickers hardness tests have been performed by Dr. Ida Westerman at SINTEF Materials and Chemistry. For each plate, three strings across the weld and one string in the base material (in thickness direction) were measured. Each string across the weld contained an average of 20 measurements, while the strings over the thickness had 5, 10 and 15 measurements respectively. The string over the thickness were taken in the base material. Before testing, the specimens were polished

to obtain a homogenous surface. The tests were performed in a Struers DuraScan fully automatic Vickers hardness testing machine. 50 N of pressure were applied for 15 seconds in each measurement, then each indentation were measured and registered. Tables with all the numerical values can be found in Appendix C.

Figure 5.1, 5.2 and 5.3 show the results from the measurements. All the figures have **(a)** a hardness plot for the three strings across the weld, **(b)** a plot showing a cross section of the weld with color graded hardness measurements and a smooth curve between the lowest measurement in each string on each side of the weld center line, and **(d)** a plot of the measurement string in the thickness direction of the base material.

5.2.1 10 mm Plate Results

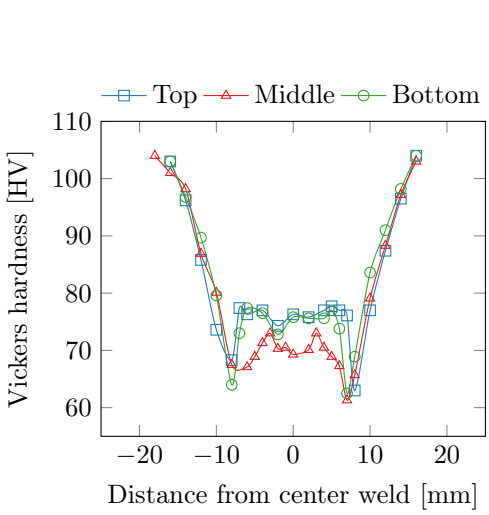

(a) Hardness measurements across weld

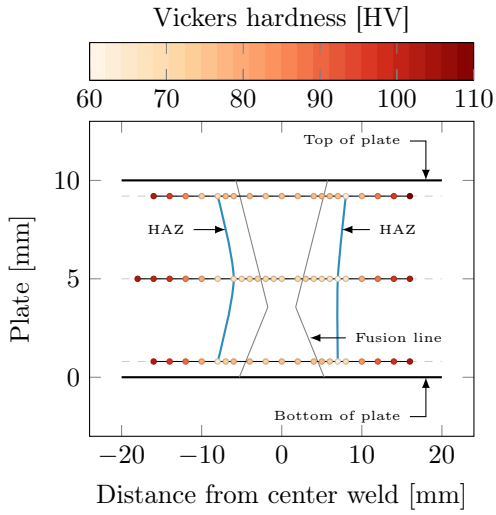

(b) Vickers hardness and weld geometry

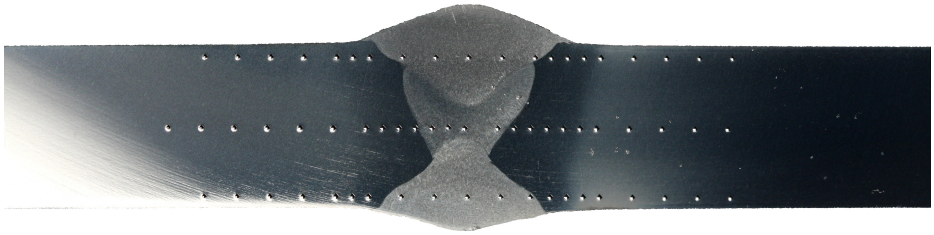

(c) Cross section of welded 10 mm plate with Vickers indentations

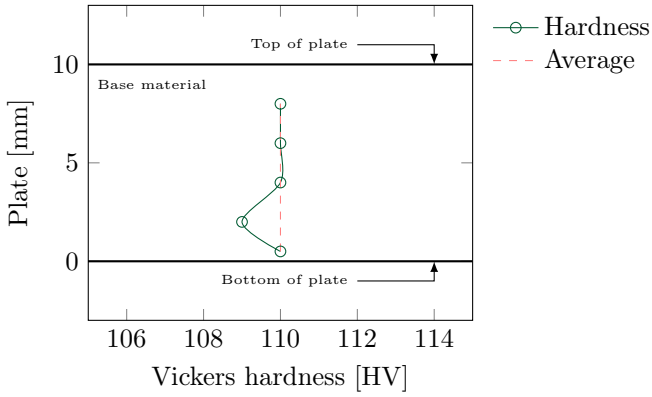

(d) Hardness over thickness in base material

Figure 5.1: Vickers hardness measurements from the 10 mm plate

5.2.2 20 mm Plate Results

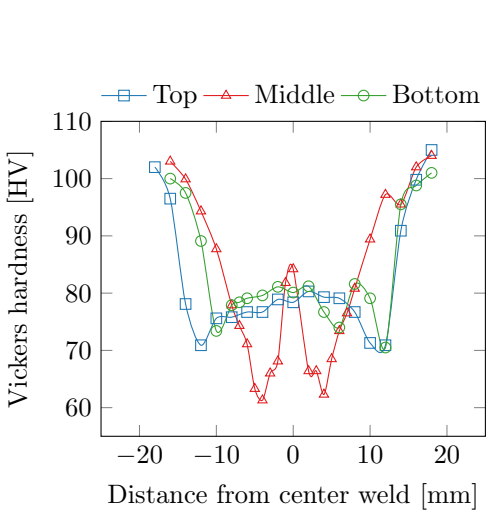

(a) Hardness measurements across weld

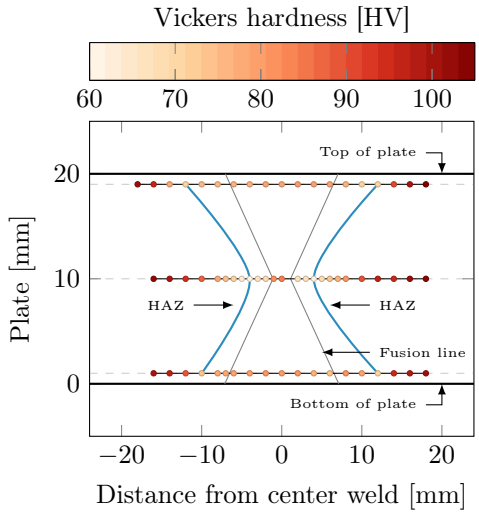

(b) Vickers hardness and weld geometry

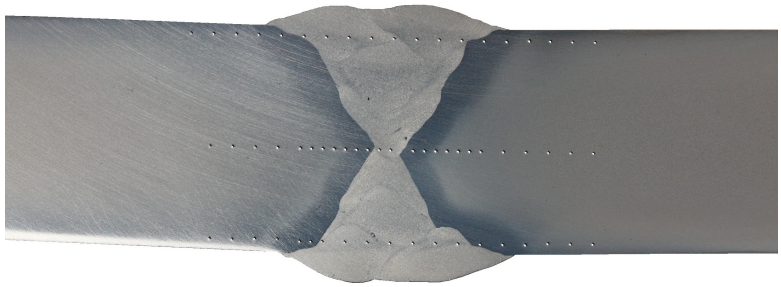

(c) Cross section of welded 20mm plate with Vickers indentations

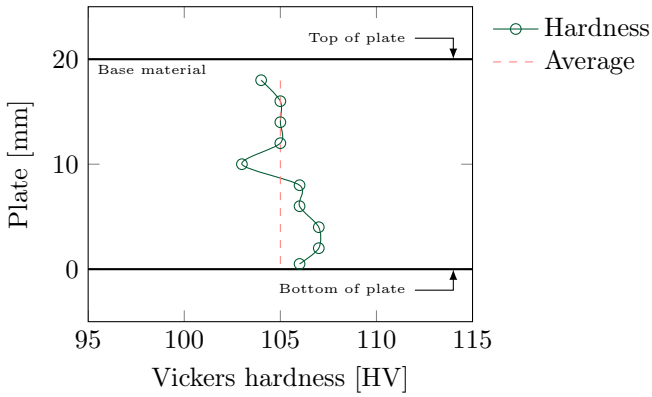

(d) Hardness over thickness in base material

Figure 5.2: Vickers hardness measurements from the 20 mm plate

5.2.3 30 mm Plate Results

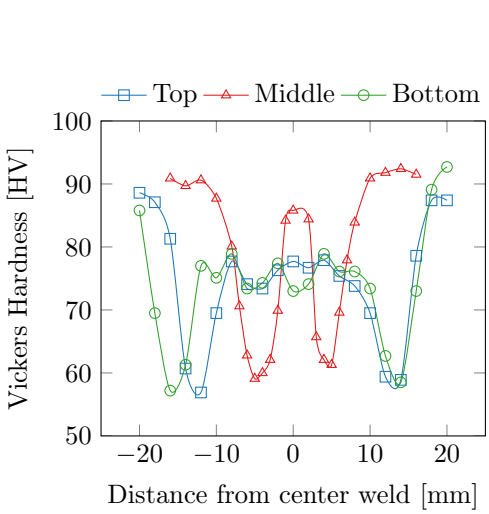

(a) Hardness measurements across weld

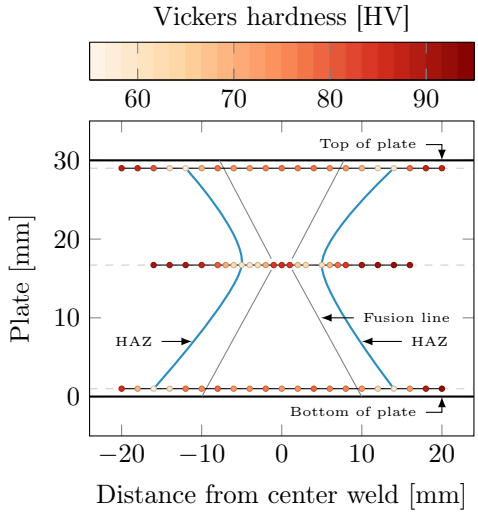

(b) Vickers hardness and weld geometry

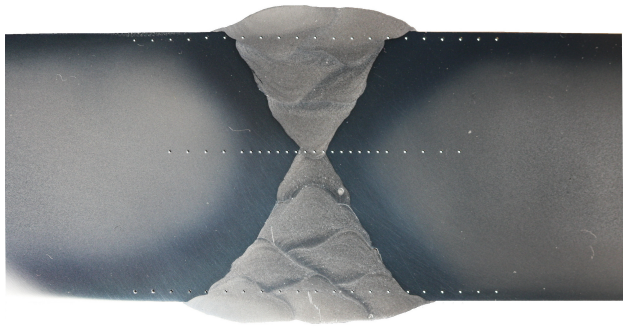

(c) Cross section of welded 30 mm plate with Vickers indentations

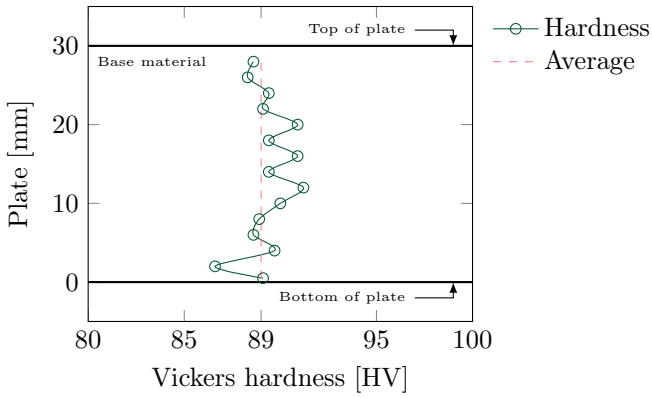

(d) Hardness over thickness in base material

Figure 5.3: Vickers hardness measurements from the 30 mm plate

5.3 Discussion of Results

As Figures 5.1c, 5.2c and 5.3c show, the polishing process actually makes it possible to see the HAZ and all the different weld layers. The different hardness values give different surface finish when polished, and the light reflects differently. In Figure 5.1b, 5.2b and 5.3b the Vickers hardness is represented by color, and a smooth line is plotted between the lowest measurement in each string on each side of the weld center line. For the 20 mm and 30 mm plate it is clear that this line follows the fusion line of the weld at an almost equal offset distance. This distance is approximately 6 mm for the 20 mm plate, and 7 mm for the 30 mm plate. For the 10 mm plate this line is more or less vertical, and the distance from the weld fusion line is about 6 mm. These results are in good agreement with the preliminiary hardness measurements in Chapter 3.

5.4 Width of the HAZ

The width of the HAZ, b_{haz}, can be extracted from the hardness measurements. b_{haz} says how far from the weld centerline the material is unaffected by the welding process. The series of measurements over the plate thickness give the hardness in the base material, and using these results, an approximate b_{haz} can be found. For instance, the middle measurements from the 30 mm plate, reach the base material hardness after only 10 mm from center weld. The top and bottom measurements reach the base value at about 18 mm. So a conservative b_{haz} measure for this plate would be 25 mm.

Some of the strings do not have measurements far enough from weld center line to reach the base material hardness level. A trend from the hardness curves can though be seen, that this level would have been achieved with one or two extra measurements. The b_{haz} values given in Table 5.2, have been chosen on the conservative side.

According to Eurocode 9, NS-EN 1999-1-1 [34],b_{haz} for this type of weld is measured as shown in Figure 5.4. In thinner plates, Eurocode assumes a vertical HAZ, but for thicker plates a curved boundary with radius b_{haz} can be assumed [34].

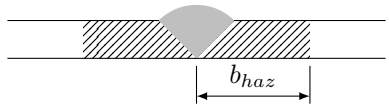

Figure 5.4: Definition of b_{haz} according to NS-EN 1999-1-1 [34]

Table 5.2 sums up the results. The width of HAZ is generally overestimated by Eurocode 9. Especially for the 20 mm and 30 mm plates. Here the differences were 57% and 63% respectively.

Table 5.2: Comparison of HAZ width

Plate thickness	10 mm	20 mm	30 mm
b_{haz} approximated	25 mm	20 mm	25 mm
b_{haz} according to Eurocode 9[a]	30 mm	35 mm	40 mm

[a]EN 1999-1-1 6.1.6.3 (3)

5.5 Tensile Testing

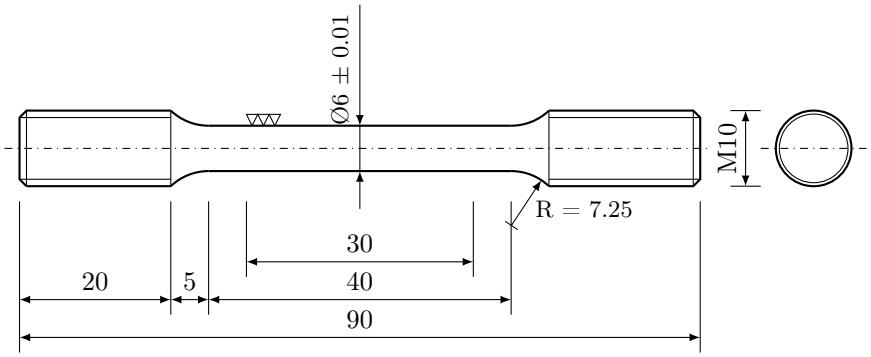

(a) Mechanical drawing of the tensile specimens. All dimensions in [mm]

(b) Tensile specimen

Figure 5.5: Tensile test specimen and geometry

Tensile tests were performed on specimens from the 10 mm and 30 mm plates by SINTEF Materials and Chemistry. From each plate 6 specimens were extracted. 3 in the extrusion direction (0°) and 3 in a perpendicular direction (90°). Figure 5.6 shows the plates and the extraction locations.

All the tests were performed in a Zwick Roell 30kN tensile tester at a rate of 1.2 mm/min. This corresponds to a strain-rate of 0.0005 s^{-1}. Force against diameter reduction of the specimen were measured. A laser, AEROEL XLS 13XY, measured the diameter continuously during the tests from two perpendicular positions. In this way, a non-circular neck could be detected. The specimens had also been polished one hundredth of a mm around the center of the gauge area. This made it trivial predicting where necking would start. To make sure the laser measured the smallest diameter, the operator swiped the specimen every 10-15 seconds to make sure the laser was positioned correctly. After testing, this swiping noise were removed from the results.

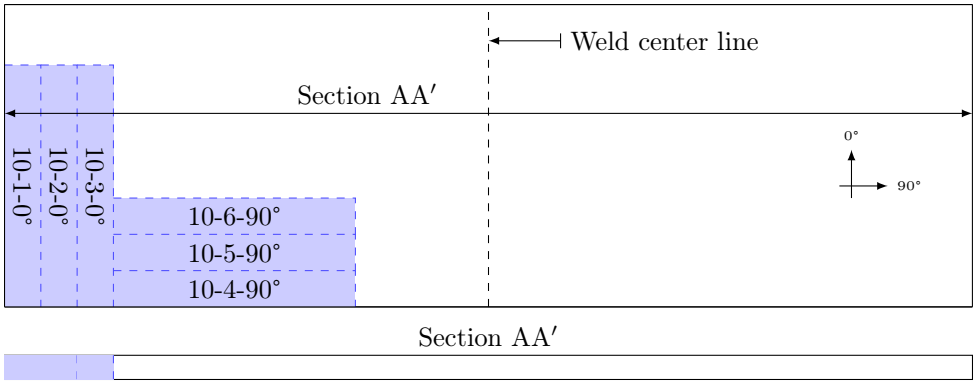

(a) 10 mm plate

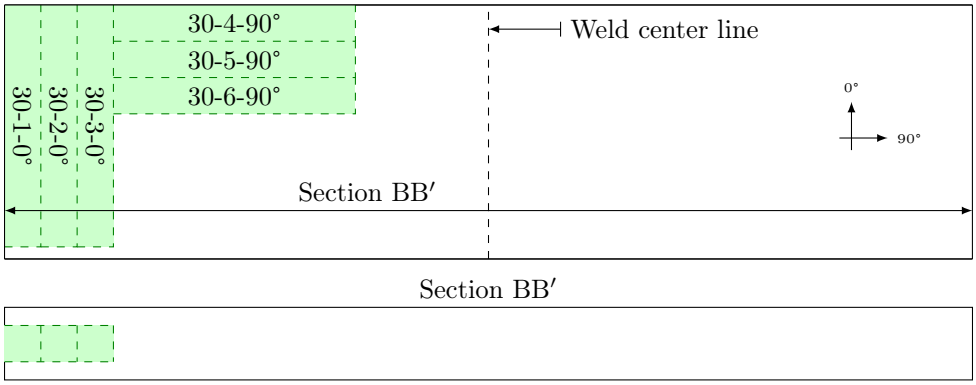

(b) 30 mm plate

Figure 5.6: Tensile specimen extraction from 10 mm and 30 mm plates. The cut out pieces are somewhat larger than the final tensile specimens, because of further processing needed in order to reach the final size shown in Figure 5.5.

5.5.1 Results from Tensile Testing

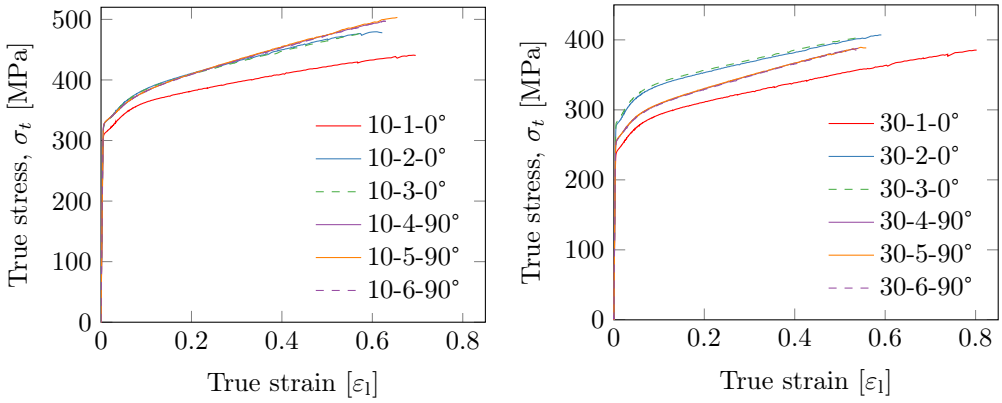

(a) Tensile tests 10 mm plate

(b) Tensile tests 30 mm plate

Figure 5.7: True stress true strain curves from tensile testing

Table 5.3: Raw data results from tensile testing

Plate [mm]	Test	Direction #	σ_0 [MPa]	σ_u [MPa]	ε_u	ε_f	W_c [MPa]
10	1[a]	0°	308.2	358.7	0.08392	0.696	274.9
10	2	0°	325.0	383.7	0.09445	0.625	263.6
10	3	0°	322.8	382.6	0.09405	0.586	243.9
10	4	90°	325.0	380.7	0.09715	0.632	269.4
10	5	90°	325.3	380.3	0.09680	0.655	283.3
10	6	90°	325.0	380.0	0.09550	0.630	268.4
30	1[a]	0°	237.5	290.8	0.09190	0.805	267.4
30	2	0°	277.2	329.7	0.07999	0.594	213.5
30	3	0°	280.8	332.7	0.07850	0.544	195.9
30	4	90°	253.4	305.1	0.08910	0.538	180.4
30	5	90°	254.1	306.2	0.09060	0.556	189.1
30	6	90°	253.1	304.5	0.08930	0.561	181.9

[a]Results omitted

Initial results are given in Table 5.3 and Figure 5.7. Two of the tests were different from the rest. A comparison between Table 5.3 and Figure 5.6a and 5.6b reveals that both of these tests came from the outer most part of the extruded plates. Assuming this is the reason for the deviation, these results have been omitted from this study.

The 10 mm plate showed little or no variation between the tests independent of direction, while the 30 mm plate showed more signs of anisotropy. Here the specimens extracted perpendicular to the extrusion direction show somewhat lower yield strength than the other specimens.

The rate of hardening seems to be almost equal in all the tests.

(a) 10-1-0°

(b) 10-2-0°

(c) 10-3-0°

(d) 10-4-90°

(e) 10-5-90°

(f) 10-6-90°

Figure 5.8: Tensile tests from the 10 mm plate

(a) 30-1-0°

(b) 30-2-0°

(c) 30-3-0°

(d) 30-4-90°

(e) 30-5-90°

(f) 30-6-90°

Figure 5.9: Tensile tests from the 30 mm plate

The curves in Figure 5.7 were calculated using formulas described in Section 2.2.1. The raw data from the tests consisted of force and diameter reduction. The data for Test 10-2-0° and 30-2-0° are displayed in Figure 5.10. In order to calculate stresses and strains, an average diameter reduction measure were used. This average can also be seen in Figure 5.10 as a dashed line. Similar plots for all the tensile tests can be found in Appendix B.

Figure 5.11 shows the true stress as a function of the logarithmic strain for Specimen 10-2-0° and 30-2-0°. These test results have been chosen to calibrate material models for use in numerical simulations. The calibration is described in Chapter 6.

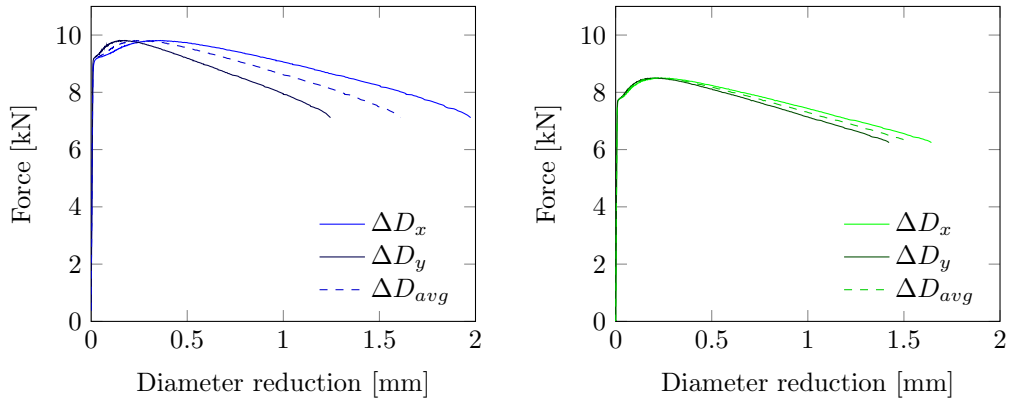

(a) Specimen 10-2-0° **(b)** Specimen 30-2-0°

Figure 5.10: Force against diameter reduction from two of the tensile tests

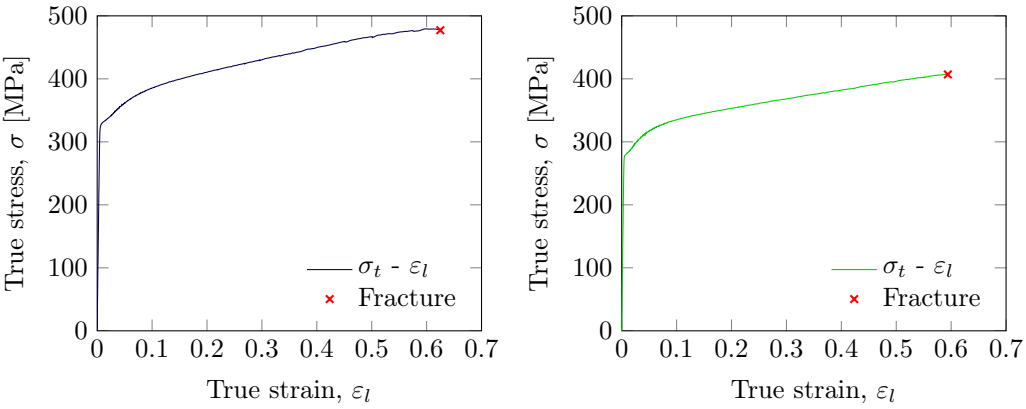

(a) Specimen 10-2-0° **(b)** Specimen 30-2-0°

Figure 5.11: Stress - strain data from two of the tensile tests

CHAPTER 6

Material Modelling

Direct calibration of data from tensile tests 10-2-0° and 30-2-0° has been performed. As seen in Section 5.5, the test results for the 10 mm plate were very similar, therefore it is assumed sufficient calibrating a material model from only one tensile test. As for the 30 mm plate, there were some anisotropy. However, making a complete material model for the 30 mm plate was outside the scope of this thesis. Though there are some anisotropy, only one test specimen has been chosen for direct calibration. Both test specimen chosen were from the extrusion directin of the plates.

The validity of the material model has been checked and recalibrated by inverse modelling of the tensile test in IMPETUS Afea Solver. Finally the true stress-true strain curve from inverse modelling has been compared with a similar curve from experimental tensile testing. This will give an indication whether the recalibrated material models can be used further in the study.

6.1 Direct Calibration

From the tensile tests, true stress-true strain curves were extracted (see Figure 5.11). These curves are only valid until the tensile specimen develops local necking. After this point, the results have to be adjusted. At necking the stresses are no longer uniaxial. The triaxial stress state that develops makes the true stress data from the tensile tests artificially high. The hydrostatic stress component needs to be removed. This can be done by using the Bridgman correction [35], given by:

$$\sigma_{eq} = \frac{\sigma_t}{(1 + \frac{2R_B}{a_B}) \ln(1 + \frac{a_B}{2R_B})} \tag{6.1}$$

where σ_{eq} is the equivalent stress. Figure 6.1 describes the parameters a_B and R_B and how the correction affects the true stress-true strain curve.

R_B and a_B were not measured during or after the tensile testing. Instead the fraction $\frac{a_B}{R_B}$ were calculated using an equation proposed by Le Roy et. al [35]:

$$\frac{a_B}{R_B} = 1.1(\varepsilon_l^p - \varepsilon_{lu}^p), \quad \varepsilon_l^p > \varepsilon_{lu}^p \tag{6.2}$$

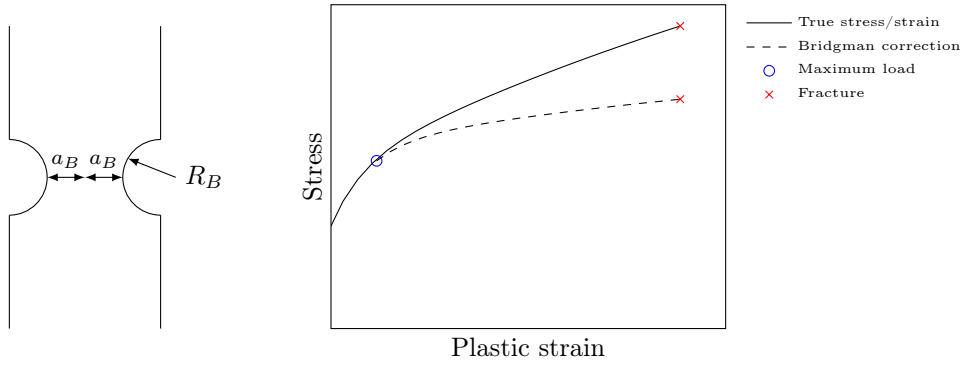

Figure 6.1: Bridgman input parameters and Bridgman correction showed graphically

where ε_{lu}^p is the equivalent strain at necking and ε_l^p is the true plastic strain.

The Bridgman correction starts at necking, σ_u. There are two common ways of finding σ_u; one graphical and one theoretical. The graphical method is simply zooming into the engineering stress-engineering strain curve and finding an approximate maximum value. The theoretical method is finding at which level of strain equation 6.3 is satisfied:

$$\frac{d\sigma_t}{d\varepsilon_l} = \sigma_t \tag{6.3}$$

6.1.1 Results From Direct Calibration

Differentiation of an initial curve fit of the raw data, gave almost exactly the same result as the graphical approach, when finding σ_u. The graphical values were chosen as a starting point for the Bridgman correction. Table 6.1 and Figure 6.2 show the results.

Table 6.1: Voce parameters from direct calibration

	A [MPa]	Q1 [MPa]	C1	Q2 [MPa]	C2	ε_{lu}^p	MSE [MPa]
Test 10-2-0°							
Initial[a]	325.0	48.62	17.6	312.5	0.70	0.0889	1.80
Bridgman corrected	325.0	65.07	15.8	84.3	0.93	0.0889	2.79
Test 30-2-0°							
Initial[a]	277.2	404.0	0.39	48.2	14.0	0.0753	1.75
Bridgman corrected	277.2	56.4	22.5	61.8	0.97	0.0753	2.44

[a]Voce-curvefit of the raw experimental data from yield to fracture

The curve fitting has been done using the Solver function in Microsoft Excel. It utilizes the least squares method to minimize the error between a Voce curve and experimental data. The error is listed in the results table as MSE, Mean square error.

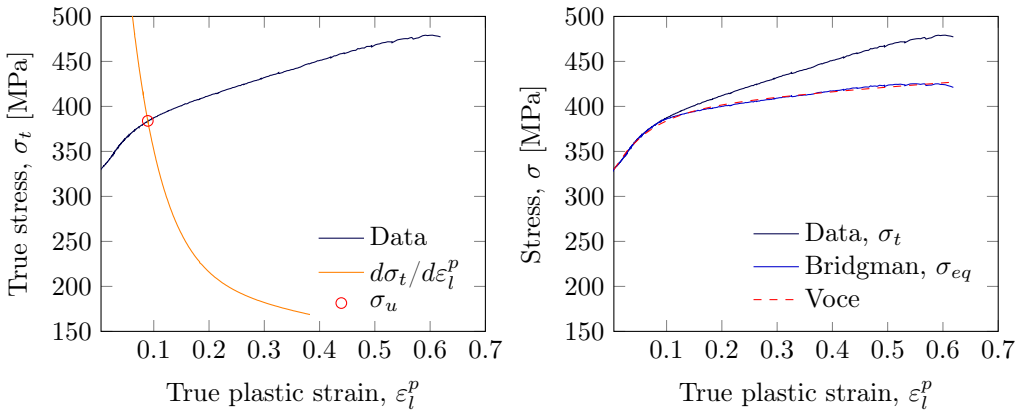

(a) Locating σ_u from specimen 10-2-0°

(b) Bridgman correction of 10-2-0°

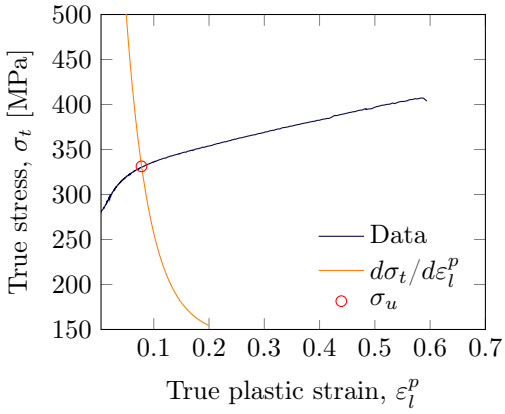

(c) Locating σ_u from specimen 30-2-0°

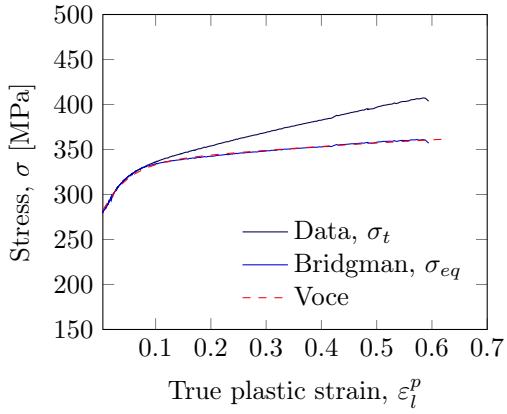

(d) Bridgman correction of 30-2-0°

Figure 6.2: Direct calibration of tensile specimen 10-2-0° and 30-2-0°

6.2 Inverse Modelling

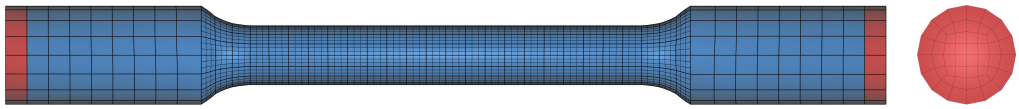

Figure 6.3: Tensile specimen modelled in IMPETUS Afea

To validate the curve fitting done, a tensile specimen was modelled in IMPETUS Afea Solver, see Figure 6.3. The specimen was modelled with 64-node quadratic hexahedron elements in the gauge area, and regular 8-node linear hexahedron elements in the rest of the model. Both of the parts marked with red in Figure 6.3 are modelled as rigid, and while one is set in motion, the other is held in place. Since IMPETUS Afea uses an explicit solver algorithm, and the critical time step in the model is about $5{\times}10^{-8}$ s, the simulation had to be time scaled. Therefore, the simulations were run at a speed of 25 mm/s, i.e. 1250 times the speed of the actual tensile tests. 25 mm/s corresponds to a strain rate of 37.5 s^{-1}. Rate dependency is disregarded in the IMPETUS Afea simulations.

The element size was chosen to be approximately the same as for the upcoming ballistic simulations (around 1-2 mm^3). Figure 6.4 shows the cross section of the gauge area. Here the smallest elements are about $2 \times 0.7 \times 0.7$ mm^3. Each element is divided into smaller parts using the 64-node quadratic hexahedron element formulation in IMPETUS Afea. The element outlines can be seen as slightly thicker than the rest.

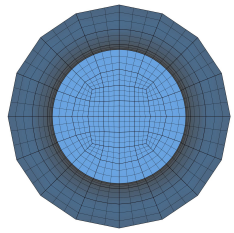

Figure 6.4: Cross section of the tensile specimens gauge area in IMPETUS Afea

The initial model was calibrated with the Voce-results obtained from direct calibration, and material constants from literature (see Table 8.1 page 71). The Voce parameters from the direct calibration were then altered in a series of simulations. In total 30 and 15 tensile tests were performed to obtain the final results for the 10 and 30 mm plates respectively. Direct calibration parameters from 10-2-0° gave a similar curve with an off-set at about 0.5 kN. As for the direct calibration parameters from 30-2-0°, the resulting curve overestimated the strength initially and underestimated it at a diameter reductions of more than 1 mm.

The directly calibrated models were not far from the experimental values, but still a number of simulations were needed for a satisfying fit. The Voce parameters governs the model with two Q values that gives the final saturation level, and two C values that govern how fast each Q value reaches its value. Tweaking these parameters manually took more effort than first anticipated. The results are given in Table 6.2 and Figure 6.5.

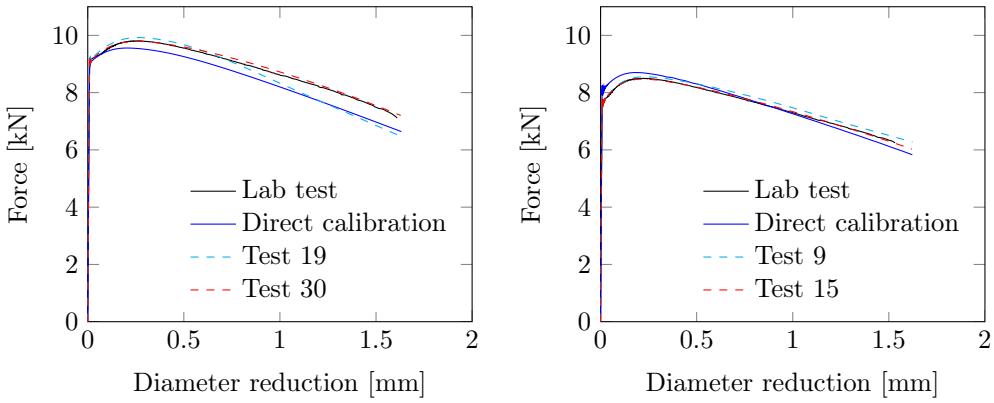

(a) Specimen 10-2-0° **(b)** Specimen 30-2-0°

Figure 6.5: Comparison of force versus diameter reduction from physical tests and numerical simulations

The red dashed lines in Figure 6.5, represent the final results given in Table 6.2. Hereafter, the material model for the base material of the 10 mm and the 20 mm plates will be denoted 10-2-0°, while the material model for the base material in the 30 mm plate will be denoted 30-2-0°.

The yield strength, σ_0, had to be lowered 2.5% for 10-2-0° and 4.5% for 30-2-0°. σ_0 from tensile testing results is the stress at 0.2% plastic strain, also known as $\sigma_{0.2}$. Taking this into account, it is only natural that the yield stress value had to be reduced a small amount.

Table 6.2: Voce parameters from inverse modelling

Specimen	A [MPa]	Q1 [MPa]	C1	Q2 [MPa]	C2
10-2-0°	317.0	55.0	17.0	165.0	1.6
30-2-0°	265.0	55.0	25.0	85.0	2.0

Using the equations given in Section 2.2.1, the force versus diameter reduction data from IMPETUS Afea can be converted into true stress-true strain curves. Running the Bridgman correction on these curves give results comparable with similar curves from direct calibration. The resulting curves in Figure 6.6, shows little or no difference. This supports the validity of the calibrated material models.

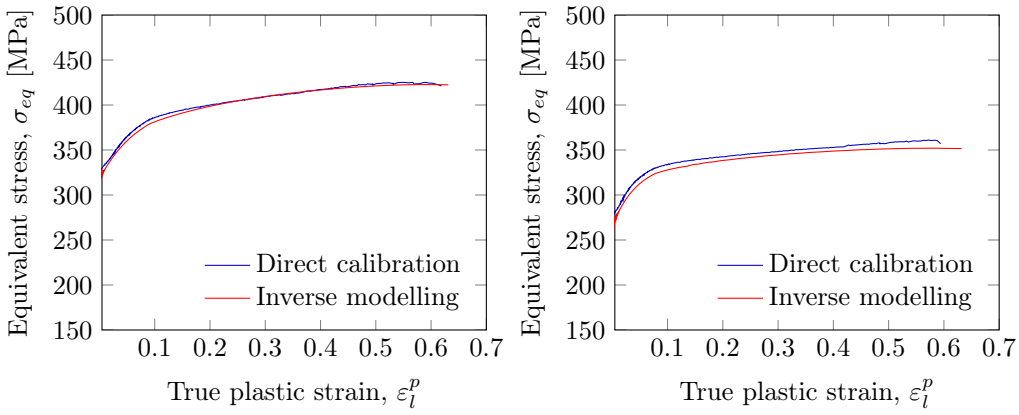

(a) Material model 10-2-0°

(b) Material model 30-2-0°

Figure 6.6: Comparison of Bridgman corrected true stress-true strain curves from inverse modelling and direct calibration.

6.3 HAZ Model for 10 mm Plate

No tensile testing has been performed across the weld and HAZ. Therefore, material models for these parts had to be approximated. This was done by combining the material model for the base material with the hardness measurements done across the weld and HAZ. A simple conversion equation exist between Vickers Hardness and yield strength [36]:

$$HV = 0.33\sigma_0 + 16.0 \tag{6.4}$$

Equation 6.4 and Table 6.2 give a hardness value of HV 120.6 for tensile test 10-2-0°. Comparing this with Figure 5.1d, show that the result is not far off. The average hardness over the thickness in the base material for the 10 mm plate is HV 110. If the constant in Equation 6.4 is changed from 16 to 5.5, the results are comparable. Solving Equation 6.4 for σ_0 and altering the constant yields:

$$\sigma_0 = \frac{HV - 5.5}{0.33} \tag{6.5}$$

With this altered equation, the yield stress for every Vickers Hardness measurement can be extracted. Assuming the material hardens to the same saturation level independent of hardness [37], complete material models for each hardness measurement can be obtained using Equation 6.5 in combination with Equation 6.6.

$$\sum_{i=1}^{2} Q_i^{HAZ} = \sigma_u^{Base} - \sigma_0^{HAZ} \tag{6.6}$$

Q1 and Q2 are Voce parameters. The ratio of the Voce parameters has been kept the same as in the base material model, when calculating how much of the total Q goes into Q1 and Q2. The parameters C1 and C2 in the Voce expression have been kept constant (see 10-2-0° in Table 6.2). Results from the calculations are given in Table 6.3, while Figure 6.7, give the stress-strain curves through the weld, HAZ and base material. The positions have been chosen so that results can be directly compared with NaMo results given in Chapter 7.

Table 6.3: Approximated material models from hardness measurements

		DFCW[a]	0 mm	4 mm	6 mm	8 mm	10 mm	14 mm	Base
Plate									
10 mm	Hardness[b]	[HV]	73.8	74.4	72.7	65.9	79.9	97.3	110
	σ_0	[MPa]	207.0	208.8	203.6	183.0	225.5	278.2	317.0
	Q^{tot}	[MPa]	330.0	328.2	333.4	354.0	311.5	258.8	220.0
	Q1	[MPa]	82.5	82.1	83.3	88.5	77.9	64.7	55.0
	Q2	[MPa]	247.5	246.2	250.1	265.5	233.6	194.1	165.0
	σ_u	[MPa]	550.0	550.0	550.0	550.0	550.0	550.0	550.0

[a] Distance from center weld
[b] Average of top, middle and bottom hardness measurements

A plot of these new material models against the model obtained from inverse modelling of the base material is shown in Figure 6.7.

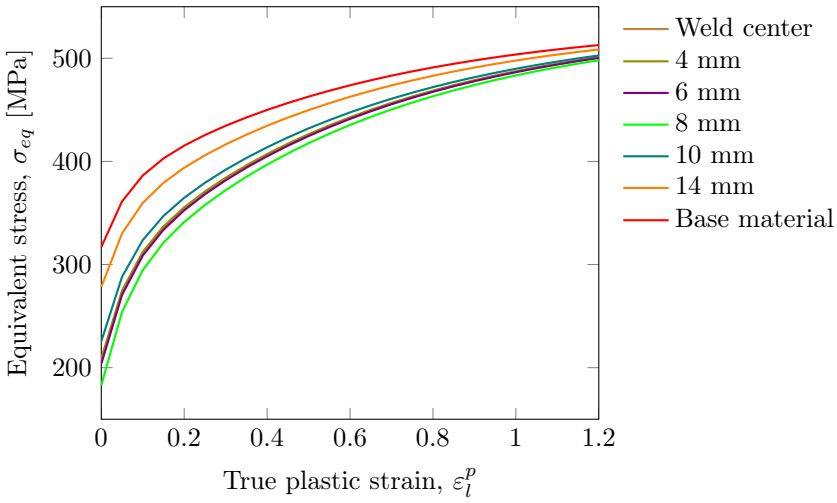

Figure 6.7: 10 mm plate material model calibration of HAZ from hardness measurements

6.4 HAZ Model For 30 mm Plate

For the 10 mm plate, vertical HAZ lines can be assumed. Hardness measurements confirm this assumption. For the 20 mm and 30 mm plates, a certain distance from the weld centerline, corresponds to different hardness values through the plate thickness. This is illustrated in figure 8.17. With that in mind, a field model of the 30 mm plate has been made. The details are found in Section 8.3. This model is equipped with material models for the HAZ material with hardness values of 60 HV and 75 HV. The base material has already been modelled from test 30-2-0°. Using the same approach as for the 10 mm plate, but with a constant of 1.5 in Equation 6.5, new material models have been calculated. The results are given in Table 6.4 and Figure 6.8.

Table 6.4: Approximated material models from hardness measurements

			Field[a]	1 & 3	2	4 (Base)
Plate						
30 mm	Hardness	[HV]		75	60	89
	σ_0	[MPa]		222.7	177.3	265.0
	Q^{tot}	[MPa]		182.3	227.7	140.0
	Q1	[MPa]		71.6	91.1	55.0
	Q2	[MPa]		110.7	136.6	85.0
	σ_u	[MPa]		405.0	405.0	405.0

[a]Fields explained in Section 8.3 page 82

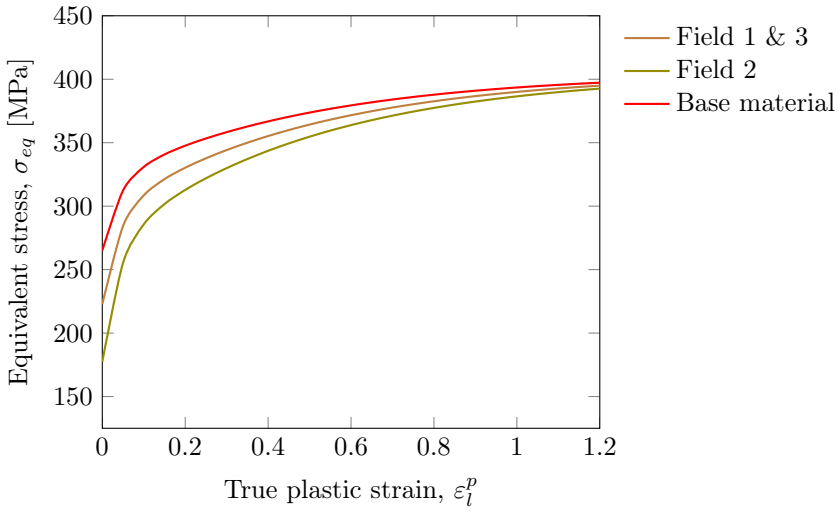

Figure 6.8: 30 mm plate material model calibration of HAZ from hardness measurements

CHAPTER 7

Numerical Material Modelling

7.1 Introduction

Although traditional laboratory testing of aluminium alloys still is the most common method of determining material parameters, there is an increased interest in doing this numerically. As illustrated in Figure 7.1, there are hundreds of combinations of welded age hardened aluminium alloys, with parameters ranging from choice of alloying elements, ageing procedures, welding procedures and post weld heat treatments [38]. This makes laboratory testing cumbersome and expensive.

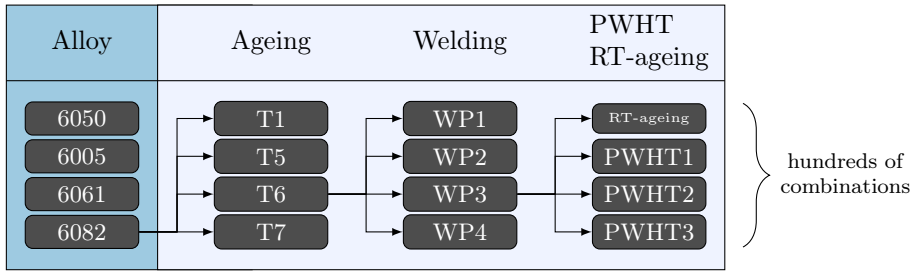

Figure 7.1: Variables involved in the production of welded age hardened aluminium alloys [38]

In this study, we will use a three-stage model as illustrated in Figure 7.2. First stage includes a thermal model to predict the heat flow from welding. Second stage involves a microstructure based constitutive model using the chemical composition and the input from the thermal model as input to give stress-strain curves. Finally, the output from the microstructure based model will be used as input in a mechanical model to simulate ballistic experiments.

In the first stage of the model, the finite element software Weldsim developed by The Institute for Energy Technology, IFE, and Hydro has been used. For the second stage, the microstructure based software NaMo, developed by Dr. Ole Runar Myhr at Hydro, has been used. Stage three was be performed in IMPETUS Afea by the authors. If this model gave good results, the ballistic experiments performed in Chapter 4, could be simulated without doing any material testing.

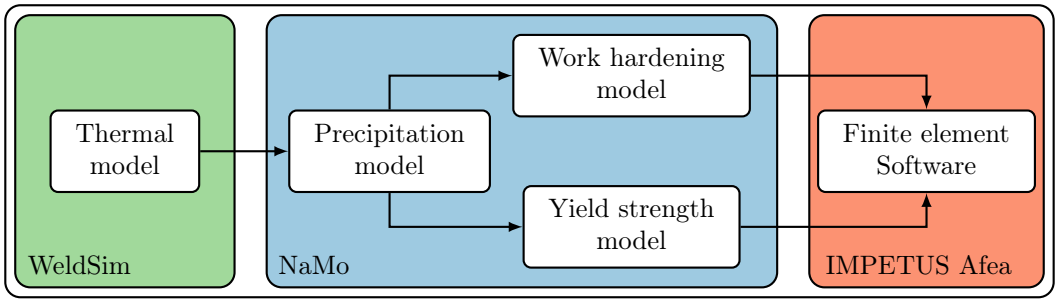

Figure 7.2: Steps involved in the numerical simulations

7.2 Weldsim

Weldsim is a finite element code for welding developed by IFE and Hydro. It uses finite element formulation of heat transfer to model the thermal flow from the fusion line and outwards in the base material. Figure 7.3 shows an example of a multipass welding simulation in Weldsim. Here it is seen how the heat propagates through the material with time. From these simulations, the operator can collect temperature data from selected points in the material and in time. This can later be used as input in NaMo [39, 40].

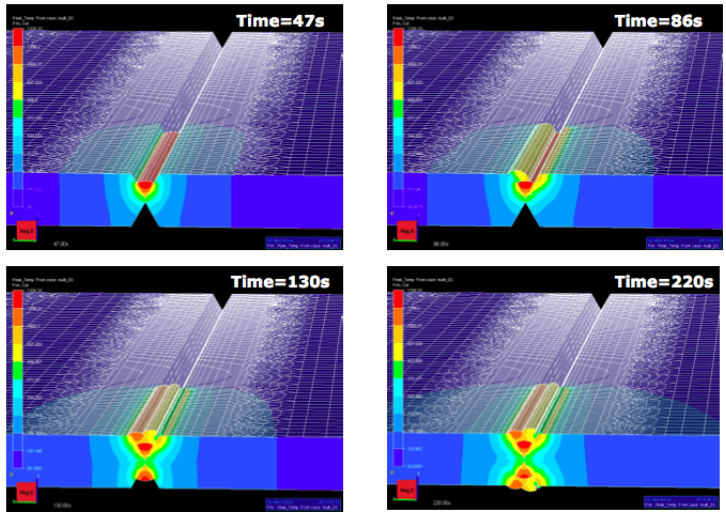

Figure 7.3: Fusion welding simulation of two 15 mm EN AW-6082 T6 plates in Weldsim [39]

IFE has carried out thermal simulations for the 10 mm EN AW-6082 T6 plate, and the resulting thermal cycles for the two first passes are shown in Figure 7.4. Here, the four continuous curves represents the temperature with time, at 8.1 mm, 10.1 mm, 12.1 mm and 14.1 mm, while the piecewise linear curve is constructed to be used in the NaMo simulations. There were three welding strings in total, but string number three did not reach temperatures that would have altered the material properties. Therefore only the two first strings have been simulated.

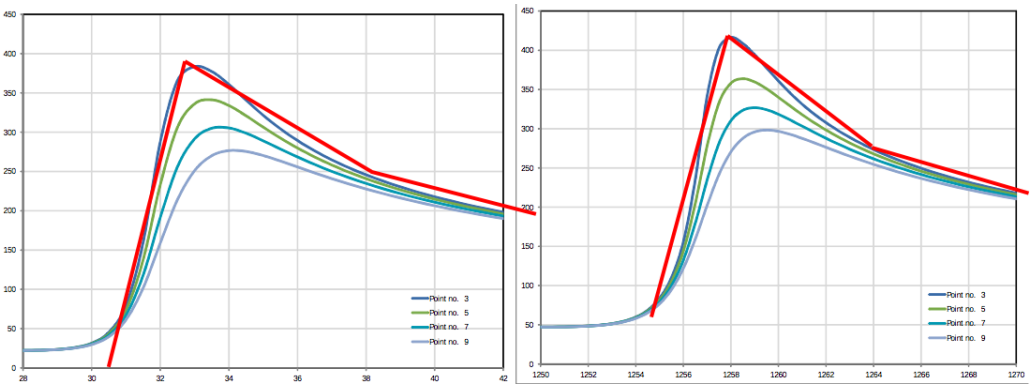

Figure 7.4: Thermal cycles calculated by IFE with Weldsim for 10 mm plates

From the time scale it can be seen that after the first welding pass, the material was cooled down to a about 50°C, before starting the second pass at about 1250 seconds.

7.3 NaMo

NaMo stands for Nano Structure Model. It has been developed by Dr. Ole Runar Myhr at Hydro, aiming to find the material characteristics for different types of alloys, without having to manufacture and carry out laboratory tests. The goal is to calculate the stress-strain curve for a given alloy, only given the material composition and a thermal history. The NaMo simulations in this thesis have been performed by Dr. Ole Runar Myhr.

In the following, a brief description of the theory behind the NaMo software will be examined, before presenting the results and a comparison with the laboratory data.

7.3.1 Precipitation Model

The theory behind the precipitation phase has previously been examined in Section 2.3.3. The first and most extensive part of the NaMo model is the precipitation model. As illustrated in Figure 7.2, it produces the input for both the yield strength and work hardening models. Figure 7.5 shows an illustration of the input used and the output produced by the precipitation model.

NaMo uses an alorithm including classic nucleation equations to calculate a particle size distribution. From the size distribution, the following variables can be extracted:

- The mean interaction force between dislocations and particles, $\overline{F}$
- The Friedel length, l (the mean spacing between precipitates)
- Mean solute concentrations in matrix of element i, $\overline{C_i}$
- Geometric slip distance, λ_g
- Volume fraction of Orowan particles, f_0 (non-shearable particles)

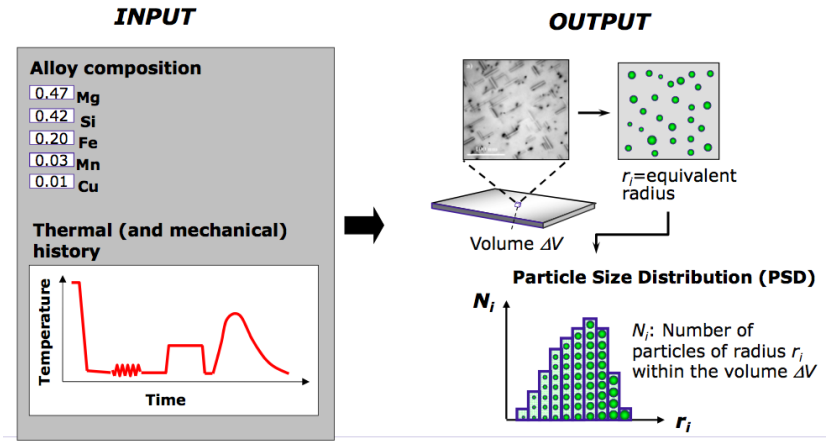

Figure 7.5: Input and output for the precipitation model i NaMo [39]

These are the variables that constitute the input for further calculation of yield stress and work hardening models [41].

To predict the complete stress-strain curve, the flow stress, σ_f, is needed and it can be calculated from Equation 7.1.

$$\sigma_f = \sigma_0 + \Delta\sigma_d \tag{7.1}$$

Here σ_0 is the yield strength and $\Delta\sigma_d$ is the net contribution from the dislocation hardening [41].

7.3.2 Yield Strength Model

As mentioned in the previous section, the yield strength model uses the output from the precipitation model to caluculate the yield strength. Figure 7.6 illustrates how a dislocation is obstructed by precipitates. If the radius of the particles is large enough, the dislocation has to bend around, instead of shearing it.

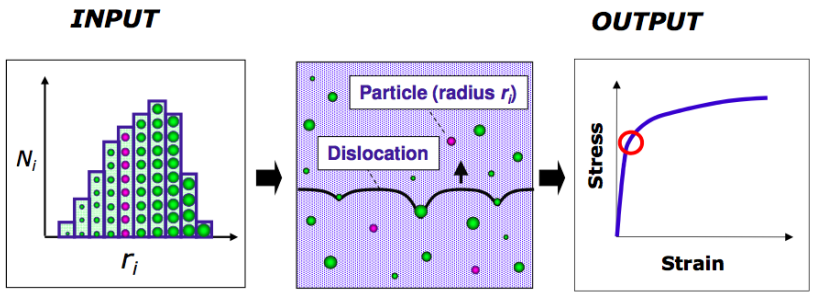

Figure 7.6: Input and output for the yield strength model in NaMo [39]

The yield strength of the alloy is calculated by Equation 7.2.

$$\sigma_y = \sigma_i + \sigma_p + \sigma_{ss} \tag{7.2}$$

where σ_i is the intrinsic yield strength of pure aluminium and σ_{ss} is the solid solution hardening potential of the alloy. σ_p is the precipitation hardening of the alloy, calculated using Equation 7.3:

$$\sigma_p = \frac{M\overline{F}}{bl} \tag{7.3}$$

where M is the Taylor factor and b is the magnitude of the Burgers vector. $\overline{F}$ and l are as previously mentioned obtained from the particle size distribution. For more theory behind the mechanisms of hardening, the reader is referred to Section 2.3.3.

7.3.3 Work Hardening Model

The goal of the work hardening model is to find $\Delta\sigma_d$. Myhr et al. [42] presents the following equation:

$$\Delta\sigma_d = \sigma - \sigma_y = \alpha MGb\sqrt{\rho_t} = \alpha MGb\sqrt{\rho_s + \rho_g} \tag{7.4}$$

where α is a constant with a numerical value close to 0.3 and G is the shear modulus. The variable,ρ_t, the total dislocation density, is found by adding the geometrically necessary dislocations, ρ_g and the statistically stored dislocations, ρ_s. These inputs are extracted from the particle size distribution produced by the precipitation model.

7.3.4 Comparison of NaMo Results With Laboratory Data

Figure 7.7 shows the stress-strain curves for the 10 mm plate generated by NaMo, compared to the stress-strain curve from the inverse modelling of tensile specimen 10-2-0°. It is seen that the NaMo generated curve coincide well with the tensile test curve, except for the stage IV hardening. The current version of NaMo does not yet account for this.

Figure 7.8 shows the NaMo generated hardness curves through the HAZ, compared with the top, middle and bottom hardness curves from the Vickers hardness tests. The results from NaMo seems to coincide well with the experimental values.

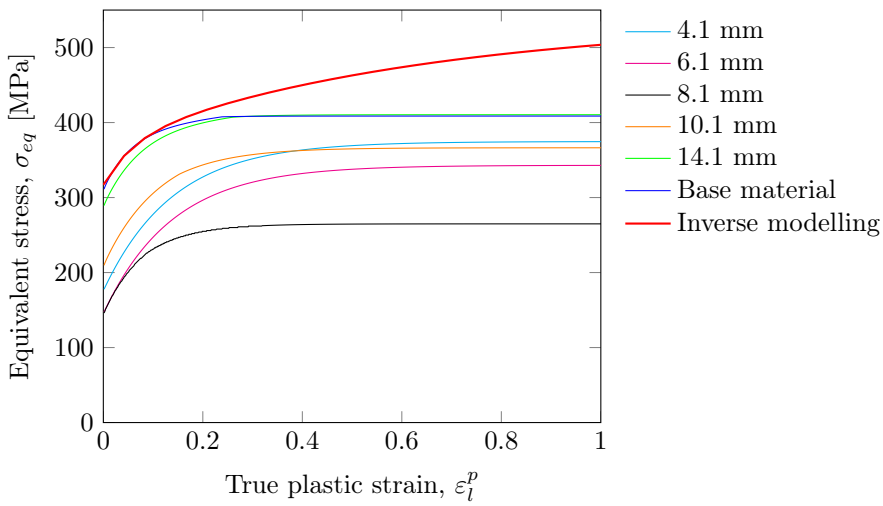

Figure 7.7: NaMo stress-strain results compared with inverse modelling of 10-2-0°

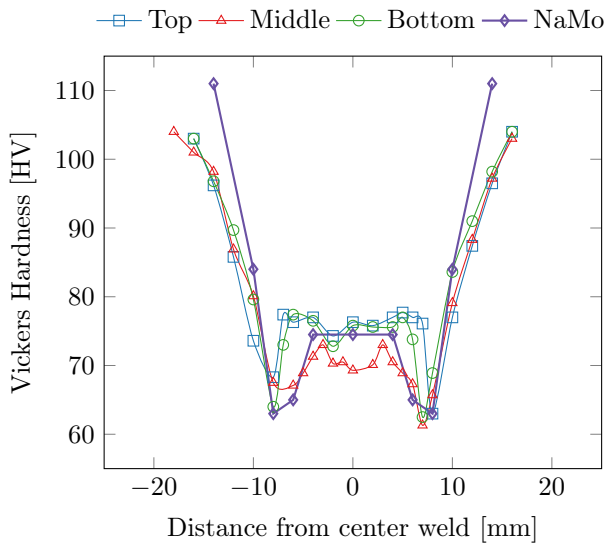

Figure 7.8: Hardness measurements from experiments and from NaMo for 10 mm plate

7.3.5 Calibration of Material Parameters

Figure 7.9 gives a Voce curve fit of the stress-strain curves generated by NaMo. Table 7.1 gives the Voce parameters from the curve fitting. Hereafter the NaMo material models will be denoted NaMo.

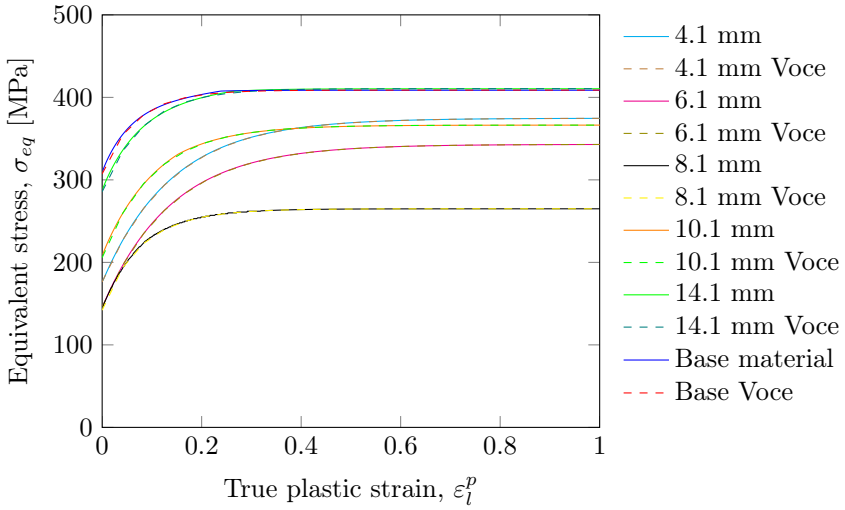

Figure 7.9: Voce curvefitting of NaMo results

Table 7.1: Results from curve fitting of NaMo data

DFCW[a] [mm]	A [MPa]	Q1 [MPa]	C1	Q2 [MPa]	C2	MSE [MPa]	Comment
4.1	176.3	141.1	7.16	57.3	7.15	0.0140	At weld fusion line
6.1	146.0	139.2	7.20	57.9	7.21	0.0139	
8.1	142.1	19.7	23.26	103.2	11.66	0.0288	Middle of HAZ
10.1	205.8	69.5	11.54	91.1	8.66	0.0818	
14.1	285.6	115.2	12.20	9.80	12.21	0.2911	
Base	307.3	4.3	278.7	97.1	14.13	0.2254	Base material

[a]Distance from center weld

CHAPTER 8

Numerical Simulations

8.1 Preparations

The numerical simulations has been performed in IMPETUS Afea Solver. See Section 2.9.1 for more information.

IMPETUS Afea Solver needs a number of constants and equations as input. The Modified Johnson-Cook constitutive relation and the Cockcroft-Latham fracture criterion have been chosen as governing equations (see Section 2.7.2 and 2.7.3). The material constants common for all the numerical simulations performed in this thesis, are listed in Table 8.1. The hardening variables that vary between which material model being investigated, can be found in Chapter 6.

Table 8.1: Material constants used in IMPETUS Afea

	Elasic constants			Damage	Strain rate hardening	
Material	E [MPa]	ρ [kg/m^3]	ν	W_c [MPa]	$\dot{\varepsilon}_{0p}$ [1/s]	C
Aluminium[a]	70 000	2700	0.33	263.6 or 213.5[b]	5e-4	0.001
Steel core[c]	-	7850	-	-	-	-

	Thermal properties						
Material	T_m [K]	T_r [K]	λ [W/mK]	m	C_p [J/kgK]	χ	α [1/K]
Aluminium[a]	923	293	0	1.00	894	0.9	0

[a] Material parameters from literature [13, 32]
[b] Depending on material model used. See Table 5.3 page 49
[c] Modeled as rigid. Only ρ needed.

In addition, IMPETUS Afea needs an *Equation of state*, EOS. EOS describes the hydrostatic pressure in computer codes like IMPETUS Afea. According to Zukas et al. [43], a linear EOS can be used in ballistic simulations with velocities ranging from 0.5 - 2 km/s. The default EOS in IMPETUS Afea reads:

$$p = -K\varepsilon_v + K\alpha_T(T - T_0) \tag{8.1}$$

Where p is the pressure, K is the bulk modulus , ε_v is the volumetric strain, α_T is the heat expansion coefficient, T is the current temperature and T_0 is the reference temperature (usually room temperature).

α_T has been set to 0 for all the numerical simulations in this thesis. Holmen and Johnsen [28] have investigated the effect of α_T in similar simulations, and the results showed that the effect was negligible. This reduces Equation 8.1 to:

$$p = -K\varepsilon_v \tag{8.2}$$

Another important assumption made, as mentioned in Section 2.1, is adiabatic conditions during all the simulations. In IMPETUS Afea setting the heat conductivity, λ, to zero enforces this.

In the upcoming section, the initial model will be introduced and effects of different parametric changes investigated. The most reliable and physically explainable set of parameters are noted and used further in Section 8.5. A simulation is found reliable if the total energy is approximately constant. The total energy is the most important tool in explicit finite element analysis for validating results. If the total energy in a simulation varies more than 5-10%, it is generally a sign of numerical instability or non-physical behavior [1].

Instability due to rounding error is another non-physical aspect one should be aware of. If the number of iterations is too high, a small rounding error in each iteration can give big fluctuations in the final result. A rule of thumb for explicit finite element analysis say that if the number of iterations exceed 10^6, one should be attentive to this problem [1]. If any of the simulations done in this thesis get close to or exceed this level, this will be commented in the results. Initial testing reveals that the number of iterations generally is in the range of 10^5.

An overview of all the simulations can be found in Section 8.4.

An earlier study [28], suggest that results from IMPETUS Afea simulations like these do not vary much when modeling the whole projectile versus only the steel core. The whole projectile also consist of a brass jacket and a lead filling at the tip. The results is not very different considering that half of the mass is removed [28], and the computational cost is lowered. Therefore all the simulations in this thesis have been done only with the APM2 hard steel core. The hard steel core is also modelled as rigid, and this assumption is backed up by the experimental tests where the penetrated steel core usually showed no signs of damage.

8.2 Setting Up the Initial Model

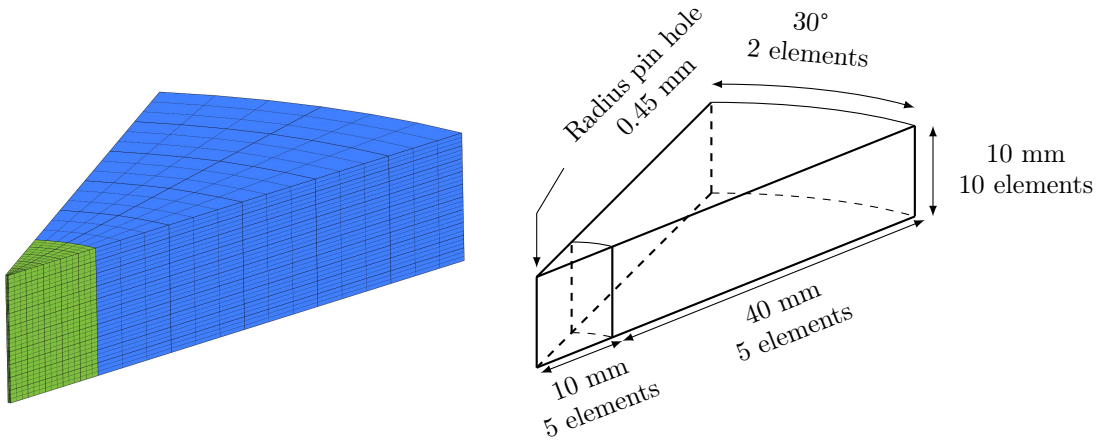

(a) Meshed initial model **(b)** Model dimensions and number of elements

Figure 8.1: Initial model used in IMPETUS Afea

The initial model has been fitted with the material model 10-2-0°, see Table 6.2.

An initial model for numerical ballistic simulation in IMPETUS Afea has been developed. The model contains 1/12 of a 10 mm plate and 1/12 of a APM2 steel core, and has two symmetry planes. This makes the model computationally friendly and easy to work with. Figure 8.1 shows the geometry and the mesh of the plate. The plate has a pin hole of radius 0.45 mm, which barely fits the tip of the modelled APM2 steel core. Dr. Lars Olovsson at IMPETUS Afea provided the geometries of the APM2 steel core, shown in Figure 8.2. The geometry of the plates were constructed by geometrical functions in IMPETUS Afea. The IMPETUS Afea input file for the initial model is provided in Appendix D.

IMPETUS Afea has three ways of defining an element as damaged. When damaged, three options follow of whether the element should be eroded, not eroded or split from the neighboring elements (fracture). If the element is eroded, IMPETUS Afea removes it completely from the simulation. An element can also be damaged without being eroded. With this option the element continue being a part of the simulation, but it can only withstand compressive stresses and not shear stresses. The node split option detaches an element from a neighboring element, but this has not been investigated in this thesis.

The three damage criteria are listed below:

1. Damage by dropping time step
   A time increment size limit can be set, and if the critical time step for an element drops below this level, the element is eroded. With this option only complete removal of the element is possible. In the initial model the limit is set to $t_{cr} = 7 \times 10^{-10}$ s.

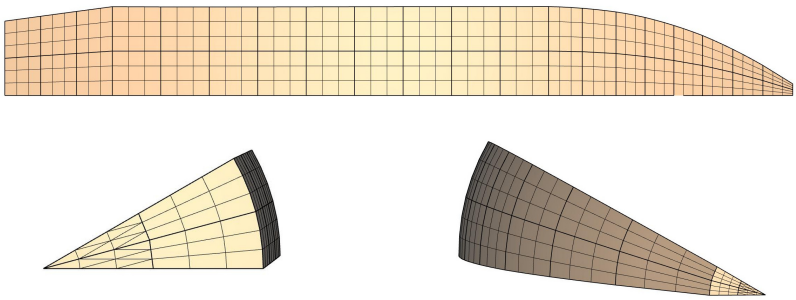

(a) APM2 steel core 1/12 model

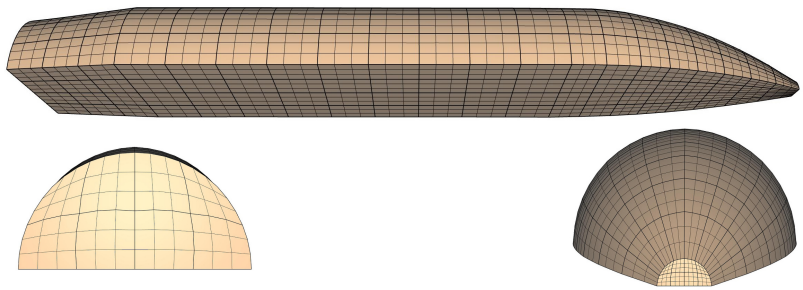

(b) APM2 steel core half model

Figure 8.2: The two meshes of the APM2 steel core used in this thesis, seen from the side, top and bottom.

2. Damage by Cockcroft-Latham damage criterion
   If the W_c number of an element is greater than a chosen value, the element is damaged. With this option all three element erosion options are available. The W_c number used in the initial model is 263.6 MPa, and with material model 30-2-0° a value of 213.5 MPa is used.
3. Damage by temperature
   If the element reaches T_m, it is not eroded, but can still take compressive stresses.

A set of initial velocities at 325, 350, 375 and 400 m/s have been selected. The velocities were chosen by examination of laboratory ballistic tests 1-4 of the 10 mm plate (see Chapter 4). The results from the initial simulations have been fitted with a Recht-Ipson expression with a = 1 and p = 2 (see Section 2.5). The fitting was done using a Matlab script given in Appendix E. The initial model results compared to experimental data, can be seen in Figure 8.3.

IMPETUS Afea utilises the penalty contact algorithm. In all simulations, the penalty factor has been set to -1×10^{15}, which means that 0.001 mm penetration gives 1 GPa of contact pressure in the opposite direction.

Results from the initial model are somewhat conservative. To make sure the initial model can be used further on in this study, the effects of some important parameters have been

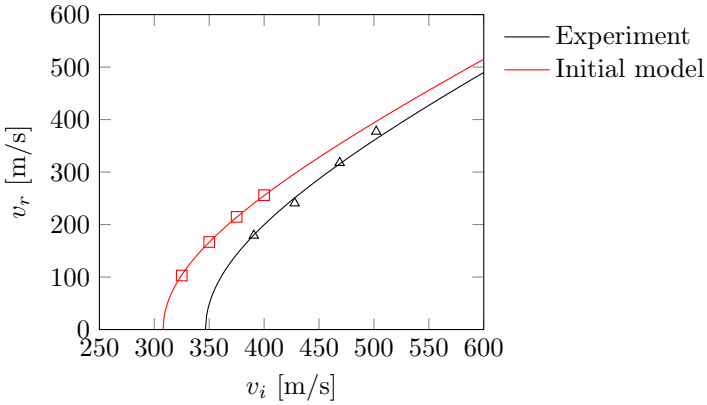

Figure 8.3: Initial model results compared to experimental values

investigated in the following sections.

8.2.1 Friction

Friction, μ, has been set to zero in the initial model. Earlier studies show that in some ballistic experiments the friction can be neglected [4]. Some believe that, as the projectile penetrates the target at high velocities, the material in contact with the projectile melts, and no friction occurs [4]. If a non-conical projectile perforates a plate, it often ejects a plug with a larger diameter than the projectile itself. This would also give approximately no friction. However, since the APM2 bullet is an ogival projectile and therefore is in contact with the walls of the cavity, a more realistic frictional coefficient of 0.05 has been proposed [4]. Figure 8.4 shows that $\mu = 0.05$ gives excellent results in this study, with the curve laying on top of the experimental curve. $\mu = 0.05$ will therefore be chosen as the frictional coefficient for the ballistic simulation in Section 8.5.

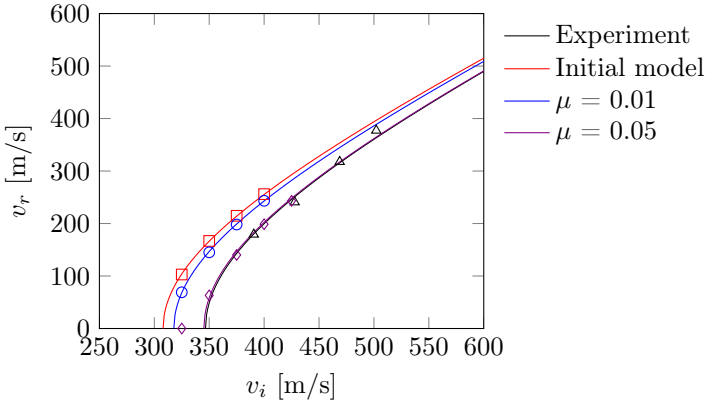

Figure 8.4: Friction study of the base material from the 10 mm plate

Figure 8.5 illustrate the energy balance for two different ballistic simulations at $v_i = 325$ m/s. One test with no friction and one with $\mu = 0.05$. The kinetic energy of the energy graph to the right drops to zero, as the projectile stopped. The frictional energy is non

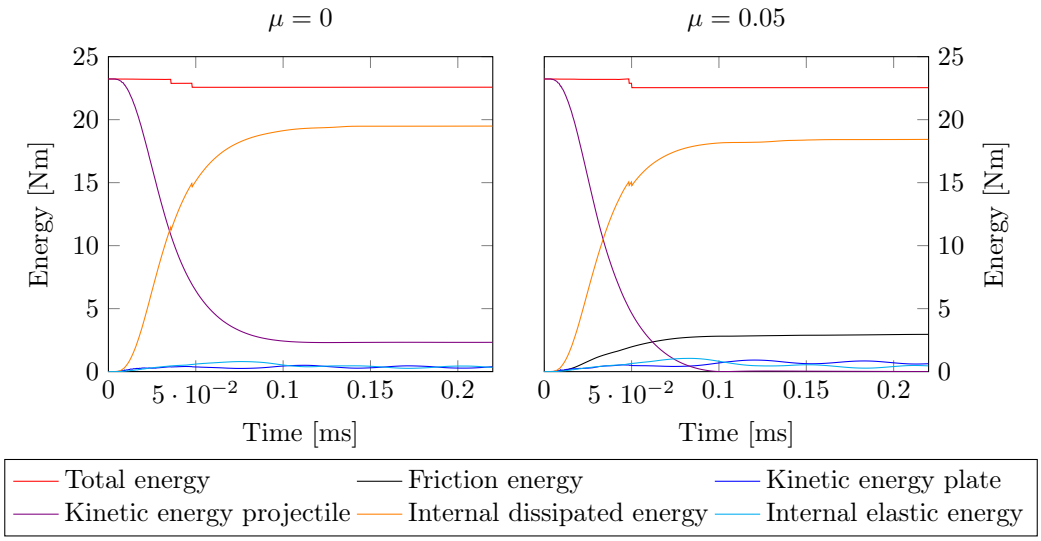

Figure 8.5: Energy balance with $v_i = 325$ m/s

existent in the left graph and fairly large in the right. This strengthens the validity of the simulations. The total energy should be a constant, but it has a dent in it. At this time two elements erode due to t_{cr} dropping below the set limit at $7{\times}10^{-10}$. Which is very small. The model is still well inside of the 5-10% limit, discussed in Section 8.1. Most of the kinetic energy is transformed into internal energy through plastic dissipation. In the model containing friction, less energy is converted into internal energy and more into frictional energy, as expected.

8.2.2 Boundary conditions

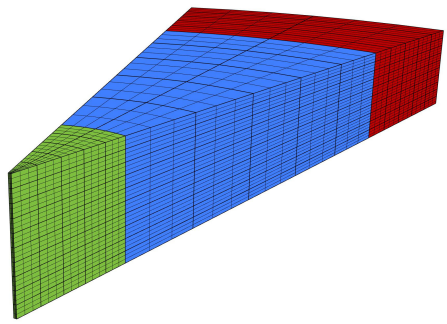

Figure 8.6: Clamped 1/12 model in IMPETUS Afea

The effects of a clamped plate have been investigated. The initial model was extended with a 20 mm wide rigid section at the end (see Figure 8.6), and then the simulations

were re-run. As Figure 8.7 shows, the results are exactly the same. Therefore boundary conditions will not be used further in this study.

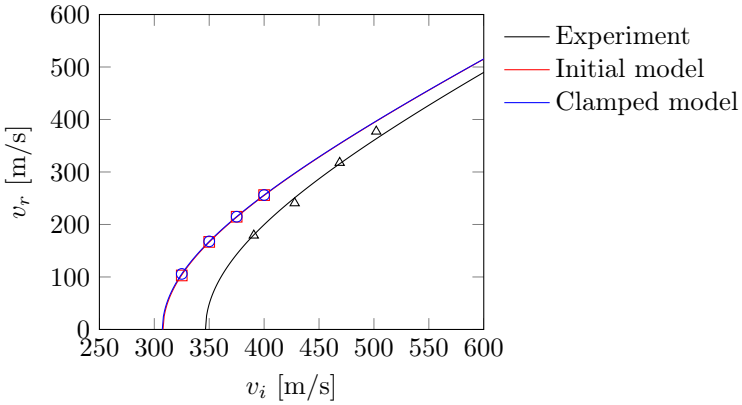

Figure 8.7: Boundary condition study with a clamped initial model

8.2.3 Symmetry

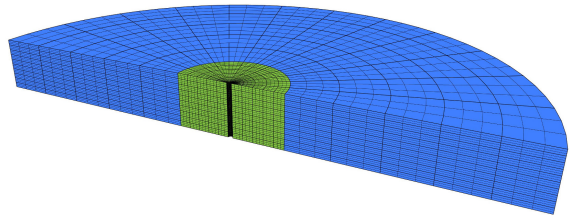

Figure 8.8: Half model

When modeling 1/12 of the real experiment, computational costs are lowered substantially. Figure 8.8 shows a half model with the same geometry that has been tested, showing the exact same results as the 1/12 model. Figure 8.9 shows the Recht-Ipson curves. This leads to a conclusion that IMPETUS Afea handles two symmetry planes equally good as one symmetry plane.

8.2.4 Mesh Sensitivity

Figure 8.10 shows two different mesh densities that have been tested. The results in Figure 8.11 show that mesh refinement makes the model more conservative. This is as expected from finite element theory [2]. The difference in computational cost is limited, and therefore the mesh from the initial model will be kept as is for the ballistic simulations in Section 8.5.

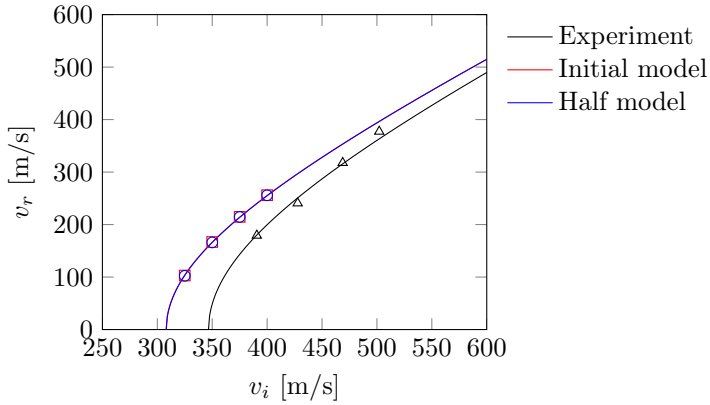

Figure 8.9: Symmetry study of the base model

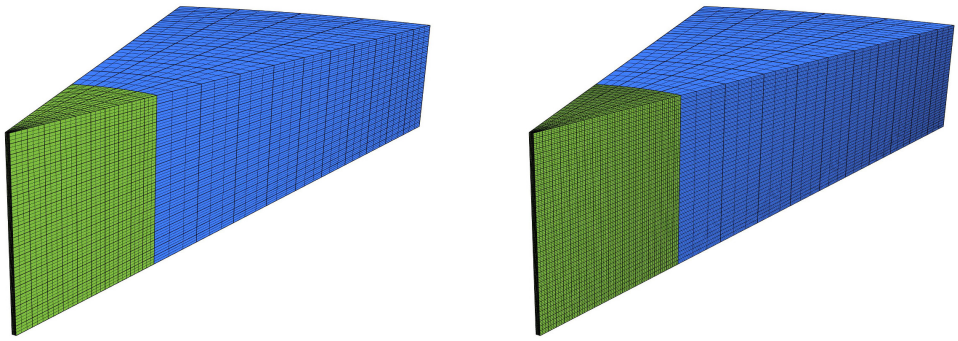

(a) Fine mesh 2x, coarse mesh 2x

(b) Fine mesh 4x, coarse mesh 2x

Figure 8.10: Mesh from initial model refined by different factors

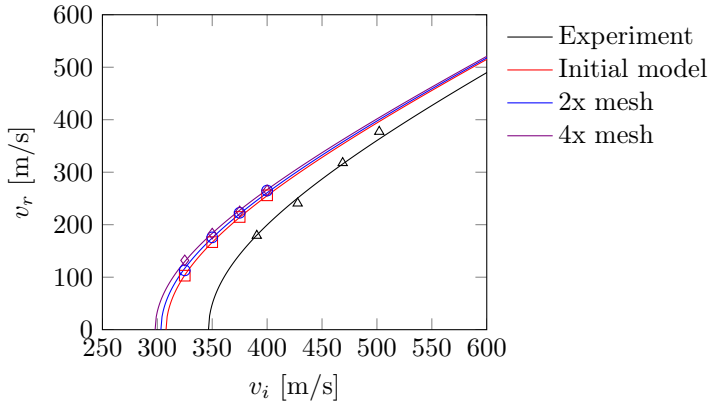

Figure 8.11: Mesh sensitivity study of the base material from the 10 mm plate

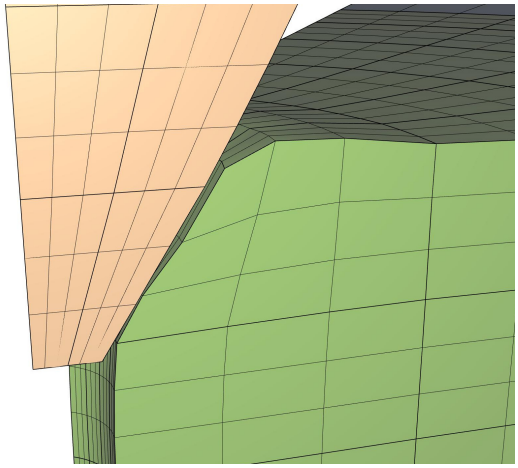

Figure 8.12: Close up detail of the projectile as it hits the plate and the pin hole

8.2.5 Pin Hole

Figure 8.12 shows the APM2 steel core entering the pin hole of the 1/12 model. As Figure 8.13 shows, the plate modeled with no pin hole and with element erosion is more conservative than the plate modeled with a pin hole. When elements are completely removed from the simulation, instead of just removing their shear stress resistance, the projectile will perforate more easily. There will be a lot less resistance when no elements have to be pushed aside. In the initial model a pin hole with a radius of 0.45 mm has been made. The steel core has a maximum radius of 3 mm and the hole needed for perforation has 2.2% less material when the pin hole is present. This minor difference makes up for other numerical problems like time step erosion. With no pin hole present, some elements have to be removed to make a hole in the plate. This is discussed further in the setup and results of the 30 mm field model, where no pin hole and time step erosion have been used.

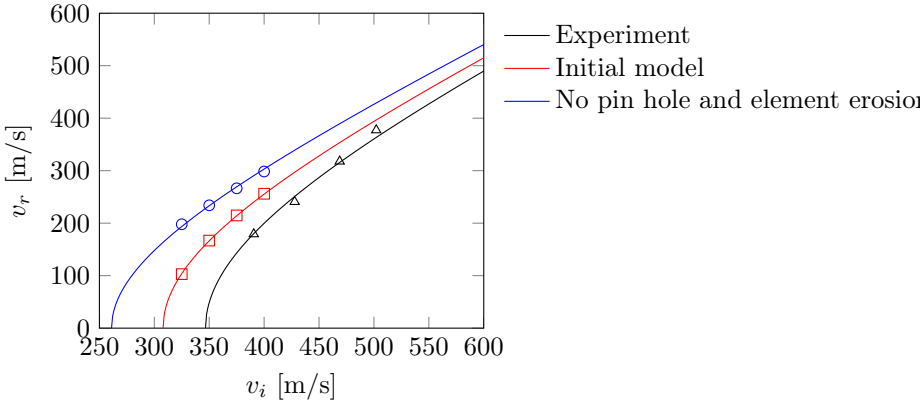

Figure 8.13: Pin hole study

8.2.6 Number of Simulations

Some extra simulations have been performed on the plate to investigate whether or not four simulations are sufficient to produce a satisfying Recht-Ipson curve. As Figure 8.14 shows, the curve with four simulations and the curve with eight simulations overlap. This indicates that four simulations are sufficient.

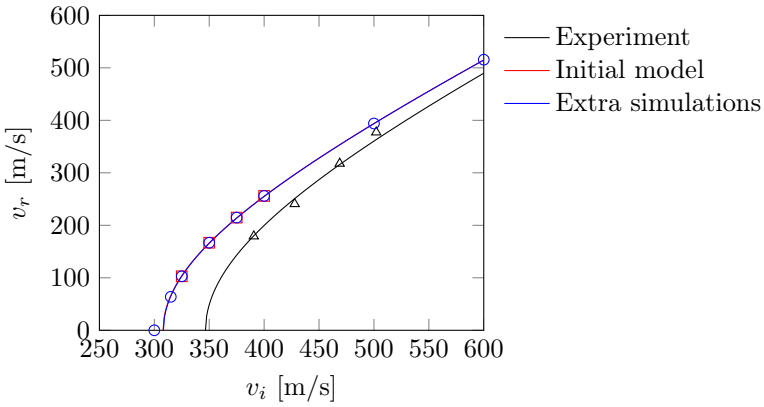

Figure 8.14: Number of ballistic simulations to make a good Recht-Ipson curve

8.2.7 Time Step Size

As previously mentioned, the critical time step size for element erosion was set to $7{\times}10^{-10}$ s in the initial model. A study has been done to check the influence of a larger critical time step limit in order to reduce computational cost. As Figure 8.15 shows, larger time steps did not affect the results.

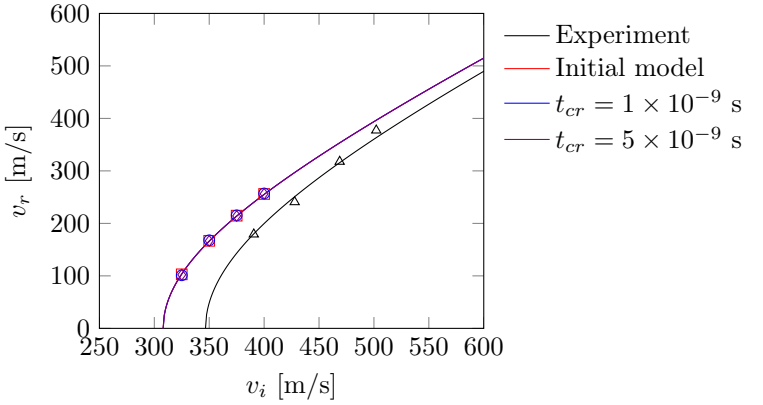

Figure 8.15: Time step erosion study

8.2.8 Updated Initial Model

The parameter study of the preceding sections has validated that the initial model can describe these simulations in a satisfying way. In the friction study the results were improved by setting $\mu = 0.05$. Therefore the updated initial model will be fitted with this value. As the increased time step did not affect the results, a time step of $t_{cr} = 1 \times 10^{-9}$ s will be used.

This updated model has been used in all the ballistic simulations that involve *one* material model.

8.3 Constructing a Field Model

For all simulations of the 10 mm plate and the base material simulations of the 20 mm and 30 mm plates, a uniform material model through the thickness have been used. Even for the HAZ models of the 10 mm plate this is a good assumption. Figure 5.1 on page 43 shows that the HAZ regions for the 10 mm plate are almost vertical. This is not the case for the 20 mm and 30 mm plates, where the hardness varies in two directions. IMPETUS Afea has a Johnson-Cook strength model with a field function [23], but this only allows material properties to vary in one direction. As this would not be enough, a custom mesh has been developed.

The 30 mm plate has been chosen as a testing model. The testing model consist of a $80\times50\times30$ mm^3 plate with $1\times1\times1$ mm^3 elements. This is half the model, so one symmetry plane has been used. Figure 8.16 shows the mesh with the projectile before impact. Here we see that the model is divided into four fields (one hidden). These fields, their geometry and their averaged hardness are shown in Figure 8.17. Each field has material parameters taken from Table 6.4 on page 60. Figure 8.16 shows the field model used in IMPETUS Afea. The red field in the figure has the lowest hardness with a value of 60 HV.

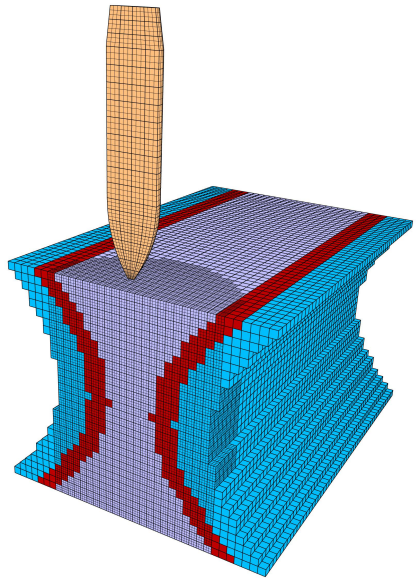

Figure 8.16: Field model of the 30 mm plate with varying hardness in two directions. The base material has been removed for illustration purposes.

The mesh was originally made in Abaqus CAE, which is a finite element software with a graphical interface. Afterwards the mesh raw data were converted in Matlab for use in IMPETUS Afea. The script can be found in Appendix F. In short, the script takes the midpoint of every element in the mesh and checks its position according to Figure 8.17, and thereafter gives the element a certain part number for use in IMPETUS Afea. A closer look at Figure 8.16 also shows that the mesh is set up with 64 node cubic hex-

ahedron elements in a radius of 12 mm from the point of impact. The model contains 1.2×10^5 elements and 3.2×10^5 nodes, which makes it computationally expensive. Running one simulation takes about 15 hours on a high performance GPU computer, making this model unfit for regular laptops.

The field model does not have a pin hole like the 1/12 model. Since fairly large cubic elements have been used, the pin hole would have been relatively large not physically justifiable. In addition, the pin hole needed to be in six different locations. Making six different models was too time consuming. Instead a larger time step erosion limit, than used in the 1/12 model, was set at 3×10^{-9} s. 1×10^{-9} s was also tried, but at this level the projectile started entering into the mesh of the plate and destroy the simulation. With no pin hole and no element erosion at damage (elements only loosing their shear stress resistance), the projectile could not make a cavity in the mesh. Some elements had to be removed. A larger time step erosion limit, solved this.

Otherwise the 30 mm field model has been set up with the same material parameters as the updated initial model.

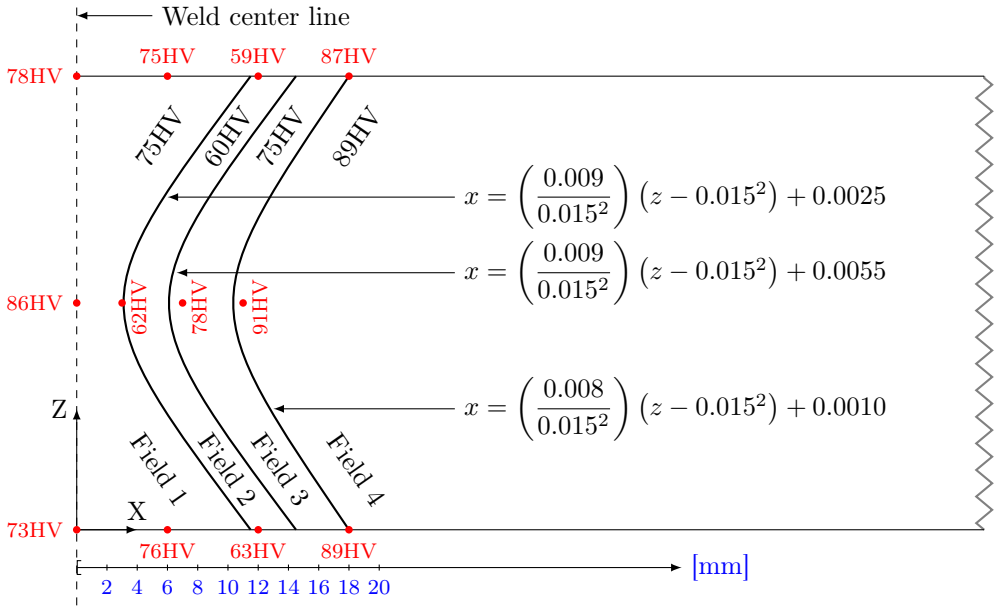

Figure 8.17: 30 mm field model. Red numbers represent hardness measurements from Chapter 5. Each field has been assigned an average hardness value and the curves are represented by functions used by Matlab to assign elements to different fields.

8.4 Overview of Numerical Tests

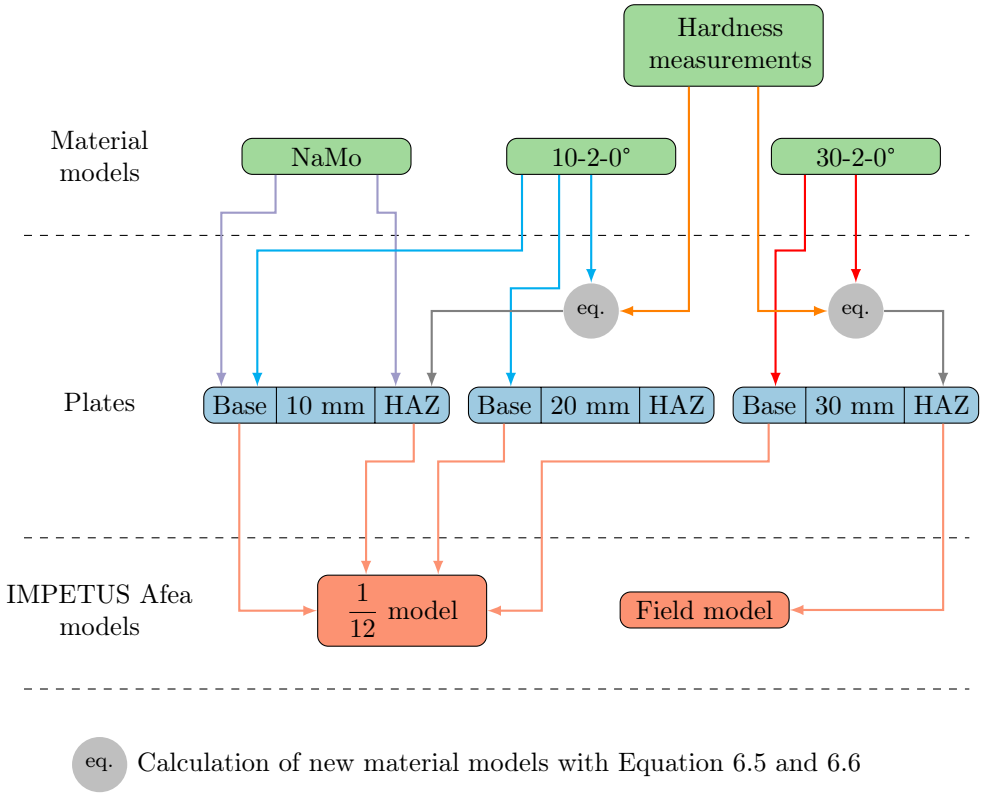

Figure 8.18: Overview of numerical simulations

As Figure 8.18 shows, most of the IMPETUS Afea simulations in this thesis have been done on the 10 mm plate. This is a natural consequence of the fact that a NaMo material model only was available for this plate. The HAZ material models have been made for the distances 0, 4, 6, 8, 10 and 14 mm from the weld centerline. NaMo material models for the HAZ are calibrated for the same distances except for the weld (0 mm). Each position for each material needs four simulations to estimate a v_{bl}. So for the 1/12 model this means eight base material simulations (NaMo and 10-2-0°) of the 10 mm plate, and four base material simulations for each of the 20 mm and 30 mm plate. In addition 24 HAZ simulations from material models made from 10-2-0° and hardness measurements (see Section 6.3) and 20 HAZ simulations from the NaMo material model. In total 60 simulations on the 1/12 model.

The field model has only been tested for the 30 mm plate because of its computational cost. Here four simulations were run for each of the same positions mentioned above, and four simulations in the base material. The following sections will present and comment on the results from the simulations.

8.5 Ballistic Simulation Results

All v_{bl} values have been found through three or more ballistic simulations in IMPETUS Afea with subseqent Recht-Ipson curve fitting using Matlab. The velocities used for each plate are listed in Table 8.2. If the projectile stopped at a given velocity, an increment of 25 m/s were added to v_i, and at least three simulations were run where $v_r > 0$. This was necessary to get a satisfying curve fit from Matlab.

Table 8.2: Initial velocities used in IMPETUS Afea

	Plate	v_i [m/s]
$\frac{1}{12}$ model	10 mm	275, 300, 325, 350, 375, 400 and 425
	20 mm	475, 500, 525, 550, 575, 600 and 625
	30 mm	625, 650, 675, 700 and 725
Field model	30 mm	650, 675, 700 and 725

Table 8.3 gives the ballistic limit velocities for all numerical simulations compared to the experimental ballistic limits and a short comment. The table shows that, for the base material of the 10 mm plate, the result is a nearly perfect fit. As explained in Section 8.2, this is the updated initial model which was calibrated to fit the experimental results, so this result was expected. For the weld in the 10 mm plate, v_{bl} is conservative, while simulations through the HAZ are somewhat non-conservative.

The simulations using the NaMo material model for the 10 mm plate, are generally conservative, except for 14 mm from center weld. This can be explained by the fact that the current version of NaMo does not account for stage IV hardening, which is highly relevant for this study, as the strains imposed on the material are quite large.

For the 20 mm and 30 mm plates, the HAZ is not vertical through the plate thickness. Therefore, a field model has been developed for simulations across the HAZ of the 30 mm plate. For more information on the field model, the reader is referred to Section 8.3. For the 20 mm plate, only the base material has been simulated. This was done, using the 10-2-0° material model, as no material testing have been performed on the 20 mm plate.

It is seen that the results of the simulations in the base material of the 20 mm plate is highly non-conservative, using the initial model. Additional simulations have therefore been performed with no friction, $\mu = 0$. As Table 8.3 shows, this gave conservative results. The same was found for the base material of the 30 mm plate. It has been discussed that the stronger influence of friction in thicker plates, comes from the larger contact surface between projectile and target during perforation.

The results from the simulations using the 30 mm plate field model are all non-conservative.

Figure 8.19, 8.20 and 8.21 show Recht-Ipson curves from simulations along with the experimental Recht-Ipson curves.

Table 8.3: Results from ballistic simulations in IMPETUS Afea

IMPETUS Afea model	Material model	Target	DFCW[a] [mm]	$v_{bl}^{impetus}$ [m/s]	v_{bl}^{exp} [m/s]	Comment
10 mm $\frac{1}{12}$	10-2-0°	Base	25+	347	347	Good fit
	10-2-0° + hardness	Weld	0	322	335[b]	OK
		HAZ	4	323	312	OK
			6	322	312	OK
			8	317	312	OK
			10	329	312	OK
			14	335	312	OK
	NaMo	Base	-	338	347	Good fit
		HAZ	4	302	312	OK
			6	287	312	OK
			8	269	312	OK
			10	309	312	OK
			14	335	312	OK
20 mm $\frac{1}{12}$	10-2-0°	Base	20+	541	484	Non-conservative
				476	484	$\mu = 0$ [c]
30 mm $\frac{1}{12}$	30-2-0°	Base	25+	647	581	Non-conservative
				571	581	$\mu = 0$ [c]
30 mm $\frac{1}{2}$ field model	30-2-0°	Base	25+	617	581	OK
	30-2-0° + hardness	Weld	0	597	583	OK
		HAZ	4	600	562	OK
			6	597	562	OK
			8	598	562	OK
			10	599	562	OK
			14	605	562	OK

[a]Distance from center weld.
[b]Ballistic limit from weld since DFCW equals 0
[c]Extra set of simulations to check the effect of friction on a thicker plate

8.5.1 1/12 Model - Base Material

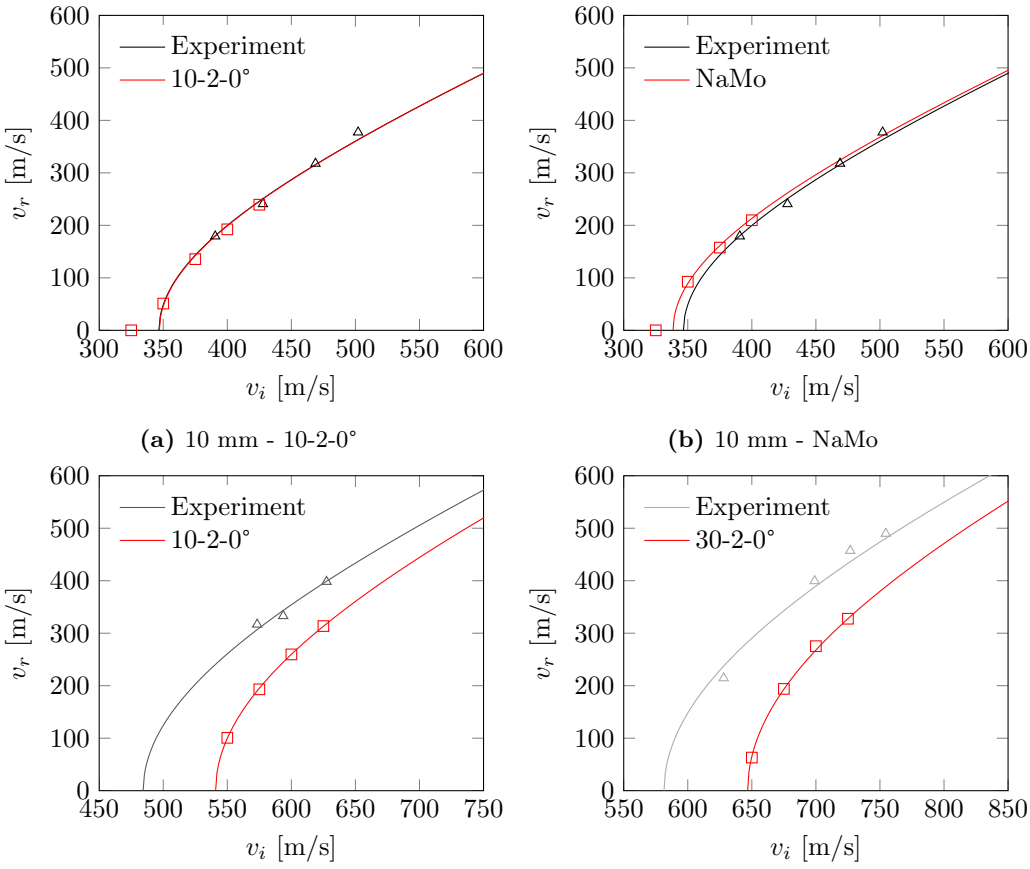

(a) 10 mm - 10-2-0°

(b) 10 mm - NaMo

(c) 20 mm - 10-2-0°

(d) 30 mm - 30-2-0°

Figure 8.19: IMPETUS Afea simulations of base material. Note the different x-axis scales.

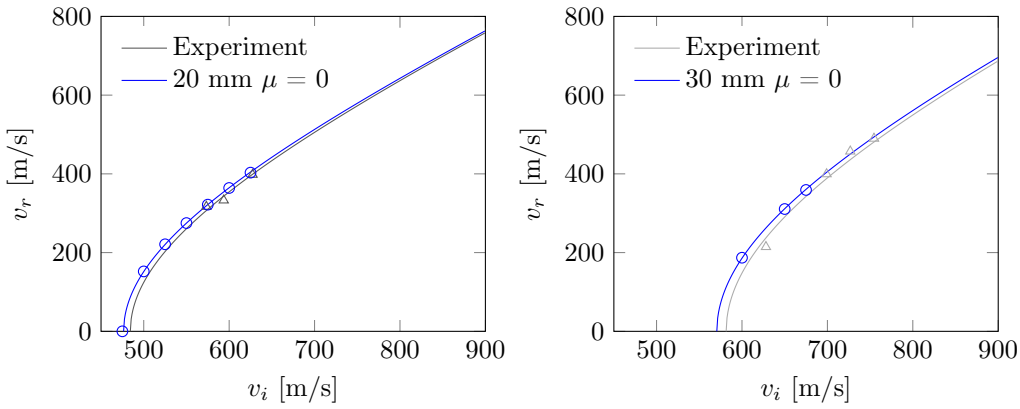

(a) 20 mm plate

(b) Friction checked on 30 mm base material

Figure 8.20: Friction check on the 20 mm and 30 mm model with base material model 10-2-0° and 30-2-0° respectively

8.5.2 1/12 Model - Weld and HAZ

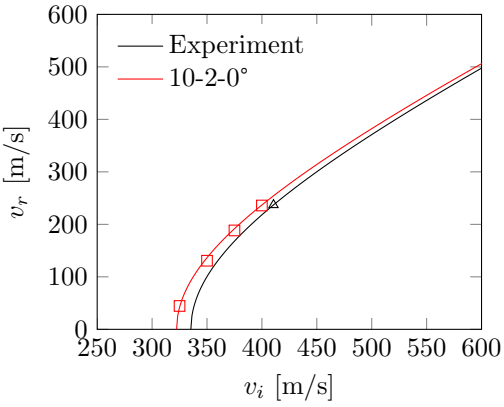

(a) Weld

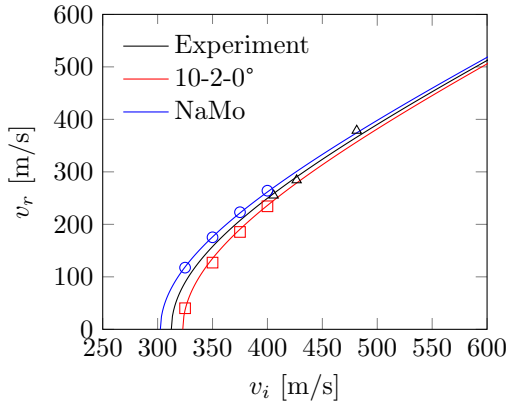

(b) 4 mm from weld center line

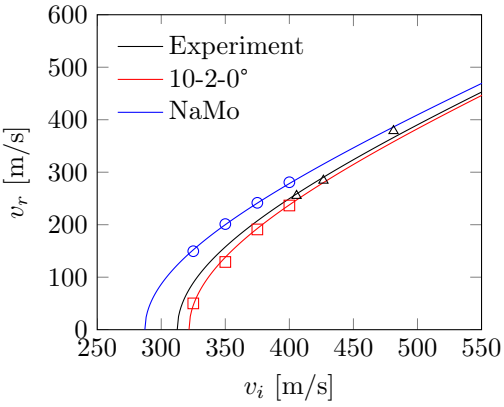

(c) 6 mm from weld center line

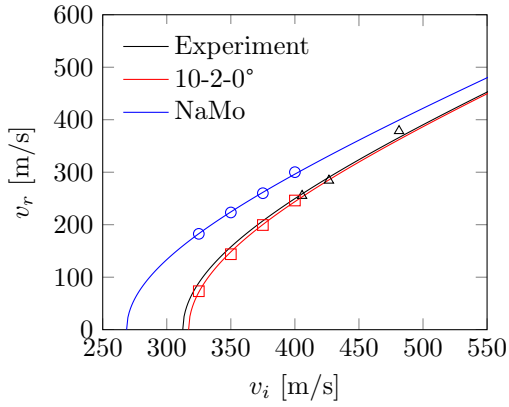

(d) 8 mm from weld center line

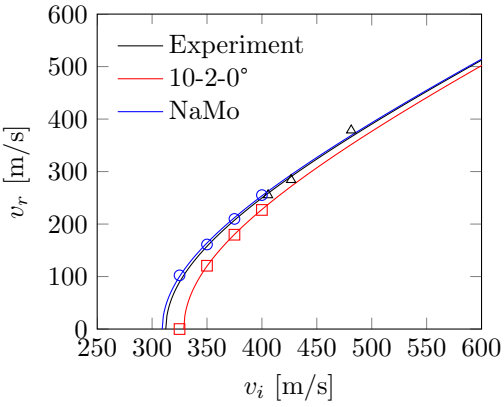

(e) 10 mm from weld center line

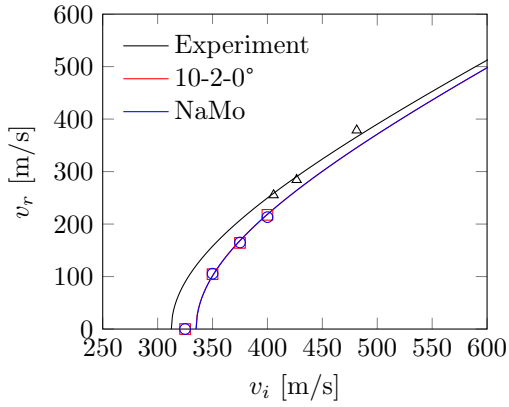

(f) 14 mm from weld center line

Figure 8.21: Numerical simulations of the weld and the HAZ with IMPETUS Afea for the 10 mm plate.

8.5.3 Figures from 1/12 Model Simulations

In this section some screen shots from IMPETUS Afea Solver are presented. Figure 8.22 shows the 1/12 model with thicknesses 10 mm, 20 mm and 30 mm used in the simulations.

Figure 8.23a shows a partially perforated plate and a damage scale. The projectile has been removed for illustration purposes. It is seen that all elements in contact with the projectile has maximum damage. Thus, Figure 8.23b shows that none of the elements in contact with the projectile takes any deviatoric stresses. Figure 8.23c shows the plate with the partially perforated APM2 bullet.

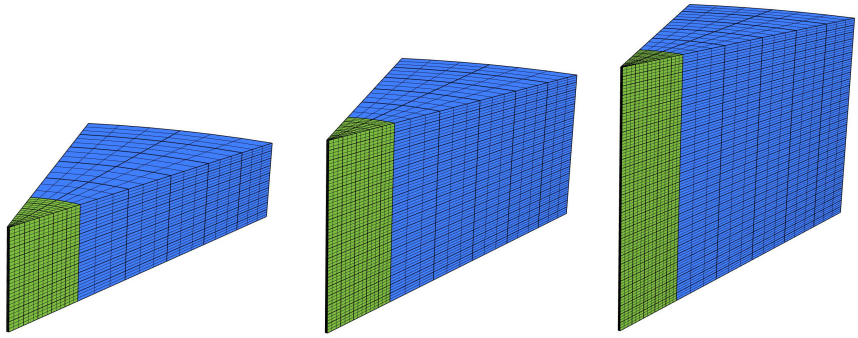

Figure 8.22: The three different thicknesses tested with the 1/12 model.

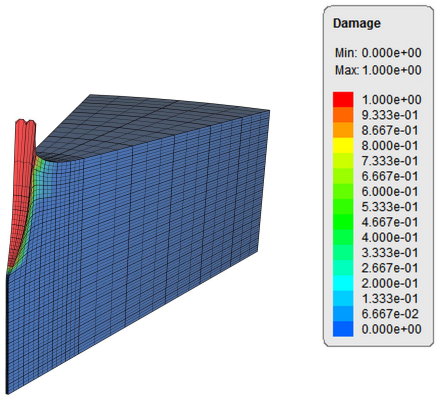

(a) Damage

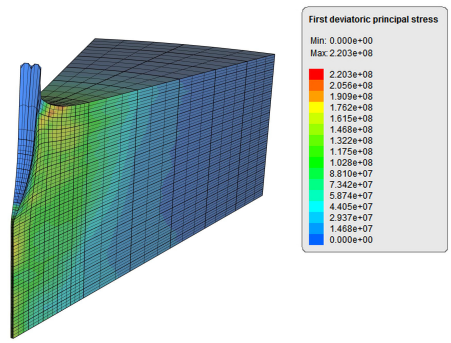

(b) Deviatoric stresses

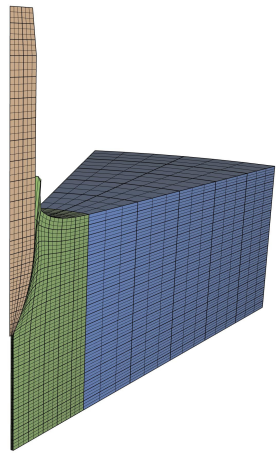

(c) Mesh with APM2 steel core

Figure 8.23: Damaged elements compared with deviatoric stresses in the same elements.

8.5.4 30 mm Field Model Results

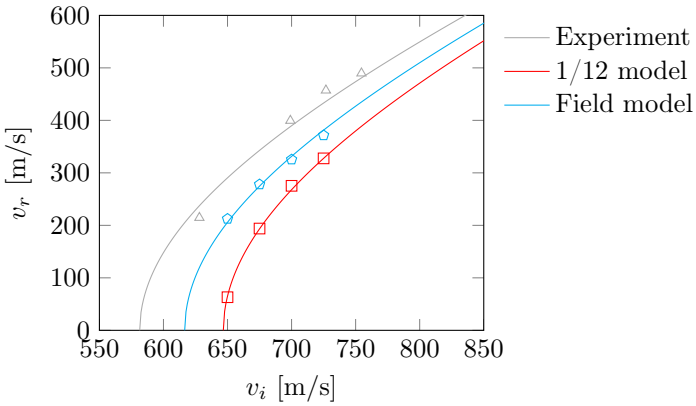

Figure 8.24: Base material simulation of 30 mm field model. The base material results from the 1/12 model have been plotted for comparison.

First, the base material was tested with the 30 mm field model. Material parameters from 30-2-0° were used, and the results can be seen in Figure 8.24 and Table 8.3. The field model is more conservative than the 1/12 model in the base material. This can be explained by 169 eroded elements in the field model compared to 144 (multiplied by a factor of 6 because of symmetry) in the 1/12 model. Less elements in the way creates less resistance and v_{bl} is lowered.The number of elements in the thickness direction was the same in both simulations.

Comparing the 30 mm field model with the experimental results, it is closer than the 1/12 model, but still on the non conservative side. Figure 8.25 shows the results from perforation of the weld and HAZ. Here, higher v_r in the weakest part of the HAZ was the desirable result. The field model did not behave in this way. Instead it showed almost the same v_{bl} for all the different target distances (from center weld). Chosing a larger critical time step limit for element erosion is most likely the cause. The different material fields are not able to behave in each their own way because they are eroded too early. Unfortunately, only this one study was run on the field model. Some thoughts about developing the model further are given in Chapter 12.

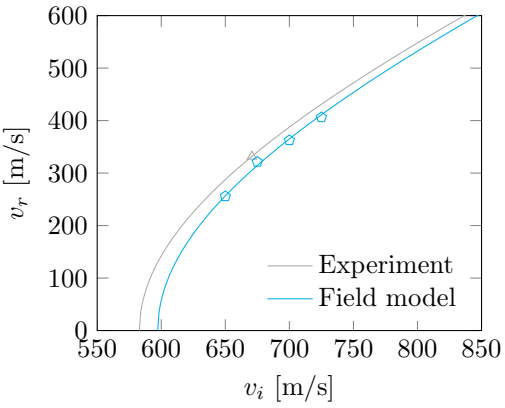

(a) Weld

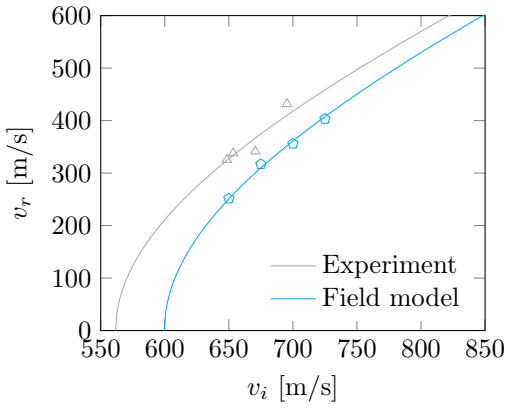

(b) 4 mm from weld center line

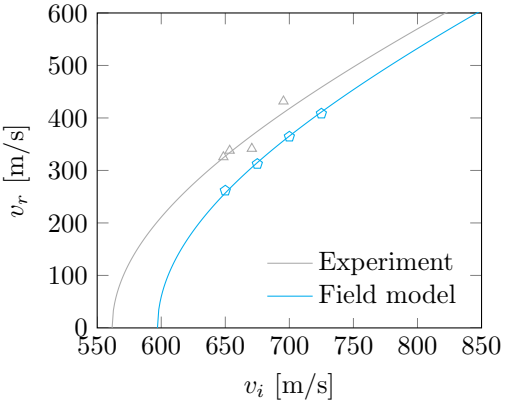

(c) 6 mm from weld center line

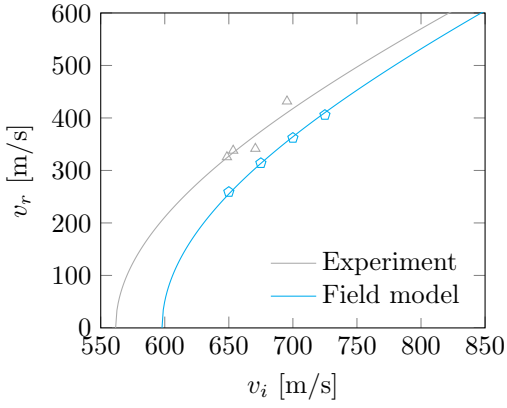

(d) 8 mm from weld center line

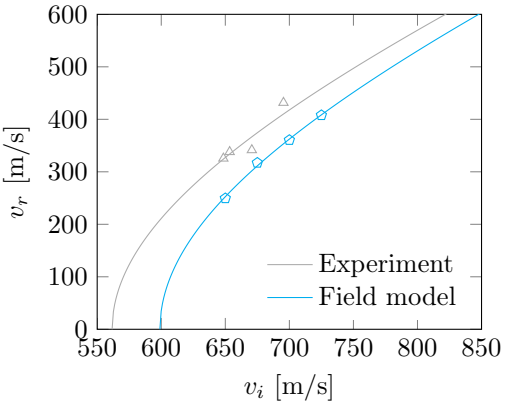

(e) 10 mm from weld center line

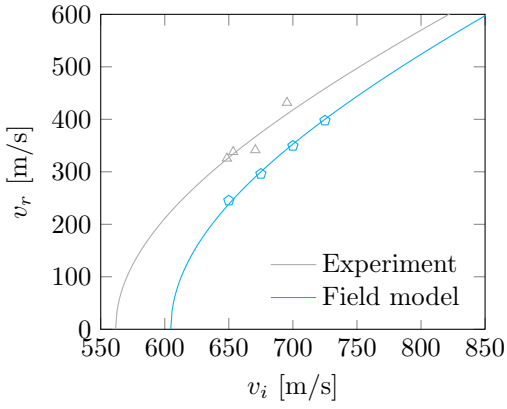

(f) 14 mm from weld center line

Figure 8.25: Numerical simulations with 30 mm field model

8.5.5 Figures from Field Model Simulations

In this section, some screenshots from IMPETUS Afea of the the 30 mm field model simulations, are shown. Figure 8.26 shows the complete field model during perforation and Figure 8.27 shows the field model without the base material to illiustrate material being laterally pushed aside. Two contour plots are shown in Figure 8.28. These illustrate the damage of the elements in contact with the projectile and that the fully damaged elements can no longer take any deviatoric stresses.

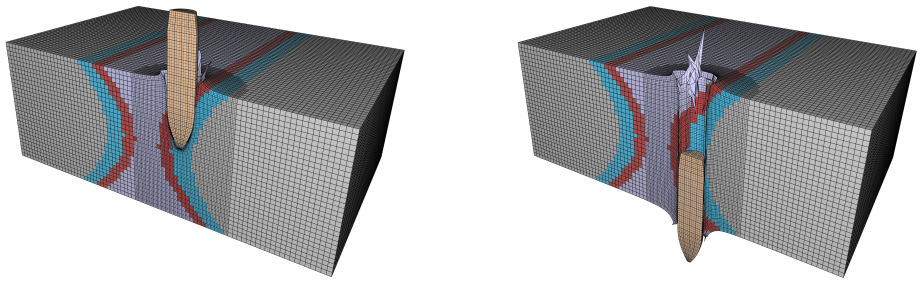

(a) Partial perforation of the plate

(b) Almost full perforation of the plate

Figure 8.26: Perforation of the 30 mm plate field model with the APM2 steel core. Symmetry plane showing.

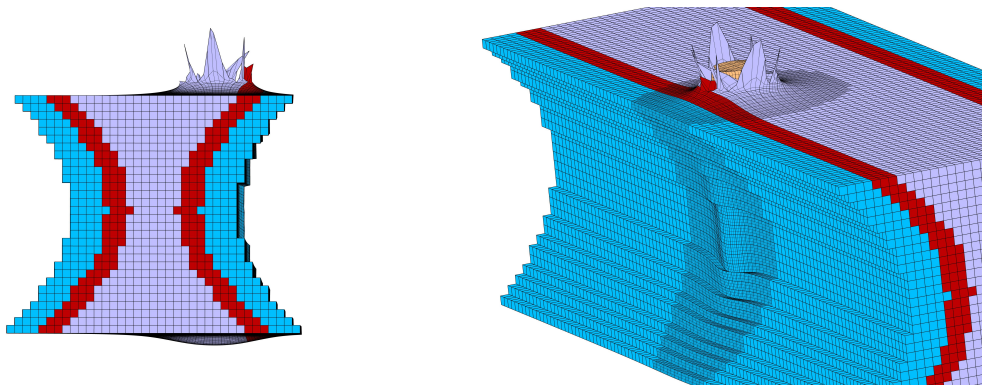

(a) View straight from the side

(b) Material being pushed laterally to open the cavity.

Figure 8.27: Perforation of the 30 mm plate field model seen from the side. The base material has been removed for illustration purposes.

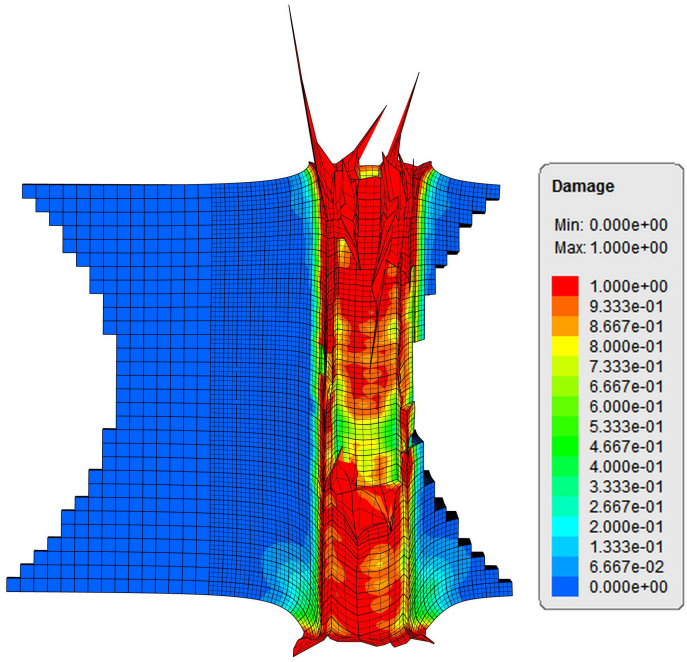

(a) Element damage

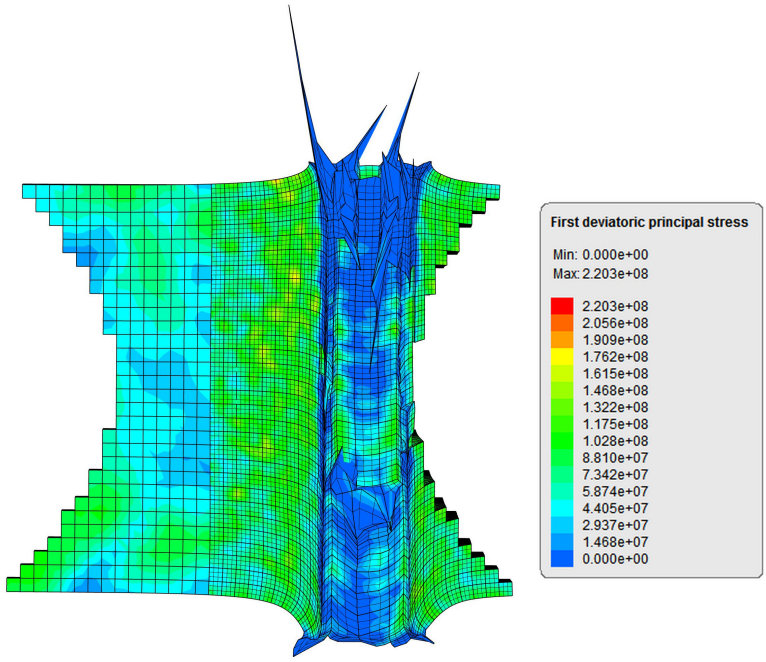

(b) Deviatoric stresses

Figure 8.28: Elements that are damaged but not eroded can not take any deviatoric stresses. The contour plots show that this is maintained in the simulations. The figure is showing the 8 mm from center weld simulation at $v_i = 675$ m/s.

CHAPTER 9

Analytical Calculations

All material models have, in addition to the numerical simulations, been run using the Cylindrical Cavity Expansion Theory, CCET. For more information on CCET, it is referred to Section 2.8. The same Matlab script was used in the Preliminary study, and is given in Appendix A.

Table 9.1 is analogous to Table 8.3 in Section 8.5. The table gives the ballistic limit velocities found using CCET and the ballistic limits from the experimental study. It is seen that the CCET is generally non-conservative. For the NaMo results however, the results are quite close to the experimental results. This is a result of the fact that the NaMo material models generally are more conservative than the 10-2-0° material model.

Figure 9.1 and 9.2 show Recht-Ipson curves for the CCET results along with the experimental Recht-Ipson curves.

9.1 Results

Table 9.1: Results from analytical calculations with CCET

Plate	Material model	Target	DFCW[a] [mm]	v_{bl}^{CCET} [m/s]	v_{bl}^{exp} [m/s]	Comment
10 mm	10-2-0°	Base	25+	394	347	Non conservative
	10-2-0° + hardness	Weld	0	357	335	OK
		HAZ	4	358	312	Non conservative
			6	356	312	Non conservative
			8	346	312	Non conservative
			10	363	312	Non conservative
			14	382	312	Non conservative
	NaMo	Base	-	387	347	Non conservative
		HAZ	4	334	312	Non conservative
			6	315	312	OK
			8	304	312	OK
			10	346	312	Non conservative
			14	381	312	Non conservative
20 mm	10-2-0°	Base	20+	572	484	Non conservative
30 mm	30-2-0°	Base	25+	673	581	Non conservative

[a]Distance from center weld.

9.1.1 Base Material

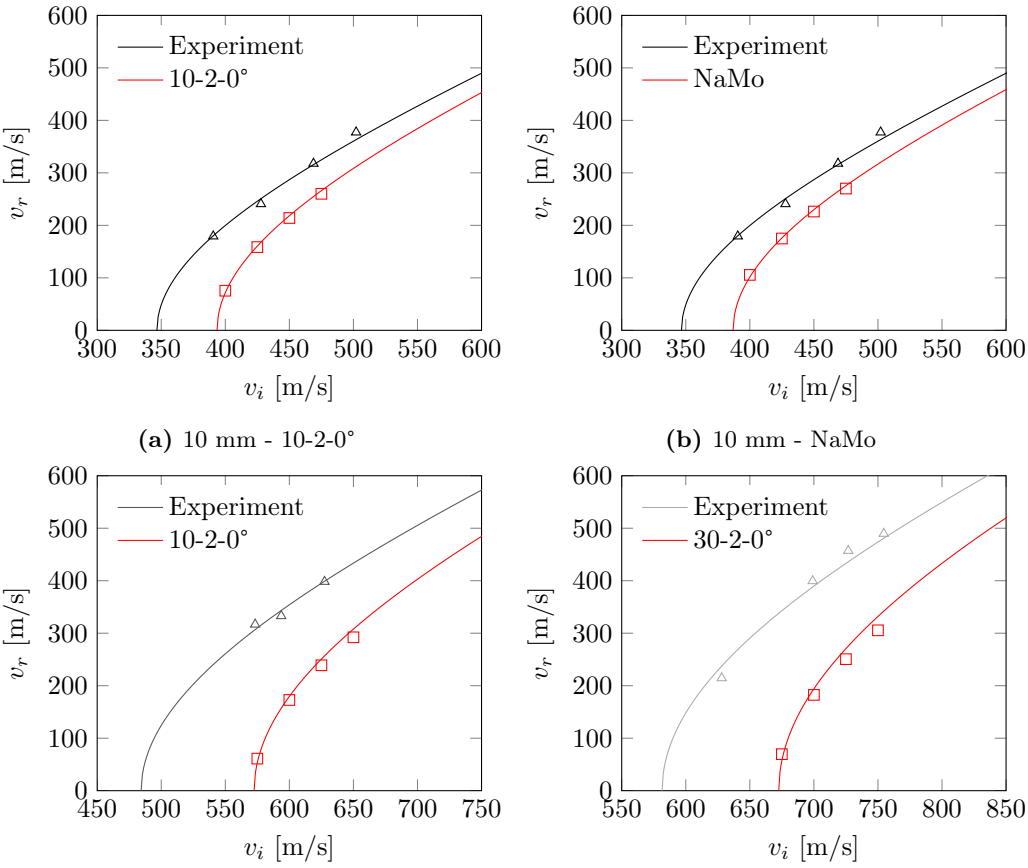

(a) 10 mm - 10-2-0°

(b) 10 mm - NaMo

(c) 20 mm - 10-2-0°

(d) 30 mm - 30-2-0°

Figure 9.1: CCET of base material

9.1.2 Weld and HAZ

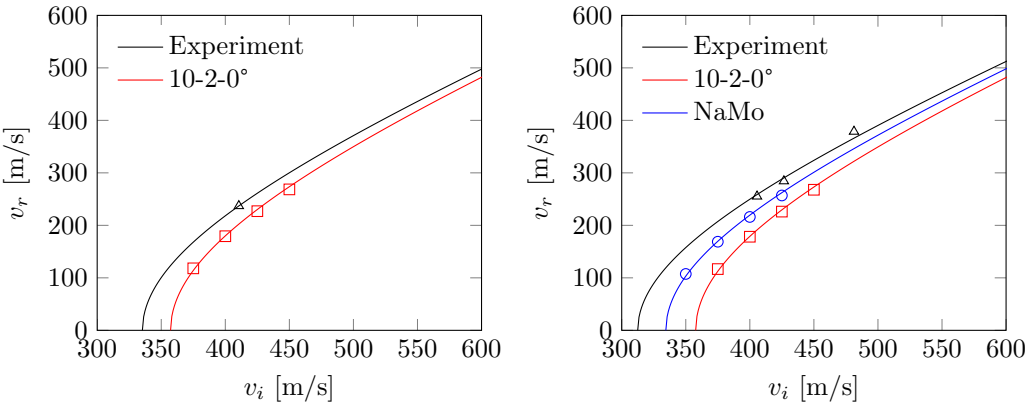

(a) Weld

(b) 4 mm from weld center line

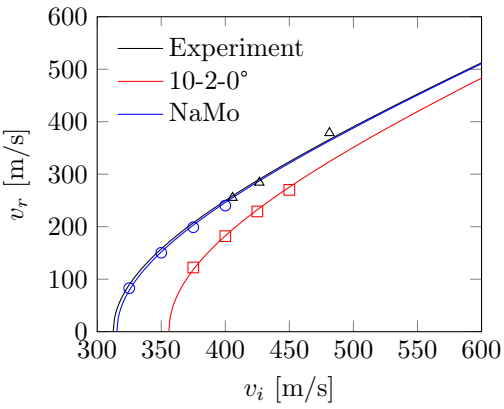

(c) 6 mm from weld center line

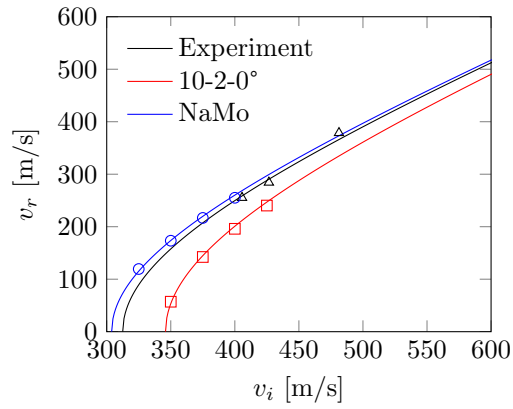

(d) 8 mm from weld center line

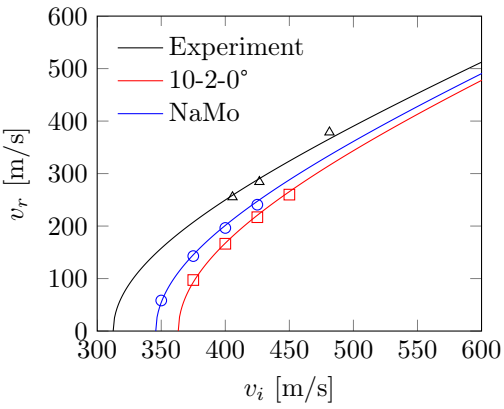

(e) 10 mm from weld center line

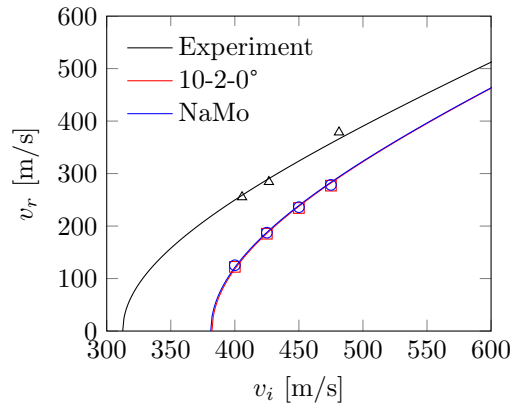

(f) 14 mm from weld center line

Figure 9.2: Analytical calucations with CCET

CHAPTER 10

Comparison of Results

Figures 10.1 and 10.2 compare the results from the numerical and analytical study. A negative value means that the ballistic limit velocity is conservative. For each part of the plate, the figure gives four bars. One for IMPETUS Afea running with 10-2-0° tensile test material model, one for IMPETUS Afea running with NaMo generated material model, one for CCET running with 10-2-0° material model and one with CCET running with NaMo material model. No material model for the weld has been generated using NaMo. This is seen as two empty spaces above the column *Weld*.

The results from IMPETUS Afea simulations of the 10 mm plate base material fits perfectly, with zero percent error. As discussed in Section 8.5, this is somewhat because the model was calibrated for the 10 mm plate in the base material. It is generally seen that the CCET gives non-conservative results, while the NaMo material model gives conservative results.

The non-conservative results for the IMPETUS Afea simulations of the 20 mm and 30 mm plates are probably due to the friction. Though this gave nearly perfect result for the 10 mm plate, the effect was too large for the 20 mm and 30 mm plates. A previous study by Holmen and Johnsen [28], yielded conservative results for most IMPETUS Afea simulations. These simulations were, however, performed using no friction.

As Figures 10.1 and 10.2 show, many of the results are quite non-conservative. It has therefore been discussed using larger time steps as this would lead to more elements eroded, and with that giving more conservative results. However, as this would have to be consider non-physical this has been avoided. It has also been discussed using no friction to make the results more accurate, however, this could also be considered somewhat non-physical. One possibility is to use a factor of safety, as this is the normal convention for structural problems in the Eurocode.

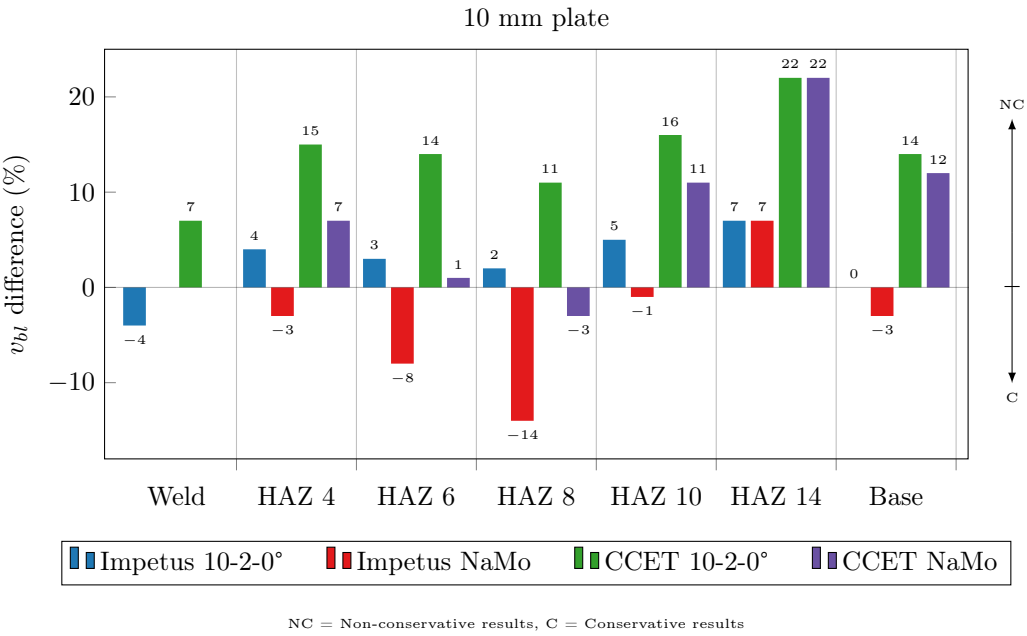

Figure 10.1: v_{bl} difference from experimental values for the 10 mm plate

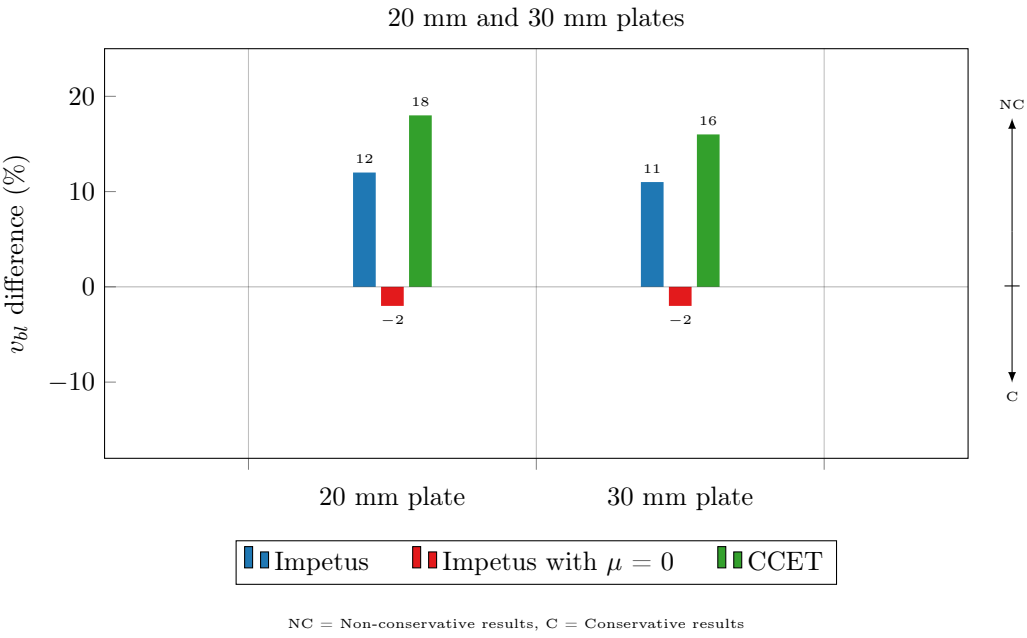

Figure 10.2: v_{bl} difference from experimental values for the 20 mm and 30 mm plates

CHAPTER 11

Conclusion

As there are many variables involved in ballistic experiments, a large number of tests should be performed, for the results to be statistically significant. As the cost of experimental testing is quite high, the experimental part of this thesis is limited and the results should be interpreted accordingly. However, trends have been observed, that coincide with the results from the preliminary study.

The literature describes the process of heat treating aluminium alloys and the following effect on its material properties. Artificial ageing at elevated temperatures can strengthen an alloy, overaging however leads to reduced strength. As elevated temperatures are inevitable with welding, overaging in the vicinity of the weld is a consequence, and we get a heat affected zone. Tensile testing across the HAZ has not been performed in this study. However, hardness measurments have been done. Using a simple conversion equation, it was possible to estimate the yield strength of the material.

In addition to the tensile tests and hardness measurements, a numerical analysis of the material properties have been performed. Using WELDSIM, a finite element software for heat flow, the heat affected zone has been estimated. The resulting temperature fields were used as input in NaMo, Nano Structure Model, to calculate the stress-strain curves across the HAZ. As Figures 7.7 and 7.8 show, the results are in good agreement with the experimental material testing.

Based on these promising results, it seems reasonable to trust the stress-strain curves generated by NaMo. It also somewhat validates the conversion equation from measured Vickers hardness to predicted yield stress.

Eurocode 9[34] estimates the width of the HAZ for welded aluminium structures. Table 5.2 compares the width found from hardness measurements across the HAZ, width the tabulated width found in the Eurocode. It is seen that for the 10 mm plate, the width of the HAZ is somewhat conservative in the Eurocode, but within reason. For the 20 mm and 30 mm plate thicknesses, the Eurocode overestimates the widths of the HAZ by 57 % and 63% respectively. This can be considered overly conservative.

Numerical simulations using the non-linear finite element code Impetus Afea Solver have been performed on the base material of every plate and across the HAZ of the 10 mm and 30 mm plates.

The results for the 10 mm plate base material gave a nearly perfect fit compared to the experimental results. This can be explained by the fact that the initial numerical model was calibrated using the 10 mm plate base material, so the parameters were altered to best describe these experimental results. Most important was adding friction to the model. With no friction, the numerical simulations were more conservative. For the 20mm and 30mm plates, the results were non-conservative. This could be a result of the added friction from the larger contact area between projectile and target during penetration. Some extra simulations were performed on the 20 mm and 30 mm plates, using no friction. The results were somewhat conservative, but quite close to the experimental values.

As Figures 5.1, 5.2 and 5.3 illustrate, the width of the HAZ is constant through the thickness of the 10 mm plate, while for the 20 mm and 30 mm plates, the width of the HAZ varies. Because of this, a numerical model for the 10 mm plate could be modelled with vertical segments of varying strengths across the HAZ. For the 20 and 30 mm plates, however, a more complicated model needed to be developed. Because of the large amount of work this would entail, such a model was only attempted for the 30 mm plate. The model can be seen in Figure 8.16

The results from the field model of the 30 mm plate were not very satisfying. A larger difference in v_{bl} was expected. Results show that the field model could not describe the effect of varying hardness and yield strength in the thickness direction. The field model results were very similar for all simulated distances from weld center line. Since the model was very computationally expencive, only one study was done. The introduction of a pinhole, a finer mesh and/or a lower t_{cr}, might change the overall behaviour of the model.

The analytical approach, using Cylindrical Cavity Expansion Theory, proved an effective way of finding the ballistic limit velocity. As it is a closed form solution, it requires substantially less computational force than numerical simulations. For the preliminary study, the results were satisfactory, though somewhat non-conservative. But it gave us a good idea of the velocity regimes necessary to achieve perforation. For the analytical study, however, the results could not compare to the good results from the numerical study. As Figure 10.1 shows, the results for the 10 mm plate were as much as 22% non-consrvative.

As the ballistic experiments showed little sign of fragmentation, this has not been taken into consideration. Instead, ductile hole growth have been assumed to be the governing failure mode.

Impetus Afea Solver with its powerful 64-node element description, has yielded good results and has been nice to work with. Few input parameters have made it easy figuring out which parameters are doing what. The total energy loss for all simulations has been kept below 5-10%. Holmen and Johnsen [28] had some problems with the total energy in similar numerical simulations, but none of these problems have occured during the work of this thesis. It seems that this problem has been resolved. The built in meshing functions of Impetus Afea Solver have proven very accurate and versatile. Some shapes and functions are still missing, but these will probably emerge in upcoming releases.

CHAPTER 12

Further Work

After some discussion, the following paragraphs were suggested subjects for further investigation.

Material Testing

Tensile testing across the width of the HAZ should be performed to more accurately find the parameters of the material model. Material testing should also be carried out for the 20 mm plate.

Ballistic Experiments

More ballistic experiments should be performed, to give a more statistically significant foundation for the study.

Blunt Projectile

Investigate the effect of blunt projectile impact in the HAZ and weld.

Field Model

Further development of the field model to better capture the effect of the curved HAZ through the tickness of the plate. Some improvents are suggested:

- Using a *pin hole* instead of a fracture criterion could remove a source of insecurity.
- Build the model with more fields of varying strength.
- A refined mesh should be investigated. However this would require developing a 1/12 model with two symmetry planes, as the computational cost is quite high.
- A lower time step should be investigated, to avoid time step erosion.

Anisotropic Material Response

For the 30 mm material testing, some anisotropy was observed. An anisotropic material model should be investigated.

Boundary Condition

As the boundary condition from the ballistic experiments were hard to model, in addition to the parameter study suggesting boundary conditions to be superfluous, it has been neglected in this study. However additonal investigation into this should be done.

Mesh Sensitivity

More investigation into the sensitivity of element size should be carried out.

Friction

Friction proved to be a quite sensitive parameter for the ballistic simulations, and further investigation should be carried out.

Parameter study

A more thorough parameter study should be performed for each plate thickness.

Weldsim implementation

Weldsim is already being implemented in IMPETUS Afea, but it has not been tested in this thesis. With this module implemented, finite element meshes with thermally treated material can be directly used in simulations with IMPETUS Afea.

Bibliography

[1] T. Børvik. Private communication, 2014.

[2] R. D. Cook, D. S. Malkus, M. E. Plesha and R.J. Witt. *Concepts and Applications of Finite Element Analysis*. John Wiley and Sons, 4th edition, 2002.

[3] O.R. Myhr B.I. Bjørneklett, Ø. Grong and A.O. Kluken. A Process Model for the Heat-Affected Zone Microstructure Evolution in Al-Zn-Mg Weldments. *Metallurgical And Materials Transactions*, 30A:2667–2677, 1997.

[4] T. Børvik. An Introduction to Impact and Penetration Dynamics, 2013.

[5] J.A. Zukas. *Impact Dynamics*. John Wiley and Sons, 4th edition, 2002.

[6] J. Johnsen, J.K. Holmen, O.R. Myhr, O.S. Hopperstad, and T. Børvik. A nano-scale material model applied in finite element analysis of aluminium plates under impact loading. *Computational Materials Science*, 79(0):724 – 735, 2013.

[7] G.T. Camacho and M. Ortiz. *Computer Methods in Applied Engineering*, 42:269–301, 1997.

[8] M. E. Backman and W. Goldsmith. The Mechanics of Penetration of Projectiles Into Targets. *international Journal of Engineering Science*, 16:1–99, 1978.

[9] O. S. Hopperstad and T. Børvik. Lecture Notes - Material Mechanics Part 1, 2013.

[10] K. M. Mathisen. TKT4197: Ikke-lineær elementmetode [Forelesningsnotater], 2013.

[11] Hydro Aluminum. `http://www.hydro.com/en/About-aluminium/`. Cited: 2014-02-19.

[12] W. D. Callister and D. G. Rethwisch. *Material Science and Engineering, an Introduction*. John Wiley and Son, 7th edition, 2007.

[13] European Aluminium Association, MATTER. `http://aluminium.matter.org.uk`. Cited: 2014-02-15.

[14] Aluplanet.com. `http://www.aluplanet.com/`. Cited: 2014-05-22.

[15] T. Wang. Modelling of welded thin-walled aluminium structures, 2006.

[16] American Galvanizers Association. `http://www.galvanizeit.org/`. Cited: 2014-02-15.

[17] Gas metal arc welding. `http://en.wikipedia.org/wiki/Gas_metal_arc_welding`. Cited: 2014-05-22.

[18] T. Wang et. al. Finite element analysis of welded beam-to-column joints in aluminium alloy EN AW-6082 T6. *Finite Elements in Analysis and Design*, 44:1–16, 2007.

[19] R. F. Recht and T. W. Ipson. Ballistic Perforation Dynamics. *Journal of Applied Mechanics*, 30:384–390, 1963.

[20] G. Ben-Dor, A. Dubinsky and T. Elperin. On the Lambert–Jonas Approximation for Ballistic Impact. *Mechanics Research Communications*, 29:137–139, 2002.

[21] Instron. Vickers test. `http://www.instron.us/wa/applications/test_types/hardness/vickers.aspx`. Cited: 2014-03-15.

[22] G. R. Johnson and W. H. Cook. A Constitutive Model and Data For Metals Subjected To Large Strains, High Strain Rates and High Temperatures. *Proceedings of the 7th International Symposium on Ballistic*, pages 541–547, 1983.

[23] L. Olovsson. Impetus user guide, 2013.

[24] T. Børvik, S. Dey and A. H. Clausen. Perforation resistance of five different high-strength steel plates subjected to small-arms projecttiles. *International Journal of Impact Engineering*, 36:948–964, 2009.

[25] M. J. Forrestal, T. Børvik, T. L. Warren and W. Chen. Perforation of 6082-T651 Aluminum Plates with 7.62 mm APM2 Bullets at Normal and Oblique Impacts. *Experimental Mechanics*, 2013.

[26] R. Hill. *The Mathematical Theory of Plasticity*. Oxford University Press, 2nd edition, 1998.

[27] J. Johnsen. Acomplete derivation of the Cylindrical Cavity Expansion Theory with Voce Law work hardening, 2014.

[28] J. K. Holmen and J. Johnsen. Effects of Heat Treatment on the Ballistic Properties of AA6070 Aluminium Plates. Master's thesis, NTNU, 2012.

[29] Till Tantau. *The PGF/TikZ manual*, 2010.

[30] Dr. Christian Feuersänger. *PGFPlots Manual*, 2013.

[31] K. S. Rostad. Corrosion of welded AA6082 in arctic marine environments. Master's thesis, NTNU, 2014.

[32] T. Børvik, S. Dey L. Olovsson, and M. Langseth. Normal and oblique impact of small arms bullets on AA6082-T4 aluminium protective plates. *International Journal of Impact Engineering*, 38(7):577 – 589, 2011.

[33] O. R. Myhr. Comments on material composition of welded aluminium plates. Private communication, 2014.

[34] Standard Norge. Eurokode 9: Prosjektering av aluminiumskonstruksjoner. Technical report, Standard Norge, 2007.

[35] T. Børvik. The tension test, 2013.

[36] O. R. Myhr, Ø. Grong and S. J. Andersen. Modelling of The Age Hardening Behaviour of Al-Mg-Si Alloys. *Acta Materialia*, 49:65–75, 2000.

[37] O. S. Hopperstad. Comments on saturation levels in EN AW-6082 T6. Private communication, 2014.

[38] O. R. Myhr, Ø. Grong, O. G. Lademo and T. Tryland. Optimizing Crash Resistance of Welded Aluminum Structures. *Welding Journal*, 2009.

[39] O. R. Myhr. Simulation and Modelling in Hydro - Examples from Welding of Aluminium, 2013.

[40] O. R. Myhr, S. Klokkehaug, O. Grong, H. G. Fjær and A. O. Kluken. Modeling of Microstructure Evolution, Residual Stresses and Distortions in 6082-T6 Aluminum Weldments. 1998.

[41] C. Dørum, O. G. Lademo, O. R. Myhr, T. Berstad and O. S. Hopperstad. Finite element analysis of plastic failure in heat-affected zone of welded aluminium connections. *Computers and Structures*, 88:519–528, 2009.

[42] O. R. Myhr, Ø. Grong and K. O. Pedersen. A Combined Precipitation, Yield Strength, and Work Hardening Model for Al-Mg-Si Alloys. *The Minerals, Metals Materials Society and ASM International*, 41A:2276–2289, 2010.

[43] J.A. Zukas. *High Velocity Impact Dynamics*. John Wiley and Sons, 1990.

APPENDIX A

CCET - Matlabscript

```
clc;
clear all;
close all;

% material constants
Y = 240e6;
E = 70000e6;
ny = 0.33;
vi = 560;

%Material constants from Wang Hoperstad 2007
voce_q = [72e6,52e6];
voce_c = [3196,29];

% APM2 bullet
a = 3.085e-3; % radius of projectile
rho_p = 7850; % density of projectile
rho_t = 2700; % density of target
l = 10.2e-3; % nose length
L = 16.8e-3; % shank length
h = 20e-3; % target thickness

V = 0.00001:0.1:(1/(sqrt(rho_t/Y)));

psi = 0.25*(((l/a)^2)+1);
gamma2 = (2*(1+ny)*Y)/(sqrt(3)*E);
gamma = sqrt(gamma2);
b = 1-gamma2;
k = @(x) ((4*(x^2))-((4*x)/3)+(1/3)) - ...
    ((((4*(x^2))*((2*x)-1))/(sqrt((4*x)-1)))
    * asin(sqrt((4*x)-1)/(2*x)));
k1 = k(psi);

alpha2 = (sqrt(3)*(1-(2*ny))*rho_t*(V.^2))/(2*(1-ny)*Y);


f1 = @(x) (x.^(voce_c(1)/(sqrt(3)))./(1-x);
voce_sum1 = (voce_q(1)*(log(gamma) + 0.5*integral(f1,0,b)));

f2 = @(x) (x.^(voce_c(2)/(sqrt(3)))./(1-x);
voce_sum2 = voce_sum1 + (voce_q(2)*(log(gamma) + 0.5*integral(f2,0,b)));

```

```
42 sigma_s = (1/sqrt(3))*((Y*(1-(2*log(gamma))))-(2*voce_sum2));
43
44 B = 0.5*(((1./((1-ny).*sqrt(1-alpha2))).*log((1 + ...
       sqrt(1-alpha2))./sqrt(alpha2)))
45     + gamma2 - (2*log(sqrt(gamma2))) - 1);
46
47 sigma_r = sigma_s + (rho_t.*B.*V.^2);
48
49 Xdata = sqrt(rho_t/Y)*V;
50 Ydata = sigma_r/Y;
51
52 f3 = fittype(@(a,b,x) a+b.*x.^2);
53 g = fit(Xdata',Ydata',f3,'startpoint',[1,1], ...
       'algorithm','levenberg-marquardt');
54
55 aa = coeffvalues(g);
56 B0 = aa(2);
57 ff = @(x) Y+B0.*x.^2;
58
59 N = @(x) ((8*x^2)*log((2*x)/((2*x)-1)))-(1+(4*x));
60
61 C = (h*rho_t*B0*N(psi))/((L+(k1*l))*rho_p);
62
63 Vbl = @(C) ...
       (((2*sigma_s*h)/(rho_p*(L+k1*l)))^(0.5))*((1+C+((2*(C^2))/3))^(0.5));
64
65 Vr = @(C,Vs,Vbl) (((Vs.^2)-(Vbl.^2)).^0.5).*(1-C+(0.5*C));
66
67 Vs = Vbl(C):0.1:vi;
68 Vs2 = Vbl(0):0.1:vi;
69
70 vbl = Vbl(C);
71 vr = Vr(C,vi,Vbl(C));
```

APPENDIX B

Tensile Tests - Raw Data

The following pages contains the raw data results from tensile testing. Results are given in force against diameter reduction. Tensile tests have been performed by SINTEF Materials and Chemistry. The raw data have also been run through a filter developed by SINTEF Materials and Chemistry to remove noise originating from actual experiments.

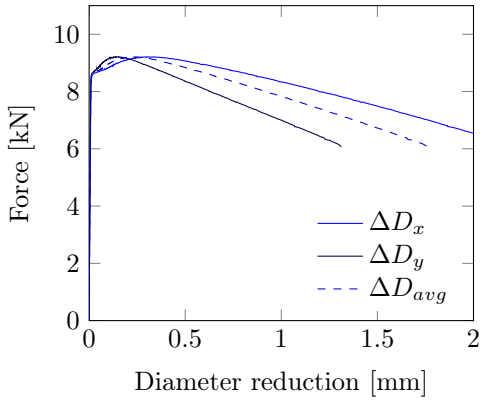

(a) Specimen 10-1-0°

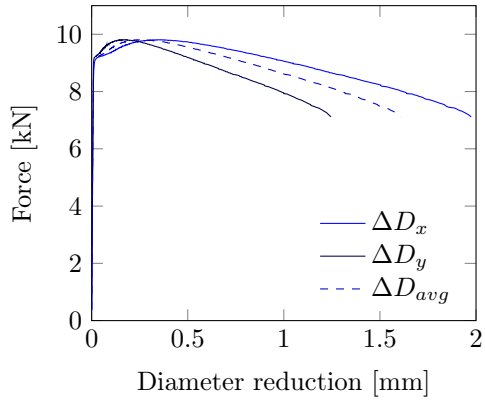

(b) Specimen 10-2-0°

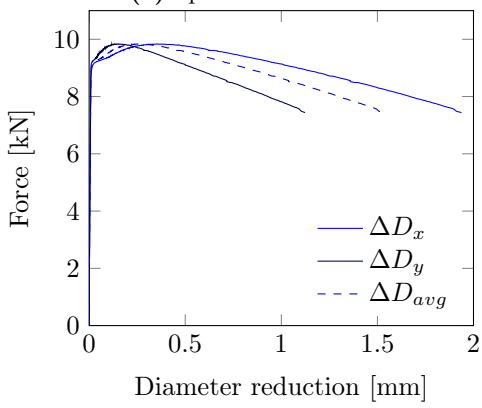

(c) Specimen 10-3-0°

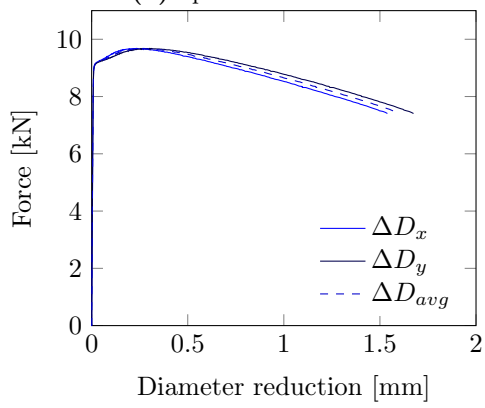

(d) Specimen 10-4-90°

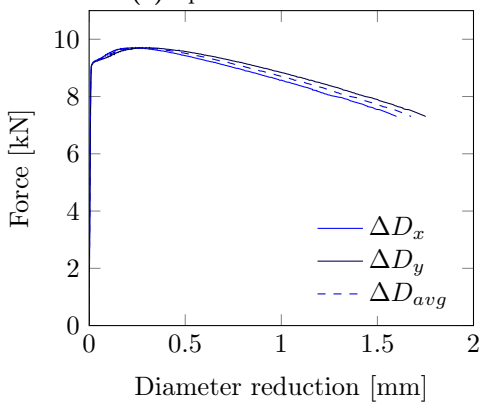

(e) Specimen 10-5-90°

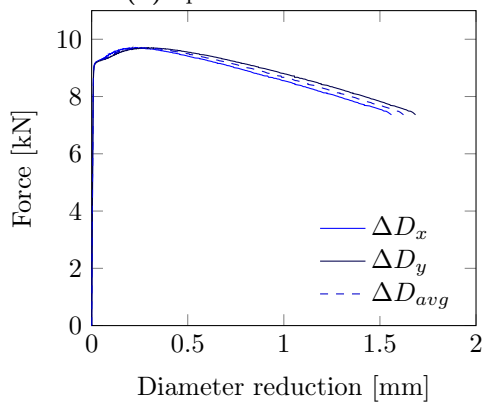

(f) Specimen 10-6-90°

Figure B.1: Force vs. diameter reduction from 10 mm plate tensile tests

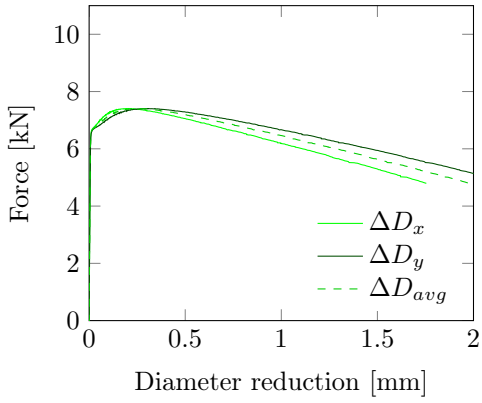

(a) Specimen 30-1-0°

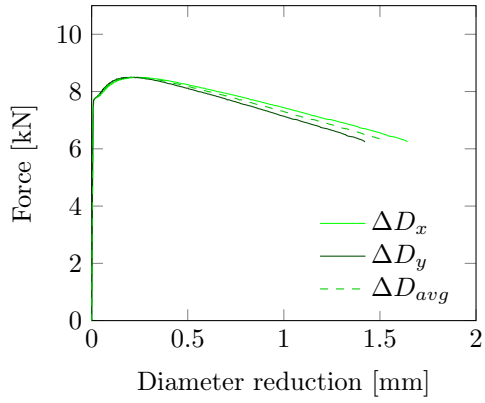

(b) Specimen 30-2-0°

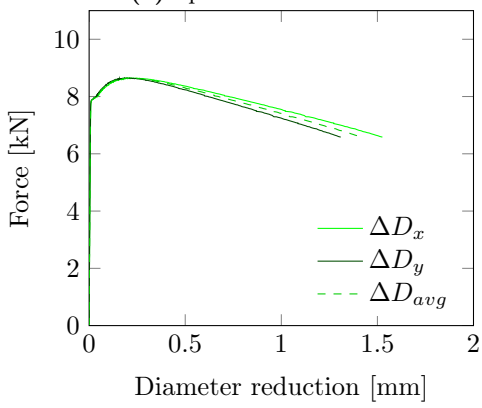

(c) Specimen 30-3-0°

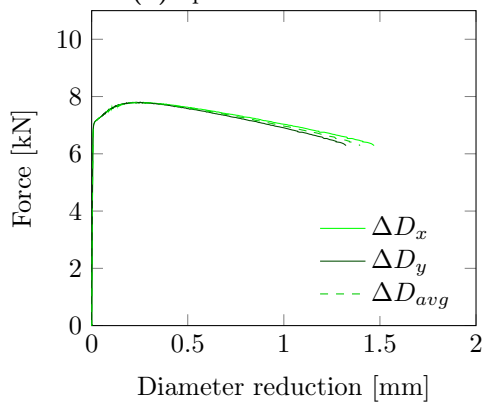

(d) Specimen 30-4-90°

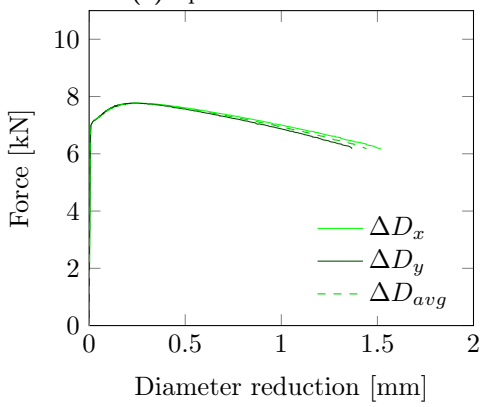

(e) Specimen 30-5-90°

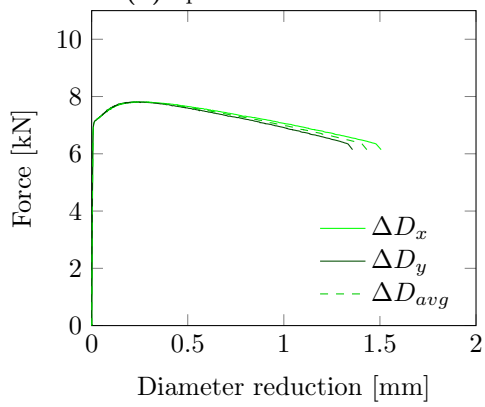

(f) Specimen 30-6-90°

Figure B.2: Force vs. diameter reduction from 30 mm plate tensile tests

APPENDIX C

Hardness Measurements - Raw Data

Table C.1: Raw data results from hardness testing across weld

	10 mm plate			20 mm plate			30 mm plate		
DFCW[a]	Top	Middle	Bottom	Top	Middle	Bottom	Top	Middle	Bottom
[mm]	[HV]	[HV]	[HV]	[HV]	[HV]	[HV]	[HV]	[HV]	[HV]
-20	-	-	-	-	-	-	88.6	-	85.8
-18	-	104	-	102	-	-	87.1	-	69.5
-16	103	101	103	96.5	103	100	81.3	90.9	57.2
-14	96.2	98.2	96.8	78.1	99.9	97.5	60.7	89.7	61.3
-12	85.8	86.9	89.7	70.9	94.3	89.1	56.9	90.6	77.0
-10	73.6	80.1	79.6	75.6	87.7	73.4	69.5	87.7	75.1
-8	68.3	67.5	64.0	75.8	77.9	77.9	77.7	80.1	78.9
-7	77.4	-	73.0	-	74.3	78.4	-	70.6	-
-6	76.3	67.1	77.4	76.7	71.1	79.1	74.1	62.8	73.4
-5	-	68.9	-	-	63.3	-	-	59.1	-
-4	77.0	71.3	76.5	76.7	61.3	79.6	73.4	60.0	74.3
-3	-	73.0	-	-	66.0	-	-	62.1	-
-2	74.3	70.3	72.8	78.9	68.1	81.1	76.3	69.9	77.4
-1	-	70.5	-	-	81.8	-	-	84.2	-
0	76.3	69.3	75.8	78.4	84.2	80.1	77.7	85.8	73.0
1	-	-	-	-	-	-	-	84.4	-
2	75.8	70.1	75.6	80.3	66.4	81.2	76.7	65.7	74.1
3	-	73.0	-	-	66.4	-	-	62.1	-
4	77.0	70.5	75.6	79.3	62.3	76.7	77.9	-	78.9
5	77.7	68.9	77.0	-	68.5	-	-	61.3	-
6	77.0	67.3	73.8	79.1	73.4	74.0	75.4	69.6	76.1
7	76.1	61.3	62.5	-	76.5	-	-	77.9	-
8	63.0	65.7	68.9	76.7	80.8	81.6	73.8	83.9	76.1
10	77.0	79.1	83.6	71.3	89.4	79.1	69.5	90.9	73.4
12	87.4	88.3	91.0	70.9	97.2	70.5	59.4	91.8	62.7
14	96.5	97.2	98.2	90.9	95.5	95.5	58.9	92.4	58.5
16	104	103	104	99.8	102	98.8	78.6	91.5	73.0
18	-	-	-	105	104	101	87.4	-	89.1
20	-	-	-	-	-	-	87.4	-	92.7

[a]Distance from center weld

Table C.2: Raw data results from hardness testing in thickness direction of base material

DFBP[a]	10 mm plate	20 mm plate	30 mm plate
[mm]	[HV]	[HV]	[HV]
0.5	110	106	89.1
2	109	107	86.6
4	110	107	89.7
6	110	106	88.6
8	110	106	88.9
10	-	103	90.0
12	-	105	91.2
14	-	105	89.4
16	-	105	90.9
18	-	104	89.4
20	-	-	90.9
22	-	-	89.1
24	-	-	89.4
26	-	-	88.3
28	-	-	88.6
Average	110	105	89.3

[a]Distance from bottom of plate

APPENDIX D

Impetus Input File

```
*UNIT_SYSTEM
SI
*PARAMETER
%E   = 70e9          # Youngs modulus
%A   = 317e6         # Voce parameters
%C1  = 17
%C2  = 1.6
%Q1  = 55e6
%Q2  = 165e6
%R0  = 0.45e-3       # hole radius
%R1  = 10.45e-3      # radius fine mesh
%R2  = 50.45e-3      # plate radius
%h   = 10.0e-3       # plate thickness
%v0  = 325.0         # impact velocity
%N   = 5             # mesh density parameter
*COMPONENT_PIPE # Makes the fine mesh of the 30 degree model
"Fine mesh"
1, 1, [2*%N], 2, [%N], 0, 30.0
0.0, 0.0, 0.0,  0.0, 0.0, [%h], [%R0], [%R1]
*COMPONENT_PIPE # Makes the coarse mesh of the 30 degree model
"Coarse mesh"
2, 2, [2*%N], 2, [%N], 0,  30.0
0.0, 0.0, 0.0,  0.0, 0.0, [%h], [%R1], [%R2]
*INCLUDE             # Includes and places the projectile from ...
    external file provided by Dr. Lars Olovsson
bullet_30_degree_2.k
1, 1, 1, 10000, 10000,
0, 0, 0, 0, 0, -15e-3
-1, 0, 0, 0, -1, 0
*CHANGE_P-ORDER # Makes all the elements in the model cubic 64 node ...
    hexahedron
ALL, 0, 3
*TIME                # Defines the simulation length
2.2e-4
*OUTPUT          # Defines how often output is written. Default ...
    totaltime/100 for frames and totaltime/1000 for plots
,,
*MAT_METAL       # Plate material
1, 2700.0, [%E], 0.33,1, 1
1, 0, 0, 0.001, 5e-4, 1.0, 293.0, 923
# Voce function
*FUNCTION            # Voce hardening function
```

```
40      1
41      %A+%Q1*(1 - exp(-%C1*epsp))+%Q2*(1 - exp(-%C2*epsp))
42      *PROP_DAMAGE_CL # Damage properties. Wc number and element erosion ...
            controls
43      1,0,
44      263.6e6
45      *PROP_THERMAL       # Thermal properties. Heat conductivity and heat ...
            expansion set to default (0)
46      1,, 894,, 0.9, 293.0
47      # core
48      *MAT_RIGID      # APM2 steel core modeled as rigid. Only density needed
49      4, 7850.0
50      *PART               # Define parts
51      "plate fine"
52      1, 1, 0, 0, 0, 7.0e-10
53      *PART
54      "plate coarse"
55      2, 1, 0, 0, 0, 7.0e-10
56      *PART
57      "core"
58      4, 4, 0, 0, 0, 7.0e-10
59      *SMOOTH_MESH        # Smoothens mesh if angle between element normals ...
            are higher than a given value.
60      ALL, 0, 40.0, 1
61      *INITIAL_VELOCITY   # Sets the initial velocity of the projectile
62      P, 4, 0.0, 0.0, [-%v0]
63      *CONTACT            # Contact definition. Here Impetus decides which ...
            part is master/slave. Friction = 0
64      ALL,0,ALL,0,0, -1.0e15
65      1
66      0, 0, 1
67      *BC_SYMMETRY        # Symmetry planes and tolerance
68      0, 1, 2,,1e-5
69      *MERGE_DUPLICATED_NODES # Merging duplicated nodes between fine and ...
            coarse mesh in plate
70      P, 2, P, 1, 1.0e-8
71      *COORDINATE_SYSTEM_FIXED    # Symmetry plane 1 normal
72      1,0.00764267,0.0044125,0.005
73      *COORDINATE_SYSTEM_FIXED    # Symmetry plane 2 normal
74      2,0.008825,0,0.005
75      *END
```

APPENDIX E

Recht-Ipson Curve Fit - Matlab Script

```
clc;
clear all;
close all;

%Name of input file
file = 'impetus-20-b-0fr.txt';

%Import datafile
import = importdata(file);

%Set Recht-Ipson parameters
a = 1;
p = 2;

%define input- and output velocity
vi = import(:,1);
vr = import(:,2);

    %Curvefit function

    [xData, yData] = prepareCurveData( vi, vr );

    % Set up fittype and options.
    ft = fittype( 'a*(((x^(p))-(vbl^(p)))^(1/p))', 'independent', 'x', ...
        'dependent', 'y' );
    opts = fitoptions( 'Method', 'NonlinearLeastSquares');
    opts.Display = 'Off';
    % Insert values in the area of where vbl will be
    opts.Lower = [250];
    opts.StartPoint = [270];
    opts.Upper = [400];

    % Fit model to data.
    [fitresult, gof] = fit( xData, yData, ft, opts );

    coeffs = coeffvalues(fitresult);

    vbl = coeffs(1);
    % Make curve from fitted vbl
    x = vbl:1:900;
    y = a*(((x.^p) - (vbl.^p)).^(1/p));

```

```
42 topgfplots = [x',y'];
43
44 % Set name of pgf file
45 newfile = strcat('pgf_',file);
46
47 % Write to file
48 printfile = fopen(newfile,'w');
49 fprintf(printfile,'vi\tvr\n');
50 fprintf(printfile,'%.3f\t%.3f\n',topgfplots');
```

APPENDIX F

Field Model - Matlab Script

```
clc
clear all
close all
%% Read node map and element connectivity data
A = importdata('nodes.txt',',',0);
B = importdata('elements.txt',',',0);

%% Create output file
geometri = fopen('geometri.k','w');

%% Change units from mm to m
A(:,2)=(A(:,2)./1000);
A(:,3)=(A(:,3)./1000);
A(:,4)=(A(:,4)./1000);

%% Print file headers,node map, and element connectivity
    fprintf(geometri,'*NODE\n');
    fprintf(geometri,'%i,%1.7e,%1.7e,%1.7e\n',A');
    fprintf(geometri,'*ELEMENT_SOLID\n');

    for i = 1:length(B)
        %% Find midpoint in element
        x = A(B(i,2),2);
        z = A(B(i,2),4);
        if x > 0
            x = x - 0.0005;
        else
            x = x + 0.0005;
        end

        %% Place element in correct part according to
        %  polynomials governing hardness positions

        if abs(x) < ((0.009/(0.015^2))*((z-0.015)^2) + 0.0025)
            part = 1;
        elseif abs(x) < ((0.009/(0.015^2))*((z-0.015)^2) + 0.0055)
            part = 2;
        elseif abs(x) < ((0.008/(0.015^2))*((z-0.015)^2) + 0.010)
            part = 3;
        else
            part = 4;
        end
```

```
43      inputline =     ...
            strcat(num2str(B(i,1)),',',num2str(part),',',num2str(B(i,2)),' ...
            ,',num2str(B(i,3)),',',num2str(B(i,4)),',',num2str(B(i,5)),', ...
            ',num2str(B(i,6)),',',num2str(B(i,7)),', ',num2str(B(i,8)),', ...
            ',num2str(B(i,9)),'\n');
44      fprintf(geometri,inputline);
45  end
46  fprintf(geometri,'*END');
```